

HIGH PRESSURE VIBRATIONAL SPECTROSCOPY

A thesis presented for the degree of

DOCTOR OF PHILOSOPHY

in the

Faculty of Science

by

MARK POGSON

University of Leicester

1987

UMI Number: U012821

All rights reserved

INFORMATION TO ALL USERS

The quality of this reproduction is dependent upon the quality of the copy submitted.

In the unlikely event that the author did not send a complete manuscript and there are missing pages, these will be noted. Also, if material had to be removed, a note will indicate the deletion.



UMI U012821

Published by ProQuest LLC 2015. Copyright in the Dissertation held by the Author.  
Microform Edition © ProQuest LLC.

All rights reserved. This work is protected against  
unauthorized copying under Title 17, United States Code.



ProQuest LLC  
789 East Eisenhower Parkway  
P.O. Box 1346  
Ann Arbor, MI 48106-1346

x751539030

### STATEMENT

The work recorded in this thesis is entirely original unless otherwise acknowledged in the text or by reference and was carried out by the author in the Department of Chemistry of the University of Leicester between October 1983 and September 1986. The work has not been, nor will be, presented for any other degree.

A handwritten signature in black ink, appearing to read 'M. Pogson', with a stylized, cursive script.

M. POGSON

## ABSTRACT

### HIGH PRESSURE VIBRATIONAL SPECTROSCOPY

M. POGSON

The study of solids at high pressure and variable temperature enables development of accurate interatomic potential functions over wide ranges of interatomic distances. A review of the main models used in the determination of these potentials is given in Chapter one. A discussion of phonon frequency as a variable physical parameter reflecting the interatomic potential is given.

A high pressure Raman study of inorganic salts of the types  $MSCN$ , ( $M = K, Rb, Cs \text{ \& } NH_4^+$ ) and  $MNO_2$ , ( $M = K, Na$ ) has been completed. The studies have revealed two new phases in  $KNO_2$  and one new phase in  $NaNO_2$  at high pressure. The accurate phonon<sup>2</sup> shift data have enabled the determination of the pure and biphasic stability regions of the phases of  $KNO_2$ . A discussion of the B1, B2 relationship of univalent nitrites is also given.

In the series of thiocyanates studied new phases have been found in all four materials. In both the potassium and rubidium salts two new phases have been detected, and in the cesium salt one new phase has been detected, all at high pressure, from accurate phonon shift data. These transitions are discussed in terms of second-order mechanisms with space groups suggested for all phases, based on Landau's theory of second-order phase transitions. In the ammonium salt one new phase has been detected. This new phase transition has been interpreted as a second-order transition.

The series of molecular crystals  $CH_3HgX$ , ( $X = Cl, Br \text{ \& } I$ ) has been studied at high pressure and at variable temperature. In Chapter five, their phase behaviour at high pressure is detailed along with the pressure dependencies of their phonon frequencies. In the chloride and the bromide two new phases have been detected. In the bromide one has been detected at high temperature and one at high pressure, the latter being interpreted as the stopping of the methyl rotation. In the chloride one phase has been found at both low temperature as well as high pressure, and the other only at high pressure, the latter again associated with the stopping of methyl rotation. The iodide displays two high pressure transitions. A Raman-active soft-mode has been observed in all three analogues, at both high pressure and variable temperature. For the chloride and bromide analogues there is a discussion of the nature of the soft-mode along with the mechanism associated with the I/II transition. The results of the X-ray crystal structure determination of  $CH_3HgBr$  at ambient temperature and pressure are given.

### ACKNOWLEDGEMENTS

I would primarily like to thank my supervisor, Dr. David Adams, whose continued help and encouragement has proved so vital in the production of this thesis.

Thanks must also go to Mrs. Ann Crane for the drawing and tracing of the majority of figures in this thesis. Also, I must express my appreciation to Phil Acton, for his tireless efforts in keeping the equipment going when all seemed lost.

I must thank the other members of the group for their help and humour. In particular Gillian Stanger and Patrick Fletcher for reading and correcting the contents of my thesis.

Finally, thank-you to all my friends and the members of my family who have encouraged me over the years.

## CONTENTS

	<u>Page</u>
CHAPTER 1    POTENTIAL FUNCTIONS IN THE SIMULATION OF SOLIDS	1
CHAPTER 2    EXPERIMENTAL TECHNIQUES	19
CHAPTER 3    A RAMAN SCATTERING STUDY OF MSCN COMPOUNDS (M = K,Rb,Cs & $\text{NH}_4^+$ ) AT HIGH PRESSURE	28
CHAPTER 4    A RAMAN SCATTERING STUDY OF UNIVALENT NITRITES $\text{MNO}_2$ (M = Na & K) AT HIGH PRESSURES	40
CHAPTER 5    A RAMAN STUDY OF THE PHASE BEHAVIOUR OF METHYL MERCURY HALIDES $\text{CH}_3\text{HgX}$ (X = Cl,Br & I) AT HIGH PRESSURE AND RELATED SOFT MODES	56

## INTRODUCTION

The use of pressure in studying the solid state has two main areas of application:

1) To investigate the phase behaviour of solids, with a view to discovering and rationalising new phases.

2) In the study of the variation of physical parameters with pressure to obtain information on the nature of interatomic potentials.

In this thesis applications are reported in both of these areas.

In chapter 1, the theoretical setting for the new pressure-phonon data is outlined. The new data obtained during this work have been displayed in the experimental chapters. These data have extended our knowledge of both areas indicated above.



## CHAPTER ONE

### POTENTIAL FUNCTIONS IN THE SIMULATIONS OF SOLIDS

## CHAPTER ONE

### POTENTIAL FUNCTIONS IN THE SIMULATIONS OF SOLIDS

#### 1.1.Introduction

In recent years computer simulation of solids has enjoyed a considerable degree of success due primarily to the development of potential models based upon two-body interactions or pair potentials. All these models account for many of the properties of crystals and have a relatively simple functional form which may be incorporated into computer codes.<sup>1</sup>

In the case of vibrational spectroscopy the observable property of the crystal will be phonon frequency ( $\omega$ ), which is directly associated with bond strength and atomic displacement. After discussion of the relation of phonon frequency to potential functions, outlining the need for high pressure spectroscopy in this area, a discussion of currently used models with some examples will be given.

#### 1.2.Potential functions

The potential energy curve, Fig 1.1, shows how the energy of interaction between two atoms, changes with distance. At  $R_e$ , the equilibrium distance, there is an energy minimum.

From a simple harmonic approximation the relationship is

$$V(R)=1/2k(R-R_e)^2 \quad (1)$$

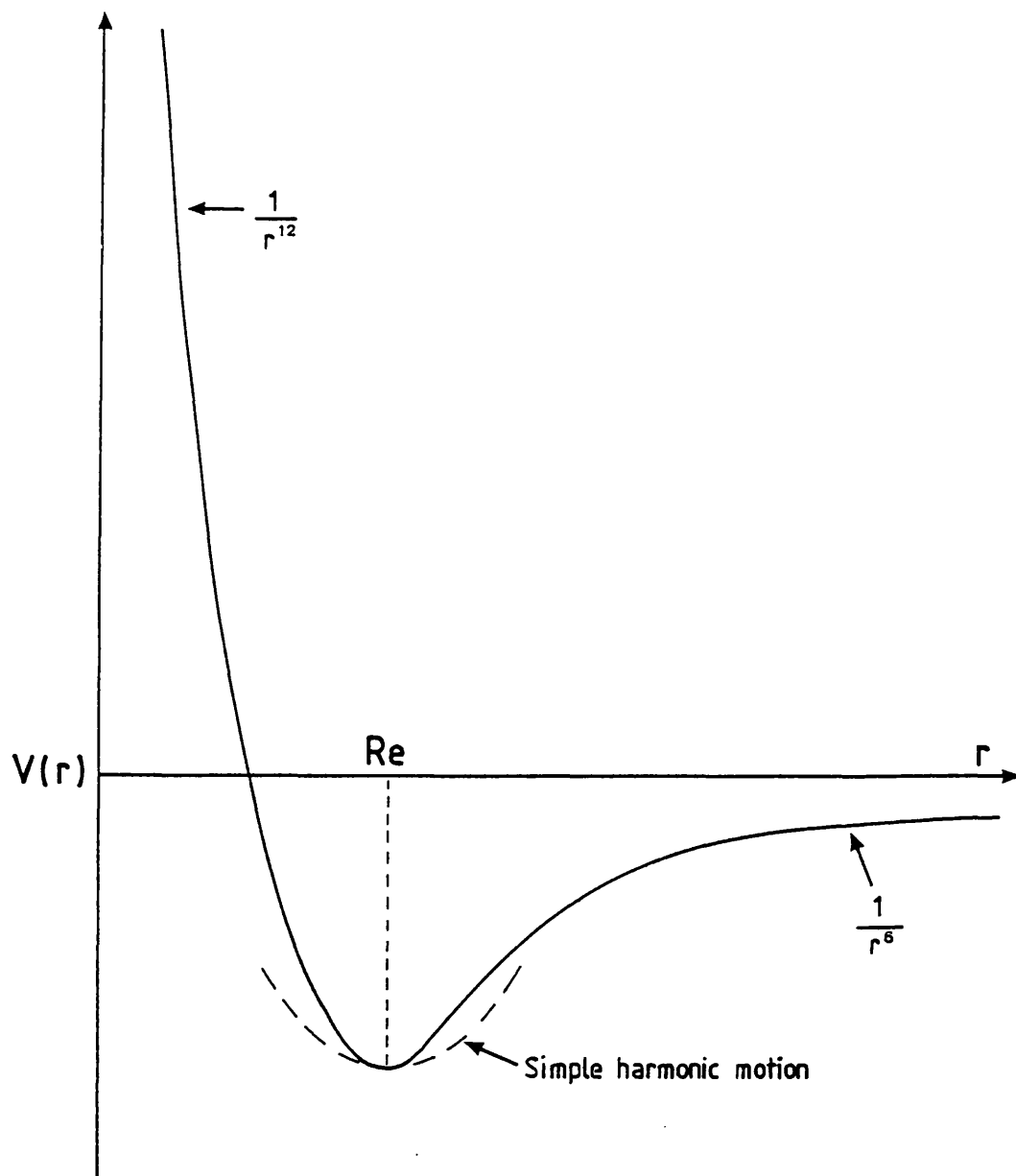
Near  $R_e$ , the potential energy curve approximates to the above relationship, where  $k$  is the force constant for the bond.

Figure 1.1

This diagram shows the interaction energy  $V(r)$  between two atoms changing with interatomic distance  $r$ . The interaction is determined by a function of the form

$$V(r) = A\exp(-r/\rho) - Cr^{-6}$$

$R_e$  is the equilibrium distance corresponding to an energy minimum. The dotted curve indicates a simple harmonic approximation.



### 1.3. Force constants

The energy of a pair-wise interaction, can be described in terms of displacement coordinates and a force constant. This in turn allows the calculation of the vibrational frequency ( $\omega$ ) of the interaction, given a set of positional coordinates. Considering a relationship for a potential function, with energy  $V$ ,

$$V = V_0 + \sum_{i=1}^{3N} (\partial V / \partial q_i)_0 \cdot q_i + 1/2 \sum_{i,j=1}^{3N} (\partial^2 V / \partial q_i \partial q_j)_0 \cdot q_i \cdot q_j + \dots \quad (2)$$

$V_0$  is a constant which is independent of  $q$  and may be ignored. At the equilibrium position  $q_i=0$ ,

$$\sum_{i,j=1}^{3N} (\partial V / \partial q_i)_0 \cdot q_i = 0$$

Higher order terms can also be neglected when considering small amplitude modes, resulting in

$$V = 1/2 \sum_{i,j=1}^{3N} (\partial^2 V / \partial q_i \partial q_j)_0 q_i \cdot q_j \quad (3)$$

where  $(\partial^2 V / \partial q_i \partial q_j)_0$  corresponds to the force constant of the interaction. We have finally,

$$V = 1/2 \sum_{i,j=1}^{3N} f_{ij} \cdot q_i \cdot q_j \quad (4)$$

where  $q_i$  and  $q_j$  are displacement coordinates and  $f_{ij}$  is the force constant of the interaction.

#### 1.4.Vibrational modes

Vibrational frequencies, of a crystal are obtained for a given wave vector  $\underline{k}$  from the secular equation

$$|F(k) - 4\pi^2 \cdot \omega^2 \cdot M| = 0 \quad (5)$$

where

$$F(k)(st, s't') = \sum \partial^2 V / \partial r(s, t) \cdot \partial r(s' t') \cdot \exp(ik \cdot R) \quad (6)$$

$r(s, t)$  is the position vector of an atom  $t$  in the molecule  $s$  within the central unit cell  $l$ , defined in cartesian coordinate space.  $M$  is the mass related term and  $\omega$  is the frequency of the vibration, with  $R$  a displacement vector. We now have a direct link between a potential function and the vibrational frequency of a Raman or infrared active mode from a force constant.

#### 1.5.Problems in defining accurate potential functions

It is relatively easy to set up some form of interatomic potential for a given type of material, and not too difficult to obtain values of it at a limited number of interatomic separations. However, the real problem arises in defining the shape of the function accurately at all distances ( $R$ ) and particularly when  $R < R_e$ . It is important to be able to do so because phase changes induced by temperature and pressure cannot be calculated unless the dependence of a potential on temperature and pressure is known. There is also a need for the calculation of elastic constants and other physical parameters away from the equilibrium setting and within stable phases.

In all this there is no substitute for the direct measurement of parameters that vary with temperature and pressure and have a dependence upon the potential function. Such a direct method is the measurement of X-ray determined lattice parameters as a function of temperature and pressure. Other techniques include measurement of phonon shifts, which is the topic of this thesis.

### 1.6. How is this sampling done ?

The following discussion will focus on the study of potential functions and phonon frequencies, with varying temperature and pressure.

a) An increase in lattice parameters can be achieved by the use of high temperatures. If  $R_c$  exists at ambient temperature and pressure, then an increase in temperature will increase the distance of a pair interaction within a stable phase. This new position in P/T space will result in a new value for the equilibrium separation  $R'_c$ . However, this has also defined a point on the original potential function, enabling refinement in this region. These data obtained with a variable temperature study, Fig. 1.2, can be used to define the attractive part of a potential more accurately.

b) A decrease in lattice parameters can be achieved by either decreasing temperature or increasing pressure. If we are decreasing the lattice parameters, it follows that in general, the distance between the pair interaction will decrease if we stay within a stable phase. This in turn forces an increase in the pair interaction energy, mirrored by an increase in phonon frequency, Fig. 1.3.

A discussion of various useful potential models follows. All references will be made to two-body, pair potentials, and not many-body potentials, unless stated.

### 1.7. Pair potentials in ionic solids

Lattice modelling techniques in the field of ionic and semi-ionic materials have been particularly successful. This is due to the development of potential models which account for most of the observed properties displayed by the crystal, and still have a sufficiently simple form to enable incorporation into computer codes without the use of extensive computer time.

Ionic solids are most often described by models which assign charges to point entities between which short-range interactions are specified. These descriptions also include polarisability functions when necessary.

The only successful models up to date are those of a central force type, which consider  $V(r_1 \dots r_N)$  the total potential energy, expressed as the sum of pair interactions of  $N$  particles with coordinates  $r_1 \dots r_N$ ,

Figure 1.2

Variation of phonon frequency with temperature.

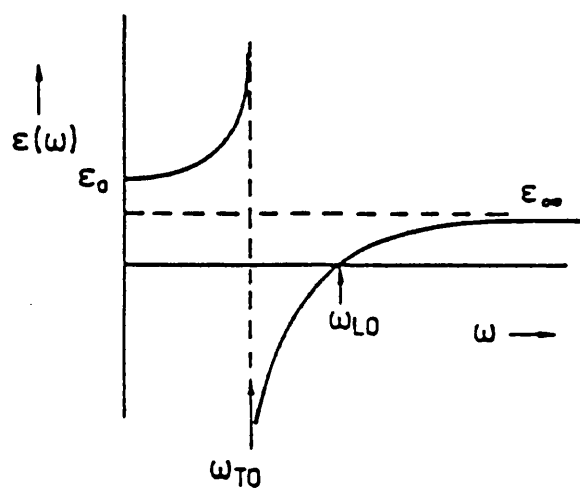
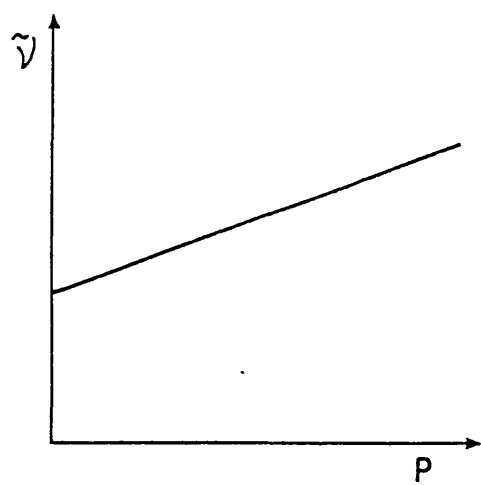
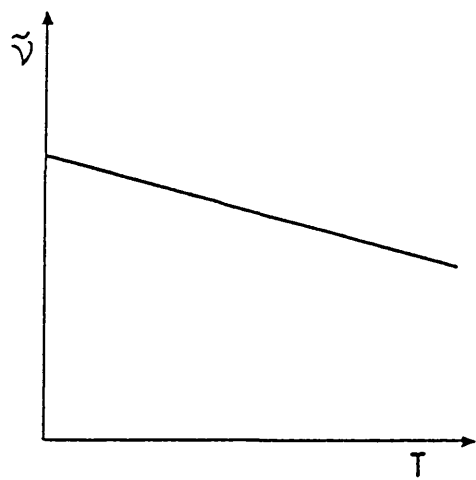
Figure 1.3

Variation of phonon frequency with pressure.

Figure 1.4

Schematic plot of the frequency dependence of  $\epsilon(\omega)$ .





in the form

$$\text{total P.E.} = V(r_1 \dots r_N) = \sum V_{ij}(|r_i - r_j|) \quad (7)$$

These pair-wise interactions are dependent on the distance between the particles and can be described by the use of a well known Born-Mayer function of the form

$$V(r) = A \exp(-r/\rho) - Cr^{-6} \quad (8)$$

In general two basic procedures are used in the estimation of these short-range potentials; empirical parameterisation and non-empirical methods.

#### 1.7.1. Empirical parameterisation

Given specific sets of pair potentials for various interactions in a crystal it is possible to calculate its elastic, dielectric and piezoelectric constants as well as the phonon dispersion curves. These elastic and dielectric constants along with lattice vibrational frequencies do not depend on the interionic potentials directly but rather on the first and second derivatives of these potentials with respect to the interionic separation. Potentials of this form which have been refined by standard fitting procedures give an impressive measure of agreement with experimental data, Table 1.1.<sup>3,4</sup>

Further information on potentials can be obtained from structural data where, in addition to the properties discussed above, the minimisation of bulk internal strains acting on the unit cell may be calculated. Such strains arise when the potentials calculated do not fit fully with observed structures. The fitting of structures via short-range parameter variation enables the strain to be minimised. This type of approach has become a powerful tool in the study of complex, low symmetry systems.<sup>2</sup>

In general though the lack of information on potentials over a wide range of internuclear distances remains a basic inadequacy of the empirical parameterisation method. Due to this inadequacy, a non-empirical approach has been developed.

Table 1.1: Calculated and observed crystal properties for  $\text{CaF}_2$  (after Catlow and Norgett<sup>3</sup> who give references to experimental data).

	Expt.	Calculated value
$r_0$	2.722	(2.722)
$C_{11}$	17.124	(16.9)
$C_{12}$	4.675	(4.80)
$C_{44}$	3.624	3.23
$\epsilon_0$	6.47	(6.42)
$\epsilon^\infty$	2.05	(2.01)
$\omega_{\text{TO}}$	270.0	(259.2)
$\omega_{\text{R}}$	330.5	310.7
$\alpha_+$	0.979	(0.984)
$\alpha_-$	0.759	(0.765)
$C_{111}$	-124.6	-107.8
$C_{112}$	-40.0	-33.8
$C_{123}$	-25.4	-17.5
$C_{144}$	-12.4	-9.3
$C_{166}$	-21.4	-23.2
$C_{456}$	-7.5	-7.8
$H_{\text{L}}$	-26.76	-28.06

Key:  $r_0$  - lattice constant (Ångstroms)

$C_{11}, C_{12}, C_{44}$  - second order elastic constants ( $10^{11}$  dyne  $\text{cm}^{-1}$ )

$\epsilon_0, \epsilon^\infty$  - dielectric constants at zero and high frequencies

$\omega_{\text{TO}}, \omega_{\text{R}}$  - transverse optic and Raman frequencies ( $\text{cm}^{-1}$ )

$\alpha_+, \alpha_-$  - cation and anion polarisabilities ( $\text{\AA}^3$ )

$C_{111}, C_{112}, C_{123}, C_{144}, C_{166}, C_{456}$  - third order elastic constants ( $10^{11}$  dyne  $\text{cm}^{-1}$ )

$H_{\text{L}}$  - lattice formation energy (eV).

(Bracketed values used in fitting)

### 1.7.2. Non-empirical methods

Pair potentials as such in solids, are not readily obtained directly from full *ab initio* quantum mechanical calculations. However, they can be extracted from approximate formulations. The most important of these for ionic interactions, certainly in the solid state, is that based on the density function treatment of the uniform electron gas.<sup>5,6,7</sup>

The energy of a closed shell ion or atom is written as<sup>1</sup>

$$\begin{aligned}
 E[\rho] = & C_k \int [\rho(r)]^{5/3} dr + C_e \int [\rho(r)]^{4/3} dr \\
 & - Z \int \rho(r)/r dr + 1/2 \iint \rho(r)\rho(r')/|r-r'| dr.dr' \\
 & + \int \epsilon_c [\rho(r)]\rho(r)dr
 \end{aligned} \tag{9}$$

where  $Z$  is the nuclear charge,  $C_k$  and  $C_e$  are constants and the first four terms represent the kinetic, exchange and coulomb energies respectively, while the last term is an approximation to the electron pair correlation energy. This final term according to Gordon and Kim<sup>7</sup> may be determined by interpolating between the high and low density limits for a homogeneous electron gas. For a pair of ions, AB, the total electron density  $\rho_{AB}(r)$  is assumed to be the sum of the separate ion densities  $\rho_A(r)$  and  $\rho_B(r)$ .

The total energy of AB, is therefore

$$E_{AB} = E[\rho_{AB}] = E[\rho_A + \rho_B] \tag{10}$$

The interaction energy,  $V_{AB}$  can be written as

$$V_{AB} = E[\rho_A + \rho_B] - E[\rho_A] - E[\rho_B] \tag{11}$$

$V_{AB}$ , particularly at or near the minimum energy separation is a small difference ( $\sim 1$  eV) between two very much larger quantities ( $\sim 6000$ – $9000$  eV). Thus, to minimise numerical errors in the calculation of  $V_{AB}$  Gordon and Kim rearranged the integral expressions in equ.9 to give the final form for  $V_{AB}$  as

$$\begin{aligned}
 V_{AB}(R) = & Z_A Z_B / R - Z_B \int \rho_A(r_1) / r_{1B} dr_1 \\
 & - Z_A \int \rho_B(r_2) / r_{2A} dr_2 + \iint \rho_A(r_1) \rho_B(r_2) / r_{12} dr_1 dr_2 \\
 & + \int \{ [\rho_A(r) + \rho_B(r)] E_G[\rho_A(r) + \rho_B(r)] \\
 & - \rho_A(r) E_G[\rho_A(r)] - \rho_B(r) E_G[\rho_B(r)] \} dr \quad (12)
 \end{aligned}$$

where  $E_G[\rho(r)]$  is related to a number of energy dependent terms previously mentioned in equ.9, and  $r$ ,  $r_{1B}$ ,  $r_{2A}$  and  $r_{12}$  are functions of the internuclear separation,  $R$ . Refinements to this approach have been reported,<sup>8-10</sup> but discussion of these is not warranted in this work.

### 1.7.3. Molecular Crystals

The term **molecular crystal** is applied to a group of compounds whose structures are variations of close-packing. In the case of non-polar molecules, in which non-directional bonding predominates, the structure is determined by the way which the molecules may pack. For crystals composed of molecules having some polar character the additional interactions possible (dipole-dipole, dipole-induced dipole, etc.) may have important modifying effects upon the structure adopted by these molecular crystals.

It is the form that these interactions take (ie. combination of non-directional and directional bonding) which shapes any pair wise interaction.

In addition, Kitaigorodskii laid down the basic principles of

molecular crystal packing and followed through their implications. He deduced that it was possible to predict a short list of space groups for crystals composed of molecules with a given symmetry.<sup>11</sup>

#### 1.7.4. Van der Waals and related interactions

The equilibrium positions of molecules in crystals are again a balance between attractive and repulsive forces. A simple expression for a pair-wise interaction may take the form,

$$U(r) = A/r^n - B/r^m \quad (13)$$

For non-polar molecules, as in the case of some organic molecular crystals, the attractive potential is dominated by dispersive forces. However, the repulsive part of the potential is dominant in determining the nature of the packing; this is reflected by its higher-order dependence on  $r$  since  $n > 6$ . The attractive forces, which are effectively non-directional, are not minimised at the eventual stable configuration.

Dispersive interactions, arise from the correlated motions of electrons on different atomic or molecular centres. This correlation which is due to the coulombic interaction of the electrons, results in an instantaneous dipole on each of the interacting species. The interaction of these dipoles and higher order multipoles give rise to what is referred to as the van der Waals energy  $\Phi_v$ . It can be written as an asymptotic expansion of the form

$$\Phi_v(r) = r^{-6} \sum_{n=0} C_n r^{-2n} \quad (14)$$

where  $C_n$  is the so called van der Waals coefficient. From the above description of its origins, it is clear that a van der Waals interaction is essentially a polarisation phenomenon, where its lowest order or London energy,  $\Phi_L(r)$  can be written as

$$\Phi_L(r) = (3h/\pi r^6) \int_0^\infty \alpha_A(i\omega) \alpha_B(i\omega) d\omega \quad (15)$$

where  $\alpha_A$  and  $\alpha_B$  are polarisabilities of the two species at a frequency  $i\omega$ .

Estimates of  $C_n$  are available following initial work by Mayer 1933;<sup>12</sup> however, in general, the values are not accurately known. Early work attempted the determination of  $C_n$  by optical absorption data but experienced two main problems. First, the energies of the optical excitations of the anions and cations often overlap and, second, it is uncertain as to how much adjustment should be made for local field effects in an ionic solid. However, hopeful development has appeared in the application of *ab initio* quantum mechanical methods, which include calculation of correlation effects by means of configuration interaction and other techniques. Recent work along these lines has been reported by Andzelm and Piela 1978 on NaF and LiF.<sup>13</sup>

Some recent studies have treated  $C_n$  as a variable parameter which can be determined by "fitting" to empirical data, or to a calculated interionic potential. It is unlikely that these calculated parameters reflect true dispersion phenomena, but in fact contain varying degrees of covalency. In short, it is not clear how dispersion energies can be calculated from potentials based on these methods with any great degree of accuracy, often the very magnitudes are in doubt. In the case of empirical potentials there is no convincing interpretation of the  $r^{-6}$  term itself.

On this note, it may be helpful to discuss various other models which have exhibited varying degrees of success within the limits they impose.

#### 1.7.5. Ionic polarisation (I.P.)

The following discussion on ionic polarisation will concentrate on phenomenological models, which are justified largely by their ability to interpret and predict experimental data.

For present purposes polarisability is related to induction of a dipole moment in a crystal by the application of an electric field, where the dipole moment per unit volume is the polarisation, the magnitude of which depends on the frequency of the applied field and can be expressed in terms of  $\chi(\omega)$  the frequency-dependent susceptibility. The

dielectric function  $\epsilon$ , in turn is frequency dependent and given by

$$\epsilon(\omega) = 1 + 4\pi \chi(\omega) \quad (16)$$

Fig.1.4 gives a schematic representation of the frequency dependence of  $\epsilon(\omega)$ , which can be expressed using the following relationship

$$\epsilon(\omega) = \epsilon^\infty + (\epsilon_0 - \epsilon^\infty) \frac{\omega_{TO}^2}{(\omega_{TO}^2 - \omega^2)} \quad (17)$$

In the following discussion we will be concerned primarily with  $\epsilon^\infty$  which arises solely from electronic displacements, since nuclei are unable to follow the high frequency field. At lower frequencies both nuclear and electronic displacements contribute to the dielectric function. From equ.(17) we can deduce

$$\omega_{LO}^2 / \omega_{TO}^2 = \epsilon_0 / \epsilon^\infty \quad (18)$$

which is the well known Lyddane-Sach-Teller (L.S.T.) relationship, and is obeyed by ionic crystals. A typical example is provided by NaI where the ratio  $\epsilon_0 / \epsilon^\infty$  at 0K is 2.21, while  $(\omega_{LO} / \omega_{TO})^2$  is 2.0. Further, we shall see that comparison between calculated and experimental dispersion curves provides one of the most critical tests of the reliability of phenomenological models, although it is often the case that polarisation parameters are obtained merely by fitting to  $\epsilon_0$  and  $\epsilon^\infty$ . The following sections will discuss the nature of the various models and there parameterisation.

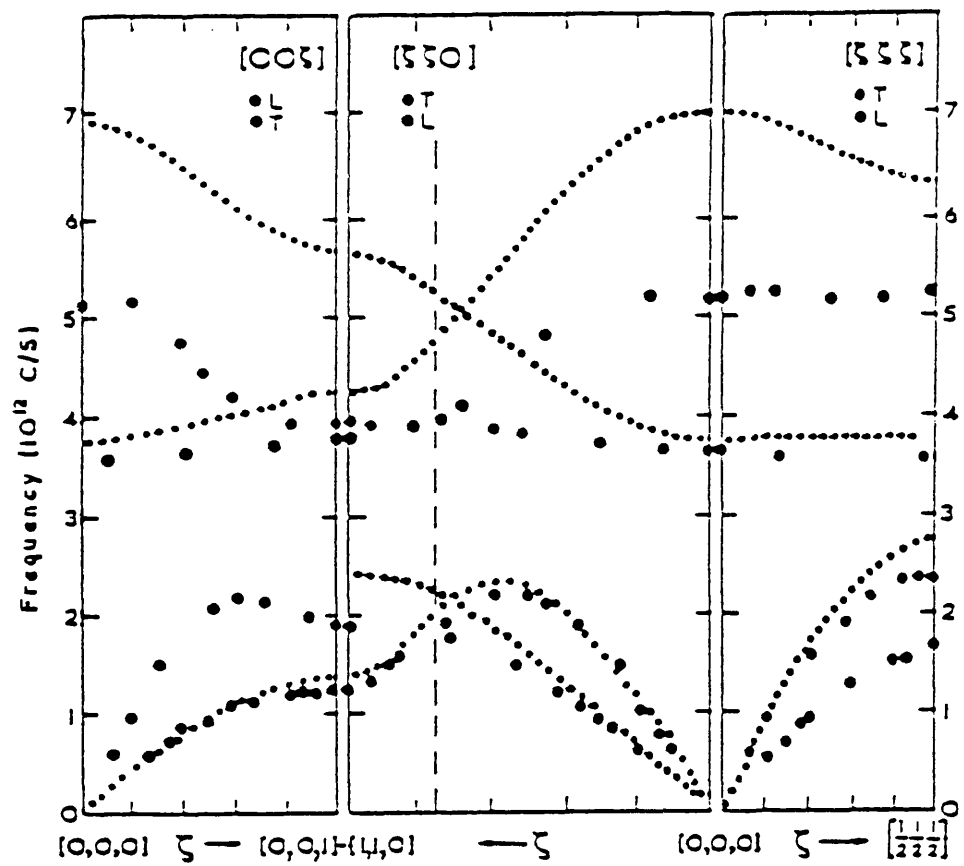
#### 1.7.6.Rigid ion model

This is the simplest class of ionic model and ignores any polarisation effects completely since it assumes  $\epsilon^\infty = 1$ . However, from the L.S.T. relationship, it is impossible for such models to provide adequate descriptions of dynamic properties of the lattice. From Fig.1.5



**Figure 1.5**

Experimental dispersion curves for NaI,  
compared with the predictions of the  
rigid ion model (....) at 100 K.



we can see that this model gives fair agreement for acoustic branches, but poor agreement for optic branches. It also fails badly in the calculation of defect energies, giving errors of up to 50%, since for ionic crystals, it is necessary to calculate an accurate static dielectric constant. In view of the importance of the dielectric response of the lattice to charge defects, a correct description of the static dielectric properties is perhaps the most important single requirement of a model in defect studies. Unfortunately, models which effectively do this do so at the expense of other crystal properties.

It is clear though, that some representation of polarisability is necessary and discussion of the simplest model which includes this effect is given below.

#### 1.7.7. Point polarisable ion (PPI) models

In the PPI model, the ion polarisability is introduced via a dipole  $\mu$ , which is induced by an electric field  $E$ .

$$\mu = \alpha E \quad (19)$$

where  $\alpha$  is the polarisability. Calculations on defects based on this model indicate a fundamental instability, which manifests itself as a "polarisation catastrophe" in which the dipole moment of the ion pairs increase without bound due to their polarisation fields. Even when calculations of this type were found to converge they were found to result in energies considerably lower than experimental values.<sup>14,15</sup>

The reason for this discrepancy can be traced to a further flaw in the PPI model, namely that excessively large static dielectric constants are obtained by these models when used in conjunction with short-range parameters obtained by fitting to elastic constants or acoustic phonon data. The fundamental inadequacy of the PPI model is that it fails to allow for any interdependence of short-range forces and ion polarisation.

In a polarisation field, there is a displacement of electrons which alters short-range interactions between ions due to overlapping charge clouds. It is essential that this be taken into account, and the simplest model which includes this is the shell model.

### 1.7.8.Shell model

The shell model is a simple mechanical model, which couples together ion polarisation and effective overlap forces, Fig.1.6. Each ion consists of two parts, the core  $X$  and the shell  $Y$ . The total ionic charge is the sum of  $X$  and  $Y$ . The mass of the ion is centered at the core, with the short-range of overlap forces acting through the "mass less" shell.  $X$  and  $Y$  are coupled by a harmonic "spring" with a force constant  $k$ , and polarisability  $\alpha$ , given by

$$\alpha = Y^2/k \quad (20)$$

The parameters  $Y$  and  $k$  are generally obtained by fitting, usually to dielectric data, although elastic and phonon properties are sometimes used.

Fig.1.7 shows that agreement is good over a wide range of wave vectors. The instabilities and inadequacies of the PPI model have been removed, also defect studies no longer show the polarisation catastrophe phenomenon.

The shell model has been further extended to take into account the effects of shell distortion due to neighbouring ions. This manifests itself as the breathing shell model, and allows a spherically symmetrical distortion of the shells. With this new model good agreement over the whole Brillouin zone is obtained. Sangster 1974,<sup>16</sup> has further extended the breathing model to use ellipsoidal deformations.

It is clear that the shell model is capable in its various forms of reproducing accurately a wide variety of lattice properties Tables 1.1 and 1.2.

Even though improvements to the model such as reliable non-empirical methods for deriving shell charges and spring constants would be desirable, it is the only available approach which can reproduce accurately the structural, dynamic and defect properties of ionic and semi-ionic crystals.

Table 1.2: Calculated and observed crystal properties for  $\text{Al}_2\text{O}_3$  and  $\text{TiO}_2$  (after Catlow *et al.* who give reference to experimental data).<sup>4</sup>

Lattice	$\alpha\text{-Al}_2\text{O}_3$		$\text{TiO}_2$	
Properties/Systems	Calculated	Observed	Calculated*	Observed
Lattice energy (eV)	-160.21	-160.4	-109.90	126.0
** $C_{11}$	42.96	49.69	25.33	27.01
$C_{12}$	15.48	16.36	17.80	17.66
$C_{13}$	12.72	11.09	20.90	14.80
$C_{33}$	50.23	49.8	77.92	48.19
$C_{14}$	-2.99	-2.35	---	---
$C_{44}$	16.66	14.74	9.22	12.39
$C_{66}$	13.70	16.66	22.12	19.30
§ $\epsilon_{11}^p$	9.38	9.34	94.76	86.0
$\epsilon_{33}^p$	11.52	11.54	157.32	170.0
$\epsilon_{11}(\infty)$	2.08	3.1	6.28	6.83
$\epsilon_{33}(\infty)$	2.02	3.1	7.99	8.43

\* Calculated value for fitted potentials.

\*\* Elastic constants ( $10^{11}$  dyn cm<sup>2</sup>).

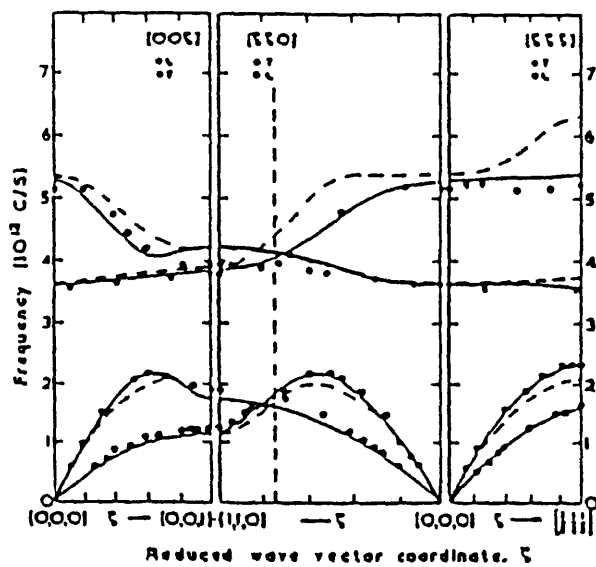
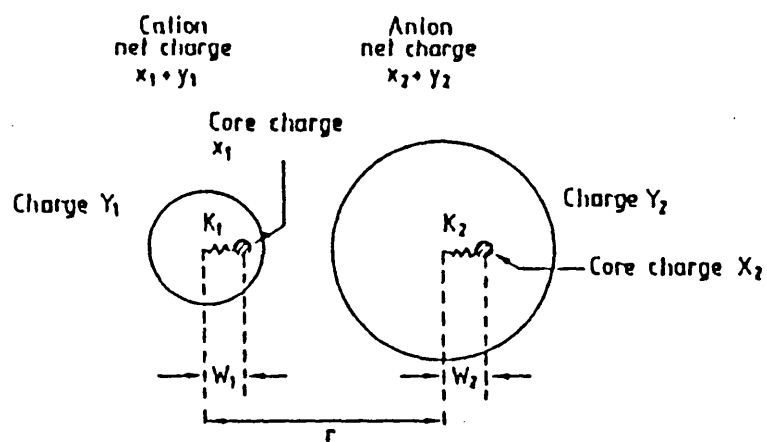
§ Dielectric constants.

Figure 1.6

Schematic diagram of the simple shell model.

**Figure 1.7**

Experimental dispersion curves for NaI compared with predictions of shell model;<sup>26</sup> (----- simple shell model, ——— breathing shell model).



## 1.8.Molecular Dynamics Simulations of Molecular Crystals and Crystalline Ionic Materials

### 1.8.1.Introduction

The majority of simulation studies are done on static systems, where no mention of the effect of thermal motion is made. This is often an adequate description for systems at low or ambient temperature, and can be a good approximation with some solids up to their melting point.

However, in some technologically important materials the operating temperature of the system in which they are used are such that the thermal energy of the constituent particles is of the same order as the energy barrier opposing their motion. Examples of such compounds are super-ionic conductors, such as those associated with solid state batteries, and there is a possibility of fission reactor fuels operating under conditions which may put them in this category. Super-ionic conductors are essentially normal ionic solids which exhibit abnormally high ionic conductivity, which approach the values typical of molten salts at temperatures well below their melting points.

Super-ionic systems have in the past been handled by the use of static methods and have given some useful results. However, these methods do not take into account the diffusion of ions, which may play an important role in these often largely disordered systems.

These static models often require particle transport to be considered in the terms of hopping models, which requires the activation barrier of migration to be considerably greater than  $KT$ . Unfortunately, this latter condition is seldom obeyed in super-ionic systems. For these reasons the molecular dynamics technique, which has been extensively used in studies of liquids, including molten solids, has recently been applied to the study of superionic solids. The following work concentrates on the modifications required to apply this technique to solids.

### 1.8.2.Techniques

In essence, the molecular dynamics technique takes an array of particles, typically 100-1000 in number, to which periodic boundary conditions are applied, and by solving in an iterative manner the



equations of motion of the system, time evolution may be followed. Of course, adequate potentials for the atomic interactions must be provided. In general, the iterative procedure goes as follows; a starting configuration for the assembly of particles is specified at time  $t = 0$ . This means the particles are given spatial coordinates corresponding to known structural data, also velocities are assigned to the particles which reflect the working temperature of the system using average kinetic energy. The forces acting upon the particles are now calculated using the specified potentials. If the velocities and coordinates of the particles at various time increments are now determined, the dynamical properties of the system can be calculated.

Further discussion of molecular dynamics theory is given in refs.17,18 and Chapter 18 ref.1 and discussions of algorithms used are in ref.19.

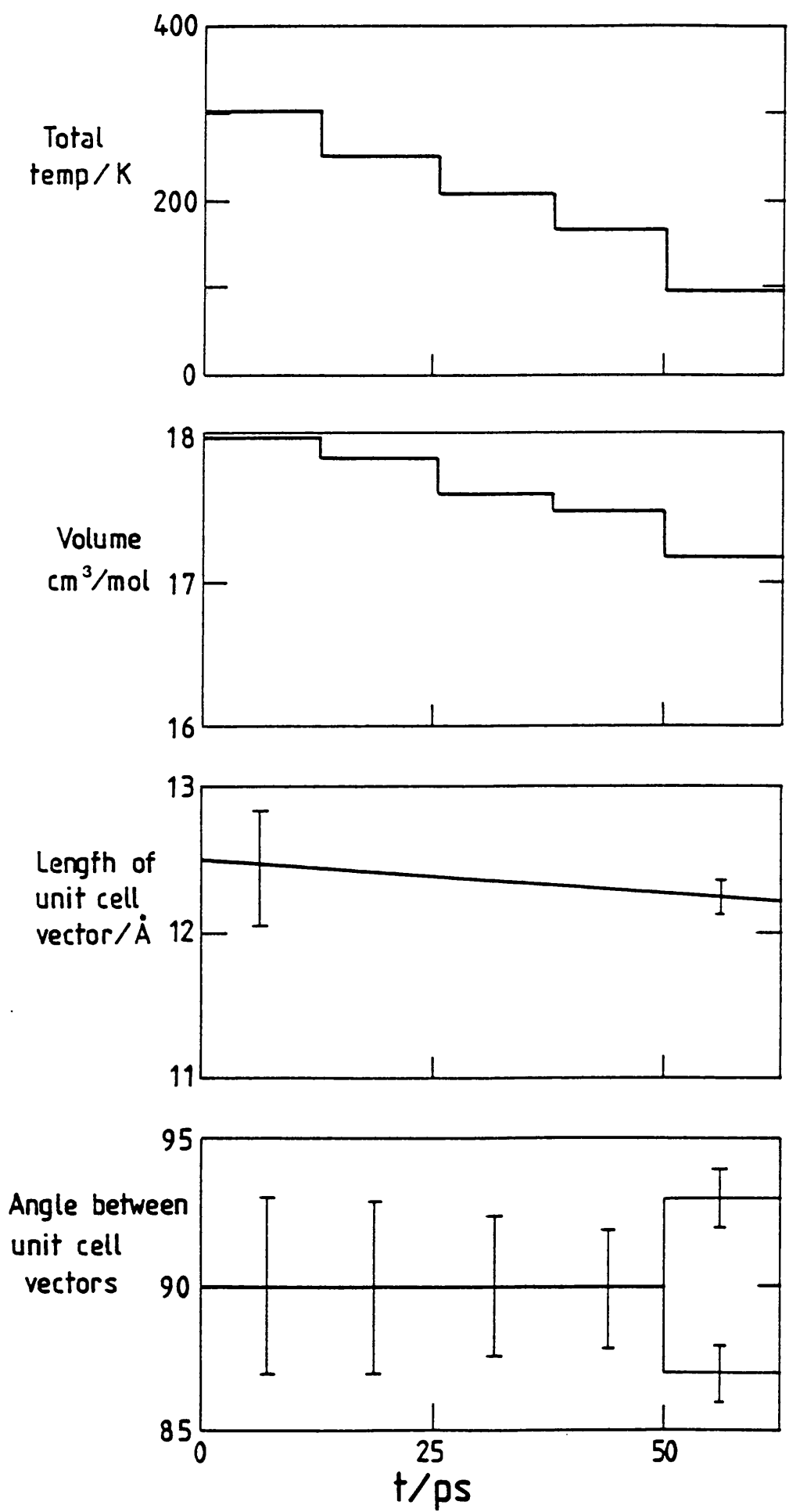
### 1.8.3. Structural Transformations in Solid Nitrogen at High Pressures

What follows is an example of a molecular dynamical (M.D.) calculation achieved by a somewhat advanced approach. It involves a technique proposed by Andersen<sup>20</sup> and then further developed by Parrinello and Rahman.<sup>21</sup> It essentially involves setting up a system at constant pressure and then varying the temperature. This model enables one to observe the variation in unit cell vectors, and the angles between these vectors at any place in P-T space.

The following example by Nosé and Klein<sup>22</sup> shows how with sufficiently refined intermolecular potentials, a series of known phase transitions in solid nitrogen can be calculated. This series of transitions involved setting up a potential at constant pressure, the pressure being 70 kbar, and reducing the temperature from 300 K to 100 K. This results in a cubic-cubic transition at 230 K and more noticeably a cubic-trigonal transition at 140 K. Nosé and Klein showed how various quantities characterising the cubic phase and the trigonal phase varied with temperature, in particular the angle between the unit cell vectors, Fig. 1.8.

Figure 1.8

Time evolution of quantities characterising the basic molecular-dynamics cell used for solid nitrogen at 70 kbar. The last panel, which refers to  $T=100$  K, clearly reveals the trigonal distortion that takes the crystal from  $Pm3n$  to  $R3c$  (After S. Nose and M.L. Klein, 1983).



### 1.9.Pseudopotential Theory

This is a theoretical approach to the study of semiconductors and metals, in particular, "simple" non d- or f- block metals, along with some of their alloys.

Consider the Schrodinger equation for a one electron system

$$[-(\hbar^2/2m)\nabla^2 + V(r)]\psi = E\psi \quad (21)$$

This can be transformed to<sup>23</sup>

$$[-(\hbar^2/2m)\nabla^2 + V(ps)]\phi = E\phi \quad (22)$$

where  $V(ps)$  represents the pseudopotential, and  $\phi$  is the pseudo wavefunction, the eigen value  $E$  is identical to that in equ 21, this approach can also be extended to a many electron system. The central idea of this theory is the reduction of the pseudopotential to a weak, long-range phenomenon by the cancellation of any core related potential  $V(r)$  by the radial oscillations of  $\psi$ . This manifests itself as allowing  $\psi$  and  $\phi$  to be equal outside the atomic core, but inside the core it is a smooth function with all radial nodes of  $\psi$  removed, Fig 1.9. Practically it gives a conceptual framework, where a "nearly free electron" approximation can be used to describe valence electrons in the conduction band.

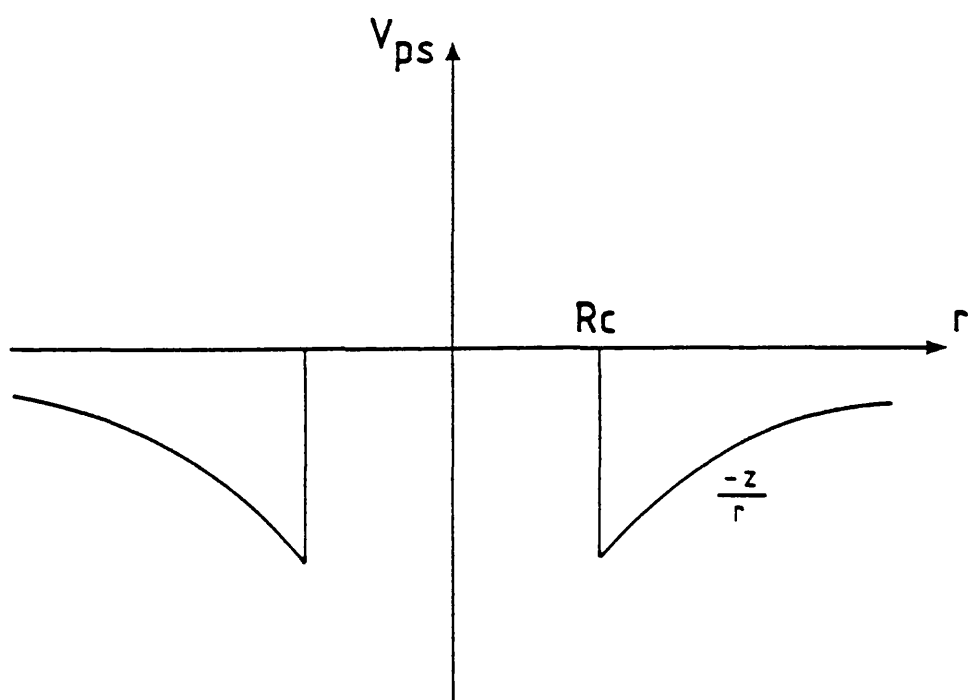
Pseudopotentials are mainly determined by a) the ratio of atomic radius to ion-core radius, and b) the energy difference between the lowest s and p valence states of the atom.

a) shows us that natural links exist between atoms from different rows of the periodic table, and from b), a discussion of structure in terms of pseudopotentials can be made along with dehybridization.

Pseudopotentials have been used consistently in the study of lattice stability and its relation to band structure. Although results were gained, eg. Heine and Weire 1968,<sup>24</sup> and Weire 1968,<sup>25</sup> the theory had many critics. The usual criticism involved its treatment in terms of second order perturbation theory, and that the conditions for this type of treatment were violated due to the basic assumptions of the theory being incompatible.<sup>23</sup> Nevertheless, its achievements are impressive, especially with semiconductors.

Figure 1.9

Schematic representation of a pseudopotential, cancelled off to approximately zero inside the ion-core radius  $R_c$ , and equal to  $-z/r$  outside.  
(From B.J. Austin and V. Heine (1966))



## General conclusions

The theory of solids is currently an area of intense activity in which some remarkably accurate results are being obtained with some of the above models. Much progress is also being made with *ab initio* approaches but it will be some time before they supplant the specialised models. Whatever theories are developed, there will always be a need for good quality experimental data to support and extend them. This is where the main effort of this thesis is directed.

## References

- 1) Catlow, C.R.A. and Mackrodt, W.C., "Computer Simulation of Solids", Springer-Verlag, Berlin, (1982).
- 2) Catlow, C.R.A., Thomas, J.M., Jefferson, D.A. and Parker, S.C. (1982), *Nature*, **295**, 658.
- 3) Catlow, C.R.A. and Norgett, M.J. (1973), *J. Phys.*, **C6**, 1325.
- 4) Catlow, C.R.A., James, R., Mackrodt, W.C. and Stewart, R.F. (1982), *Phys. Rev.*, **B25**, 1006.
- 5) Wedepohl, P.T., (1967), *Proc. Phys. Soc.*, **92**, 79.
- 6) Wedepohl, P.T., (1968), *J. Phys.*, **B1**, 307.
- 7) Gordon, R.G. and Kim, Y.S. (1972), *J. Chem. Phys.*, **56**, 3122.
- 8) Rae, A.I.M. (1973), *Chem. Phys. Lett.*, **18**, 574.
- 9) Cohen, J.S. and Pack, R.T. (1974), *J. Chem. Phys.*, **C12**, 431.
- 10) Mackrodt, W.C. and Stewart, R.F. (1979), *J. Phys.*, **C12**, 431.
- 11) Kitaigorodskii, A.I., "Organic Chemical Crystallography", Consultants Bureau, New York, 1961.
- 12) Mayer, J.E. (1933), *J. Chem. Phys.*, **1**, 270.
- 13) Andzelm, J. and Piela, C. (1977), *J. Phys.*, **C10**, 2269; **11**, 2695, (1978).
- 14) Martin, R.M. (1969), *Phys. Rev.*, **186**, 871.



- 15) Bosawava, I. and Lidiart, A.B. (1967), *Phil. Mag.*, **16**, 805.
- 16) Sangster, M.J. (1974), *J. Phys. Chem. Solids*, **35**, 195.
- 17) Catlow, C.R.A., Corish, J., Diller, K.M., Jacobs, P.W.M. and Norgett, M.J. (1978), *J. Phys.*, **C12**, 451.
- 18) Sangster, M.J. and Dixon, M. (1976), *Adv. Phys.*, **25**, 247.
- 19) Beeman, D. (1976), *J. Compt. Phys.*, **20**, 130.
- 20) Andersen, J. (1980), *J. Chem. Phys.*, **72**, 2384.
- 21) Parrinello, M. and Rahman, A. (1980). *Phys. Rev. Lett.*, **45**, 1196.
- 22) Nosé S and Klein M.L. (1983), *Phys. Rev. Lett.*, **50**, 1207.
- 23) Austin, B.J. and Heine, V. (1966), *J. Chem. Phys.*, **45**, 928.
- 24) Heine, V and Weire, D. (1966), *Phys. Rev.*, **152**, 603.
- 25) Weire, D. (1968), *J. Phys.*, **C1(2)**, 210.

## CHAPTER TWO

### EXPERIMENTAL TECHNIQUES

## CHAPTER TWO

### EXPERIMENTAL TECHNIQUES

#### 2.1.Introduction to the design and use of the diamond anvil cell.

##### 2.1.1.Introduction

There are many different types of measurement made on materials at high pressures, and over the last two decades such studies have become increasingly common. There are now upwards of 3000 papers being published each year on subjects related to high pressure research.<sup>1</sup> The development of high pressure cells suitable for infrared and Raman spectroscopy has recently led to an increasing amount of activity in this field.

Individual descriptions of many different high pressure spectroscopic systems have been published. Stadtmuller, 1976, has discussed over forty different high pressure optical cells.<sup>2</sup>

The simplest and easiest to use are the Bridgman opposed anvil cells, of these the diamond anvil cell(d.a.c.) is probably the most versatile in achieving very high pressures. This type of cell has been used for Raman, mid-infrared and far-infrared spectroscopy and with various modifications, for X-ray diffraction (powder and single crystal). These cells may be used both at high and low temperatures without great difficulty. When working with sample volumes of less than twenty nanolitres and a cell transmission as low as 1%,<sup>3</sup> the success of the system is principally determined by its correct manipulation, and proper coupling to the relevant spectrometer.

##### 2.1.2.An outline of d.a.c. design

An excellent brief history of d.a.c. design is available in Appleby 1977,<sup>4</sup> with particular emphasis on the cells designed for use within the Leicester research group. Appleby also performed a structural analysis

of the Mark IIA cell, using these results to design a much sturdier Mark III cell. The development of the d.a.c. has progressed throughout the group, Williams 1980,<sup>5</sup> and Shaw 1982,<sup>6</sup> have published detailed accounts of computer aided design studies on the stress and deformations experienced by diamond anvils under high pressure. These have given valuable insight into both diamond anvil and d.a.c. design within the group.

The work reported in this thesis has been undertaken using a variety of cells, but mainly of the type MK III "Dynocell", Fig. 2.1, which is capable of extremely high pressures, and for routine work up to 150 kbar the "Diacell", Fig. 2.2, was used.

The samples are placed between opposed diamond anvils of a diameter typically in the range 0.7 mm to 1.2 mm at the working surface. The pressure is generated in the assembled cell by a hydraulic system, transmitting through a moving anvil holder (piston) via the lever arms and presser-plate, thus compressing the sample.

Drawings of the "Dynocell" and "Diacell" used are shown in Fig. 2.3, and Fig. 2.4 respectively.

Light ports beneath each anvil permit the passage of radiation to be transmitted through the diamond anvils and the sample.

The "Diacell" is made from stainless steel, AISI 310 and the "Dynocell" is made from McCreedy's NSOH steel (not oil hardened). The anvil supports are made from tool-steel which is harder than stainless steel. The anvils can be mounted on tungsten carbide inserts, should extremely high pressures be required.

### 2.1.3. Diamonds for high pressure work

The selection of diamonds for use as anvils is discussed fully in Adams and Payne 1974,<sup>7</sup> and Adams and Sharma 1977.<sup>8</sup> Essentially, the diamonds must be without visible defects and should be of type IIA or IIB. The latter type are preferred for Raman spectroscopy due to their lower fluorescence. Testing for unacceptable fluorescence should always be done to rough diamonds before they are cut for anvils.

A good description of the mounting and alignment of the diamonds within the d.a.c. is given by Williams 1980.<sup>5</sup>

The cell is initially aligned at ambient pressure by the use of Newton's fringes. The cell is now checked under pressure by the visual observation of low pressure phase transitions when the cell is in an ungasketed mode. Since the pressure distribution across the faces of

Figure 2.1

Photograph of a MKIII "Dynocell", used in studies to very high pressures (ca. 0.5 Mbar).

Figure 2.2

Photograph of a "Diacell", used in studies up to 150 kbar.



Figure 2.3

The Dynocell outline and a section of the central insert.

Parts labelled are:

1. Cell body
2. Central insert
3. Fixed anvil holder
4. Moving anvil holder
5. Presser plate
6. Lever arms
7. Piston plate
8. Hydraulic ram
9. Knurled backing screw
10. Central pivot
11. Piston screw
12. V block assembly

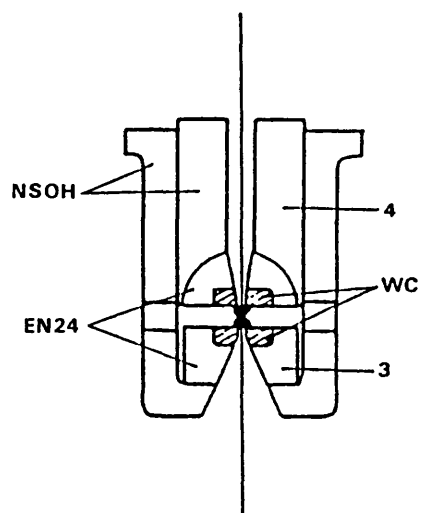
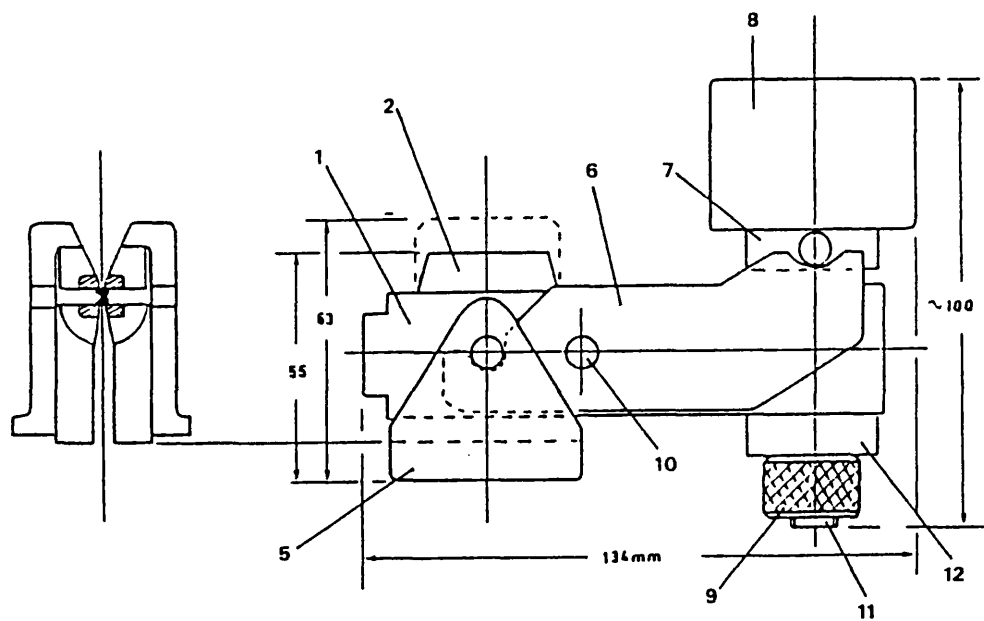


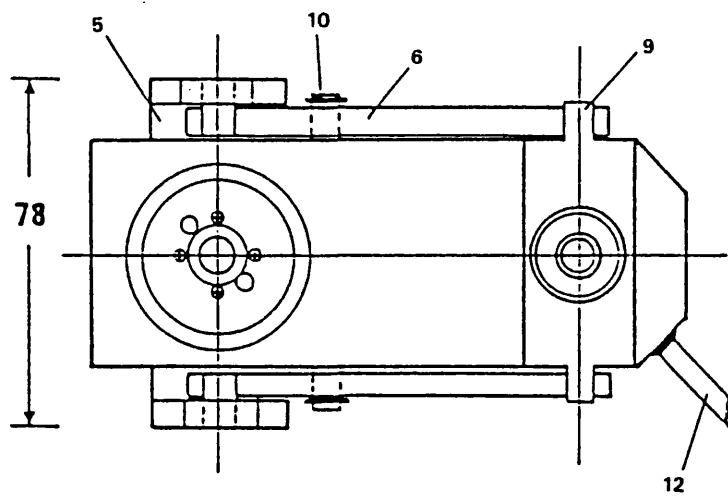
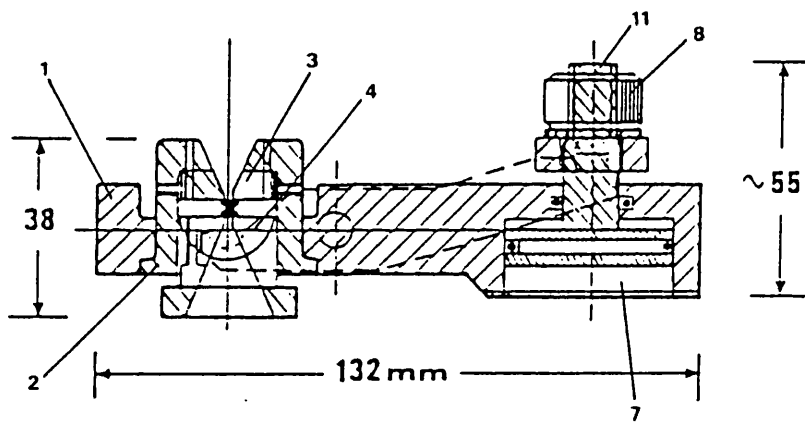


Figure 2.4

The Diacell outline side and top view.

Parts labelled are:

1. Cell body
2. Central insert
3. Fixed anvil holder
4. Moving anvil holder
5. Presser plate
6. Lever arms
7. Internal hydraulic ram
8. Knurled backing screw
9. Piston plate
10. Central pivot
11. Piston screw
12. Oil feed for hydraulic ram



the diamond anvils is approximately parabolic, with maximum pressure experienced in the middle, falling to ambient at the edges the appearance of symmetric and concentric phase boundaries initiating from the centre would be expected for a correctly aligned cell. The materials which are used for such alignment include  $\text{HgI}_2$  (phase transition at 13.0 kbar) and  $\text{AgI}$  (phase transitions at 4.0 and 98.0 kbar).

#### 2.1.4. Use of the d.a.c.

When the cell has been correctly aligned it may be used in an ungasketed mode wherein the sample is placed between the anvil faces and pressure is applied, resulting in the afore mentioned pressure gradient. When used in this mode problems in spectral interpretation occur due to peak broadening and the possibilities of multiphase systems.

A hydrostatic pressure may be attained by sealing the sample and a pressure transmitting fluid within a metal gasket placed between the two anvil faces. The materials commonly used in producing gaskets are inconel (a Fe/Cr/Ni heat resisting alloy), molybdenum and stainless steel and are generally 0.05-0.075 mm thick for infrared or 0.2 mm thick for Raman work. The diameter of the hole may be between 0.2 mm and 0.6 mm depending on the spectroscopic technique used. Methods of loading are described in detail by Williams 1980.<sup>5</sup>

As well as the sample a microscopic grain of ruby is placed within the gasket hole as a pressure calibrant. The ruby R-line method is used for pressure calibration, where the  $R_1$  and  $R_2$  fluorescence lines of ruby are monitored as they move linearly with pressure at  $0.76 \text{ cm}^{-1} \text{ kbar}$ ,<sup>9,10</sup> certainly to 200 kbar and possibly to very much higher pressures.<sup>11</sup>

The ruby R-line method is particularly useful as a pressure calibrant as broadening of the two fluorescence lines or variation in frequency separation are indicative of a lack of hydrostaticity in the sample compartment.

#### 2.1.5. Use of the d.a.c. in Raman and mid-infrared spectroscopy

The method of coupling a d.a.c. to a Coderg T800 Raman spectrometer via an off axis ellipsoid mirror has been given in detail previously.<sup>12</sup>

A discussion of the optical problems associated with infrared spectroscopy at very high pressures has been given,<sup>8</sup> with reported improvements made by coupling to the Perkin-Elmer 580 I.R. spectrophotometer also reported.<sup>13</sup>

## 2.2.The use of spectral deconvolution routines

In our Raman studies, as in most kinds of spectroscopy, we find that the spectra often contain bands whose envelopes indicate two or more unresolved components. Since two bands are considered resolved by Rayleigh's criterion, when two lines separated by the resolution interval would give a minimum in intensity between the lines equal to 0.81 of the intensity at the line maxima. Under this definition, a side band that appears as a shoulder on another band is not considered resolved; this is often the case in Raman spectroscopy.

Information from these unresolved envelopes may be gained from the application of computer-generated deconvolution routines. These routines rely upon the combination of bands to simulate actual spectra. The deconvolution routine used in this work is interactive in type. It requires the operator to adjust the parameters (peak position, height, half-band width and percentage Gaussian) in an iterative manner until a suitable fit is achieved.

In the case of Raman spectroscopy all peaks are considered to be Lorentzian (which corresponds to 0.0% Gaussian in our program). If  $I(\omega)$ , the "sharp line frequency", is subjected to an exponentially decaying dipole correlation function, as in the case of Raman spectroscopy, then the new functional dependence of  $I(\omega)$  is called a Lorentzian lineshape.

An interactive technique such as this has inherent pit-falls, mainly based on the philosophy of "rubbish in-rubbish out". This implies that if the original premiss was incorrect then the end product is unlikely to be sensible. Any additional bands may be introduced when all reasonable combinations of the existing ones have been used. We often have some idea of the number, position and intensity of some or all of the bands present, enabling a good fit to be produced with only a few minor alterations.

Fortunately, subsequent experiments have proven the validity of deconvolution techniques. This enables us to use the results gained from this technique to suggest reasonable mechanisms for phase transitions based upon a spectral interpretation.

### 2.2.1. Technical details

Only data which is presented in a digitised form may be subjected to our deconvolution routines. This data is gained either by direct collection of spectra from a computer aided device or by the use of a standard digitiser.

The deconvolution routine used was:

Spirit written by N. Pay, department of Chemistry, and supplied by the University of Leicester Computer department.

### 2.3. Classification of Phase transitions

The purpose of this thesis is not the detailed discussion of phase transition theories, however, a limited discussion of some of the commonly used terms and concepts would be helpful.

A solid undergoes a phase transition when a particular phase of this solid becomes unstable under a given set of thermodynamic conditions. During a phase transition, whereas the free energy of a system remains continuous, thermodynamic quantities such as entropy, volume, heat capacity and so on, undergo discontinuous changes. Ehrenfest,<sup>14</sup> classified phase transitions on the basis of the dependence of their thermodynamic quantities undergoing the discontinuity with respect to the Gibbs free energy function. In this scheme, a system is said to be of the same order as the derivative of the Gibbs free energy which shows a discontinuous change at the transition.

The Gibbs free energy is given by

$$G = H - TS = U + PV - TS$$

Hence  $dG = VdP - SdT$

The first and second derivatives of the free energy may be written as

$$(\partial G / \partial P)_T = V \quad (\partial G / \partial T)_P = -S$$

$$(\partial^2 G / \partial P^2)_T = (\partial V / \partial P)_T = -V\beta \quad (\partial^2 G / \partial P \partial T) = (\partial V / \partial T)_P = V\alpha$$

$$(\partial^2 G / \partial T^2)_P = -(\partial S / \partial T)_P = -C_P / T$$

Where,  $C_P$ ,  $\alpha$  and  $\beta$  are the heat capacity, volume thermal expansivity, and compressibility respectively. We readily see that discontinuous changes in volume and entropy belong to the first order and that the remainder belong to the second order.

When considering the variation of phonon frequency with pressure or temperature, we observe that it parallels the behaviour of a first order system, insofar as the plot of frequency verses temperature or pressure in first order systems are generally associated with discontinuities in slope. However, the situation is more complicated in reality and is more akin to symmetry than thermodynamic considerations.

### 2.3.1 Landau's theory of second order phase transitions

Landau<sup>15</sup> proposed a theory which could account for the discontinuity of the heat capacity and the thermal expansivity at a transition during a second order transition. The transition from a high temperature phase to a low temperature phase corresponds to an ordering process. In the ordered, less symmetrical (low temperature) phase of the material, it is possible to identify a long range ordering parameter, which decreases continuously with temperature and becomes zero at the transition temperature. The disordered high temperature phase has the highest symmetry. Therefore, the free energy may be expressed in terms of an order parameter,  $\xi$ . The mathematical foundation for the above statement is provided in refs. 16 & 17.

### 2.3.2. Symmetry changes at phase transitions

The question to be asked on this point is as follows: given a crystal whose symmetry group is  $G_0$ , which symmetry group may be achieved by this crystal on undergoing a continuous phase change (second order)? A solution to this problem is given in by Landau's theory.<sup>15</sup> It is apparent that this theory contains two interweaving threads, one concerning the symmetry changes at the transition, and the other the behaviour of the thermodynamic potential in the vicinity of the critical point. However, we are concerned with the symmetry relationship only in this passage. It is assumed that the symmetry of the high temperature phase is determined by a known space group  $G_0$  and that of the low

temperature phase by some unknown space group  $G_1$ . These two phases will show a direct symmetry relationship manifesting in a sub-group/super-group relationship. The different type of subgroup available, zellengleich (crystal cell preserving), klassengleich (crystal class preserving) and allgemein (general) were designated by Hermann.<sup>18</sup>

In the event of a first order phase transition there will not be a direct symmetry relationship, resulting initially in no apparent pathway between the two structures. However, Boyle *et.al.*<sup>19</sup> described a system where several stages of descent and ascent in symmetry may construct a relationship between two crystal structures.

The reproducibility of phase transitions insists that there be a certain defined pathway which the atoms follow. To produce absolutely random arrangements of atoms at a transition is probably more energetically difficult than to allow the use of more symmetrical pathways.

## References

- 1) Merrill, L. (1981), "Bibliography on High Pressure Research", Brigham Young University.
- 2) Stadtmuller, A.A. (1976), M. Phil. Thesis, University of London, King's College.
- 3) Adams, D.M. and Sharma, S.K. (1977), *J. Phys. E.*, **10**, 680-2.
- 4) Appleby, R. (1977), Ph.D. Thesis, Leicester University.
- 5) Williams, A.D. (1980), Ph.D. Thesis, Leicester University.
- 6) Shaw, A.C. (1982), Ph.D. Thesis, Leicester University.
- 7) Adams, D.M. and Payne, S.J. (1974), *J. Chem. Soc. (Farad. Trans. II)*, **70**, 1959-66.
- 8) Adams, D.M. and Sharma, S.K. (1977), *J. Phys. E.*, **10**, 838-42.
- 9) Adams, D.M., Appleby, R. and Sharma, S.K. (1976), *J. Phys. E.*, **9**, 1140-4.
- 10) Piermarini, A.J., Block, S., Barnett, J.D. and Formann, R.A. (1975), *J. Appl. Phys.*, **46**, 2774-80.
- 11) Mao, H.K., Bell, P.M., Shaner, J.W. and Steinberg, D.J. (1978), *J. Appl. Phys.*, **49**, 3276-83.
- 12) Adams, D.M., Sharma, S.K. and Appleby, R. (1977), *Applied Optics*, **16**, 2572-5.
- 13) Adams, D.M. and Sharma, S.K. (1979), *Applied Optics*, **18**, 594-5.



- 14) Ehrenfest, P. (1933), *Proc. Amsterdam Acad.*, **36**, 153.
- 15) Landau, L.D. and Lifshitz, E.M., "Statistical Physics," Pergamon Press, Oxford, 1959.
- 16) Krivoglaz, M.A. and Smirnov, S.S., "The Theory of Order-Disorder in Alloys," Macdonald, London, 1964.
- 17) Sato, H., in "Physical Chemistry, An Advanced Treatise," vol.10, Academic Press, New York, 1970.
- 18) Herman, C., (1929), *Zeits fur Krystall.*, **69**, 533-555.
- 19) Boyle, L.L. Walker, J.R. and Wanjie, A.C., (1980), *Faraday Discussion*, **69**, 115-119.

## CHAPTER THREE

A RAMAN SCATTERING STUDY OF MSCN COMPOUNDS (M = K,Rb,Cs & NH<sub>4</sub><sup>+</sup>)

AT HIGH PRESSURES

## CHAPTER THREE

### A RAMAN SCATTERING STUDY OF MSCN COMPOUNDS (M = K, Rb, Cs, $\text{NH}_4^+$ ) AT HIGH PRESSURE

#### 3.1. Potassium Thiocyanate (KSCN) and Rubidium Thiocyanate (RbSCN)

##### 3.1.1. Introduction

###### **Potassium Thiocyanate:**

The structure of potassium thiocyanate II, the ambient phase, was first deduced by Klug 1933<sup>1</sup> and then by Büssen et al. 1934.<sup>2</sup> Both concluded that KSCN has an orthorhombic structure, space group  $D_{2h}^{11}$  (Pbcm no. 57) with a tetramolecular primitive cell. A further refinement<sup>3</sup> differs significantly from the original structure determinations only in the position of the carbon atoms. The structure consists of potassium ions at the centre of a distorted square antiprism with four sulphur atoms and four nitrogen atoms occupying the vertices, Fig.3.1a).

Potassium thiocyanate II has been subjected to several investigations by infrared and Raman spectroscopy. Early studies<sup>4,5,6</sup> centred around the internal modes, with later investigations<sup>7,8,9</sup> giving detailed discussions of both internal and external modes, along with a full factor group analysis, Table 3.1.

Previous studies of potassium thiocyanate at conditions other than standard temperature and pressure have revealed the existence of five stable phases, all of them accessible only at elevated temperatures, Fig. 3.2. Bridgman 1915<sup>10</sup> studied KSCN at temperatures and pressures up to 473 K and approximately 12 kbar, where he detected the high temperature order-disorder transition at 413 K and 1 bar. His interpretation of the results led him to believe that the transition was of first-order with a very small accompanying volume change. However, later work<sup>11,12</sup> based on dilatometric, DTA and heat capacity measurements suggested it was a lambda-type transition of second order. A further detailed study of the phase behaviour KSCN<sup>13</sup> using DTA supported the transition II/I being second-order and further reported no observable hysteresis. An attempt using X-ray diffraction techniques

Figure 3.1a)

The crystal structure of ambient MSCN

M = Rb & K (a/b projection).

They exhibit the orthorhombic space group

$D_{2h}^{11}$ , Pbcm, Z = 4.

Lattice parameters:

KSCN a =  $6.673 \pm 0.003$

b =  $6.715 \pm 0.003$

c =  $7.543 \pm 0.005$

RbSCN a = 6.911\*

b = 6.846

c = 8.024

All dimensions in Ångstroms.

(\* Ti and Kettle private communication).

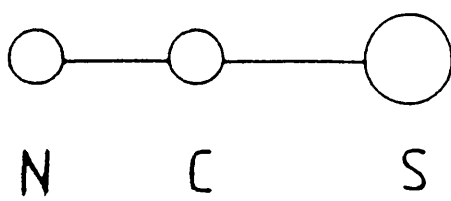
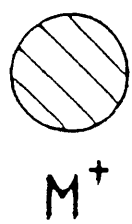
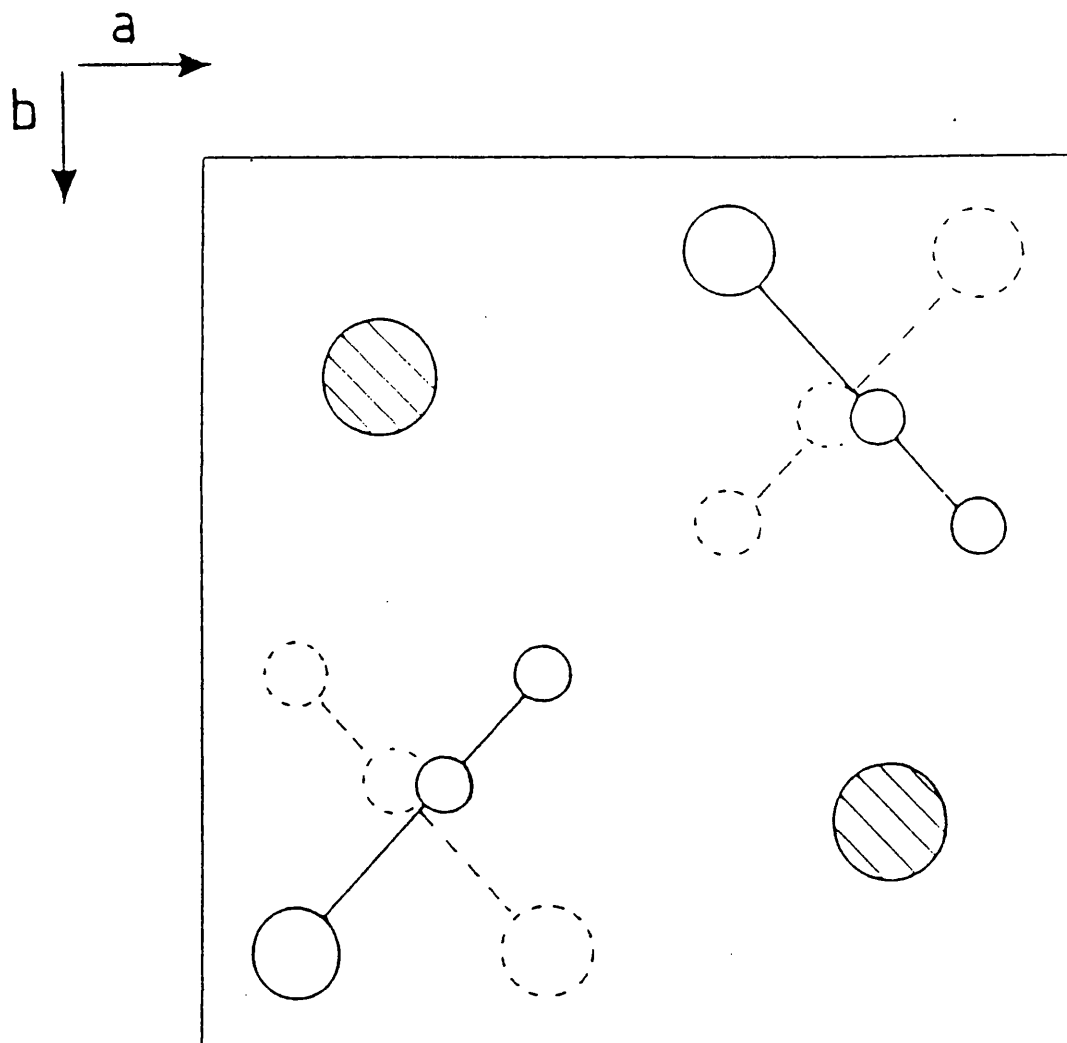


Figure 3.1b)

The crystal structure of KSCN and RbSCN  
at i) room temperature and ii) high  
temperature.

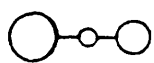
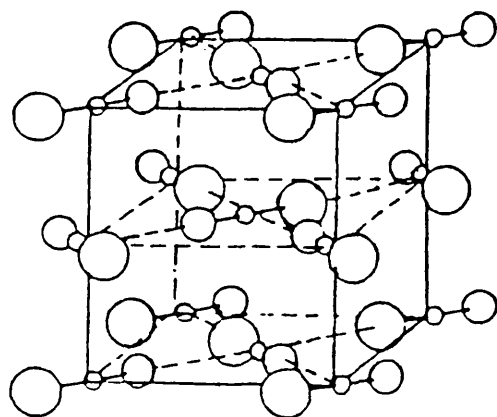
High temperature data:

Space group, tetragonal,  $D_{4h}^{18}$ ,  $Z = 2$ .

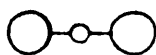
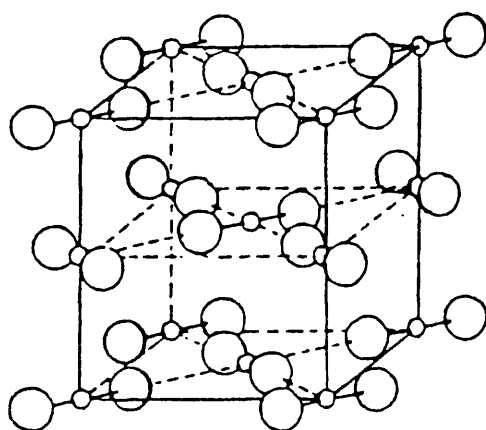
Lattice parameters

$a = b = 6.70 \text{ \AA}$

$c = 7.73 \text{ \AA}$ .



S C N



$\frac{1}{2}(N+S)$  C  $\frac{1}{2}(N+S)$

Table 3.1. Factor group analysis of MSCN crystals (M = K, Rb)

$D_{2h}^{11}$	N	T'	T	R	$\Gamma_{SCN}$	i.r.	Raman
$A_g$	7		3	1	3		xx, yy, zz
$B_{1g}$	8		4	1	3		xy
$B_{2g}$	5		3	1	1		xz
$B_{3g}$	4		2	1	1		yz
$A_u$	4		2	1	1		
$B_{1u}$	5	1	2	1	1	Tz	
$B_{2u}$	8	1	3	1	3	Ty	
$B_{3u}$	7	1	2	1	3	Tx	

Table 3.2. Correlation between the molecular and factor group modes of  $NSC^-$  ion.

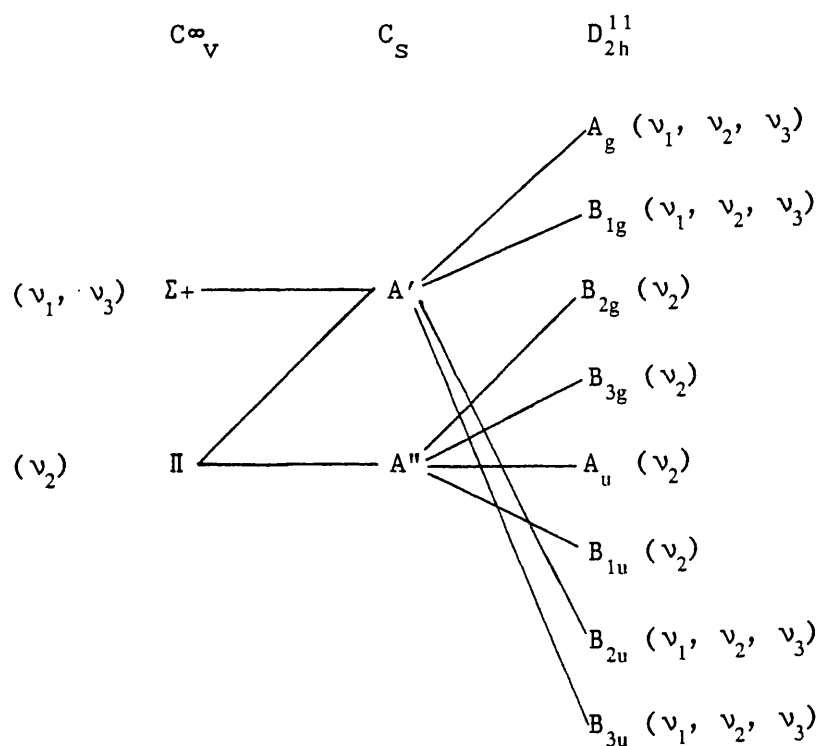
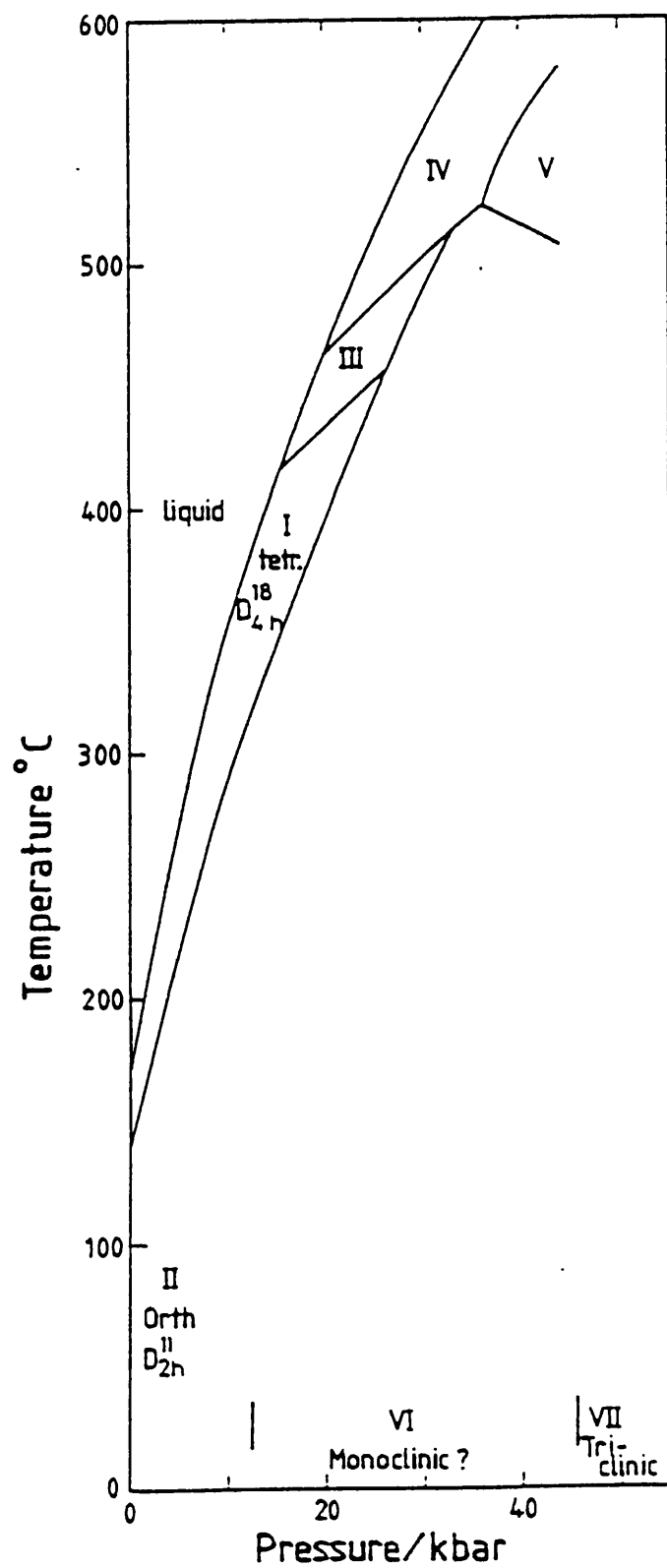




Figure 3.2

Phase diagram of potassium thiocyanate,  
showing the new phases revealed by this  
work.



was made to confirm the suggested mechanism for the transition II/I, described as an order-disorder type involving the orientation of the rod-shaped thiocyanate ions.<sup>14</sup> This study yielded a tetragonal space group for KSCN I of  $D_{4h}^{18}$  (I4/mcm no. 140) with a bimolecular unit cell, which is apparently isostructural with  $KN_3$ , Fig.3.1 b).

Further transitions at elevated temperatures and pressures were detected in a narrow range close to the liquid-solid boundary. The KSCN I/III transition yielded similar DTA signals to those associated with KSCN II/I<sup>13</sup> but again no observable hysteresis was detected. This suggests that the I/III transition may be a lambda-type transition of higher order similar in nature to the II/I transition. In such a case it probably involves a further step in the disordering of the lattice through increased thermal vibration.

Further increases in temperature and pressure result in the appearance of another solid phase, designated KSCN IV. Although the DTA signals were considerably stronger than those associated with the other transitions, suggesting some first-order character, it is still thought to be a further step in the thermal disordering of the lattice. Finally, KSCN IV gave way to a new solid phase, KSCN V, which possesses a density somewhere between those of phases IV and II. However, no attempt at determining the nature or the mechanism of the transition has been given.<sup>13</sup>

No polymorphic behaviour of KSCN at room temperature and elevated pressure has been reported in the literature, although Bridgman<sup>10</sup> studied KSCN up to approximately 12 kbar at 293 K and detected no anomalous volume change. There are no known studies at temperatures substantially below room temperature.

This present study is concerned with the phase behaviour of KSCN to much higher pressures than previously attained, at room temperature. It has revealed two phase transitions, 12.5 kbar and 45.5 kbar, both at 298 K. They have both been analysed on the basis of a second order mechanism.

#### Rubidium Thiocyanate:

Rubidium thiocyanate is isostructural with KSCN II as determined by X-ray diffraction techniques<sup>8,15</sup>, where reflections consistent with the space group  $D_{2h}^{11}$  (Pbcm no. 57) were obtained, and the lattice parameters are  $a = 6.842$ ,  $b = 6.895$  and  $c = 8.019$  Å, Fig. 3.1 a).

Detailed single crystal Raman and infrared data of RbSCN has been

obtained,<sup>8</sup> good agreement with factor group predictions was reported.

Previous studies of the polymorphic behaviour of RbSCN are somewhat limited.<sup>15</sup> They are confined to the investigation of the high temperature solid-solid phase transition at 437 K and the solid-liquid phase boundary up to 40 kbar. The transition at 437 K is considered to be analogous to the KSCN II/I transition. Although no further work on RbSCN has been attempted it would be reasonable to assume that its phase behaviour would follow closely that of KSCN.

This present work has attempted to detect changes at room temperature and high pressure which may be similar to those found in KSCN. We have been successful in identifying two transitions, at 10.5 kbar and 37.5 kbar, both at 293 K. These transitions are also analysed on the basis of a second order mechanism.

### 3.1.2.Experimental

Analar grade KSCN was used (after first drying at 373 K) in a diamond anvil high pressure cell. Pressures were estimated by the ruby R-line method. The samples were contained within stainless steel or inconel gaskets with initial dimensions 0.4 mm diameter and 0.2 mm thick. Spectra were obtained with 488.0 nm and 514.5 nm Ar<sup>+</sup> radiation of approximately 400–700 mW power at the sample.

All modes except  $\delta(\text{NCS})$  and  $2 \times \delta(\text{NSC})$  were followed, these two regions being too weak to observe at high pressure.

RbSCN was synthesised by a double decomposition reaction between barium thiocyanate and rubidium sulphate. The sample of RbSCN was then recrystallised twice from aqueous solution and dried at 373 K for two days. Other experimental details for RbSCN are as for KSCN above.

### 3.1.3.Assignment of the Raman Spectrum for KSCN II

KSCN has a tetramolecular unit cell in which both anions and cations are to be found on sites of  $C_s$  symmetry.<sup>8</sup> Factor group analysis, Table 3.1, reveals that there are 24 Raman-active and 21 infrared-active vibrational modes. In the i.r. there are 7 and in the Raman there are 8 vibrations of the thiocyanate ions (Table 3.2 shows the correlation between molecular and factor group modes of  $\text{NCS}^-$  ion): the remainder are lattice modes. The predicted number of Raman-active internal modes has been observed for KSCN, Table 3.3 a). They are represented by the strong  $\nu_1$ ,  $\nu(\text{CN})$  doublet, the medium strength  $\nu_3$ ,  $\nu(\text{SC})$  doublet and the weak

**Table 3.3(a).** Raman-active internal mode frequencies of  
MSC(M = K, Rb).

Symmetry species	KSCN			RbSCN		
	$\nu_1$	$\nu_2$	$\nu_3$	$\nu_1$	$\nu_2$	$\nu_3$
A <sub>g</sub>	2050	485	749	2050	482	748
B <sub>1g</sub>	2053	485	750	2051	482	749
B <sub>2g</sub>	--	476	--	--	477	--
B <sub>3g</sub>	--	479	--	--	478	--

$\nu_1$ : The C-N stretching frequency.

$\nu_2$ : The S-C-N bending frequency.

$\nu_3$ : The C-S stretching frequency.

**Table 3.3(b).** Raman-active external mode frequencies of  
MSCN (M = K, Rb).

Symmetry species	Frequencies in cm <sup>-1</sup> .					
4A <sub>g</sub>	KSCN	144	122	96	78	
	RbSCN	132	119	67	48	75 (2-phonon)
5B <sub>1g</sub>	KSCN	124	112		98	68 145(2-phonon)
	RbSCN	124	99	72	65	48 153(2-phonon)
4B <sub>2g</sub>	KSCN	122	96	87	66	
	RbSCN	111	100	54	48	
3B <sub>3g</sub>	KSCN	126	112	68		
	RbSCN	124	99	49		

$\nu_2$ ,  $\delta(\text{SCN})$  region consisting of four possible bands.

The external mode region of KSCN is strong but complicated and is therefore difficult to resolve, but a combination of data from single crystal polarised Raman spectra<sup>8</sup> and deconvolution routines allow us to evaluate the contents of the broad envelopes, Table 3.3 b).

Since RbSCN is isostructural with KSCN II the correlation sequence and the factor group analysis will be identical, Table 3.1 and 3.2. The lattice modes follow a similar overall pattern of intensity and position to those in KSCN. However, some of the external modes are seen to be cation-mass sensitive, these are likely to be translational modes, as rotational modes will have predominant contributions from  $\text{NCS}^-$  librations, Table 3.3 b). Internal modes are again similar to those in KSCN, differing only slightly in position, Table 3.3 a). The observed correlation field splitting in RbSCN is weaker than that of KSCN, since the increased unit cell dimensions reduce possible intermolecular coupling.

#### 3.1.4. High Pressure Results

##### **Potassium Thiocyanate:**

Representative Raman spectra of the lattice modes, Fig. 3.3, and internal modes, Fig. 3.4, at various pressures are given along with mode shifts with pressure, Figs. 3.5 a)-d) and Tables 3.4 a) & b).

It can be concluded from these figures, that there is evidence for two phase changes, one at 12.5 kbar and one at 45.5 kbar. The first of these two is fairly subtle with the clearest indication coming from a break in the plot of pressure versus  $\nu_{\text{CN}}$ , and the two lowest lattice modes, which show a change of slope at the phase boundary. The second transition is perhaps the most obvious, being indicated by the reduction in the gradient of all the  $d\nu/dP$  plots, and the increase in the separation of the  $\nu_{\text{CN}}$  doublet.

##### **Rubidium Thiocyanate:**

RbSCN also shows evidence for two phase transitions, one at 10.5 kbar and one at 37.5 kbar. The changes at both transitions are, again, subtle but combined evidence from all the plots, Figs. 3.6 a) & b), Tables 3.5 a) & b) and spectra, Figs. 3.7, leaves little doubt as to their existence. The clearest evidence is from the mode changes associated with the bands initially at 134.8 and 153  $\text{cm}^{-1}$ .

The number of bands in each compound and in each phase remains the

**Table 3.4(a).** Pressure dependencies of the Raman-active lattice modes of KSCN.

	<u>Phase II</u>	<u>Phase VI</u>	<u>Phase VII</u>
$\nu_i = 69.0$	0.18	0.315	0.025
71.6	1.28	0.515	0.063
89.2	0.88	0.977	-----
98.25	0.982	1.115	0.083
114.5	1.358	1.30	-----
124.2	1.298	1.309	0.277
128.5	1.819	2.027	0.242
144.2	2.028	2.04	0.233

**Table 3.4(b).** Pressure dependencies of the Raman-active internal modes of KSCN.

	<u>Phase II</u>	<u>Phase VI</u>	<u>PhaseVII</u>
$\nu_i = 740.4$	0.704	0.480	0.132
745.0	0.752	0.518	0.122
748.4	0.672	0.511	0.132
2046.4	0.4	0.669	0.062
2049.1	0.39	0.712	0.057

$\nu_i$ : Initial frequencies of the vibrational mode at 0.001 kbar ( $\text{cm}^{-1}$ ).

Pressure dependencies  $d\nu/dP$  in  $\text{cm}^{-1}\text{kbar}^{-1}$ .

Figure 3.3

The deconvoluted external mode spectra of the three room temperature phases of potassium thiocyanate.



Intensity ↑

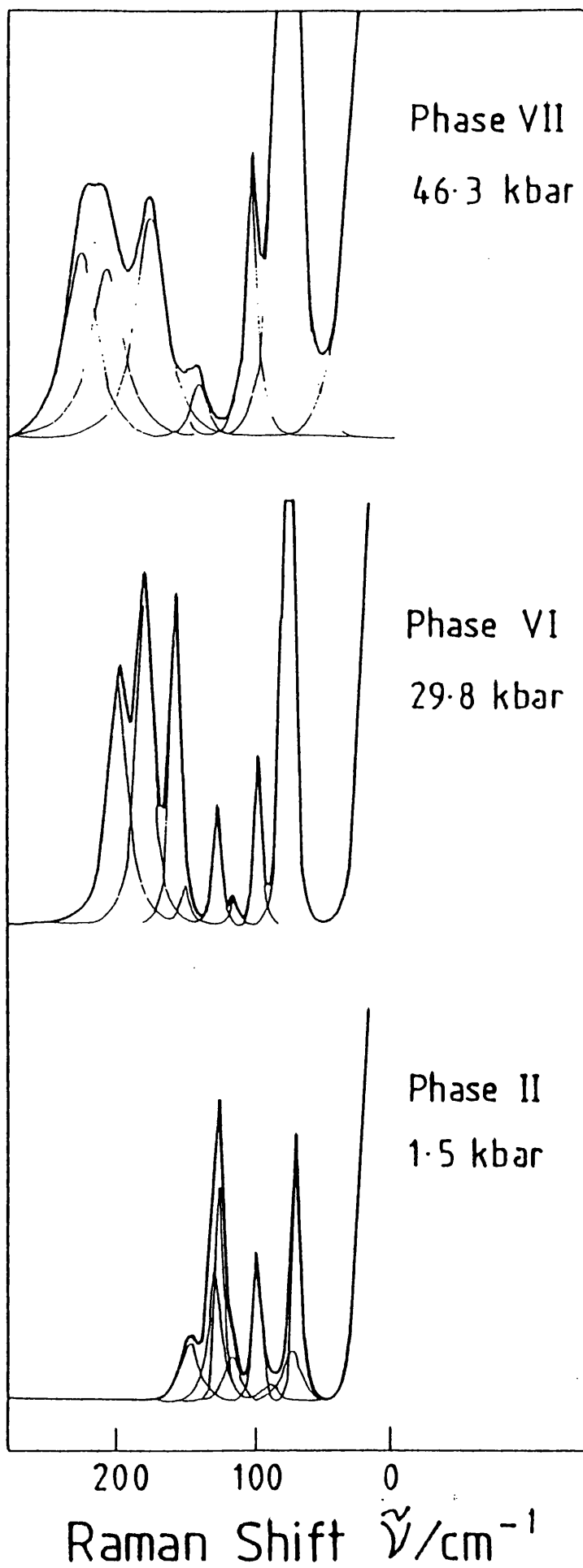


Figure 3.4

The deconvoluted internal mode spectra of the three room temperature phases of potassium thiocyanate.

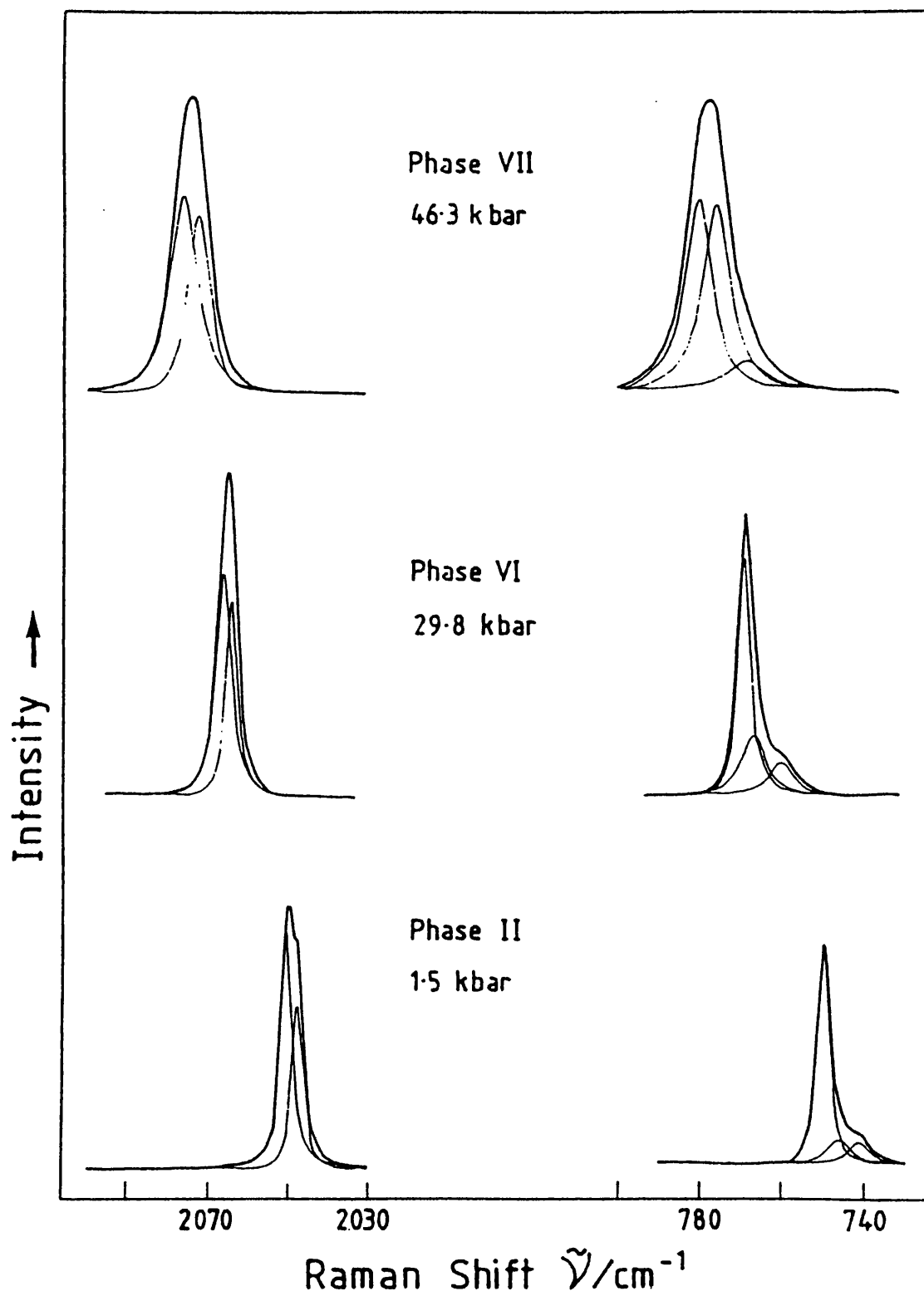


Figure 3.5a)

Plot of frequency ( $\text{cm}^{-1}$ ) against pressure  
for the Raman-active  $\nu_3$  S-C stretch  
region in potassium thiocyanate.

Figure 3.5b)

Plot of frequency ( $\text{cm}^{-1}$ ) against pressure  
for the Raman-active  $\nu_1$  C-N stretch  
region.

All solid lines and error bars were  
obtained by the method of least squares.

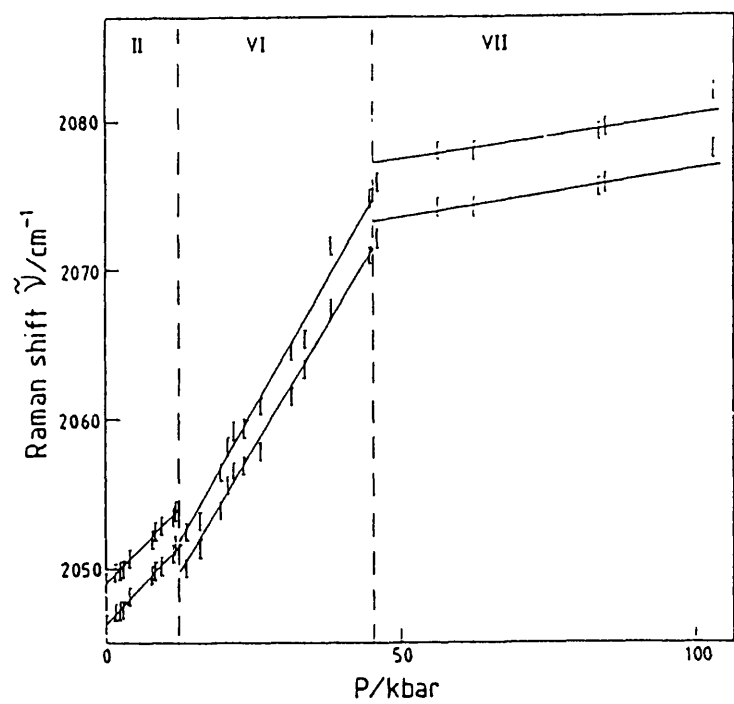
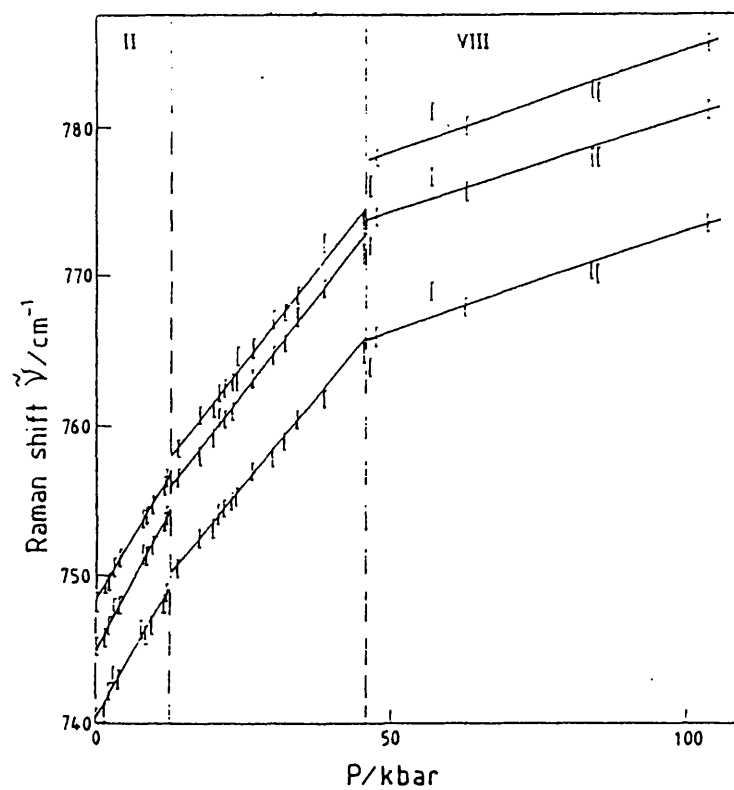
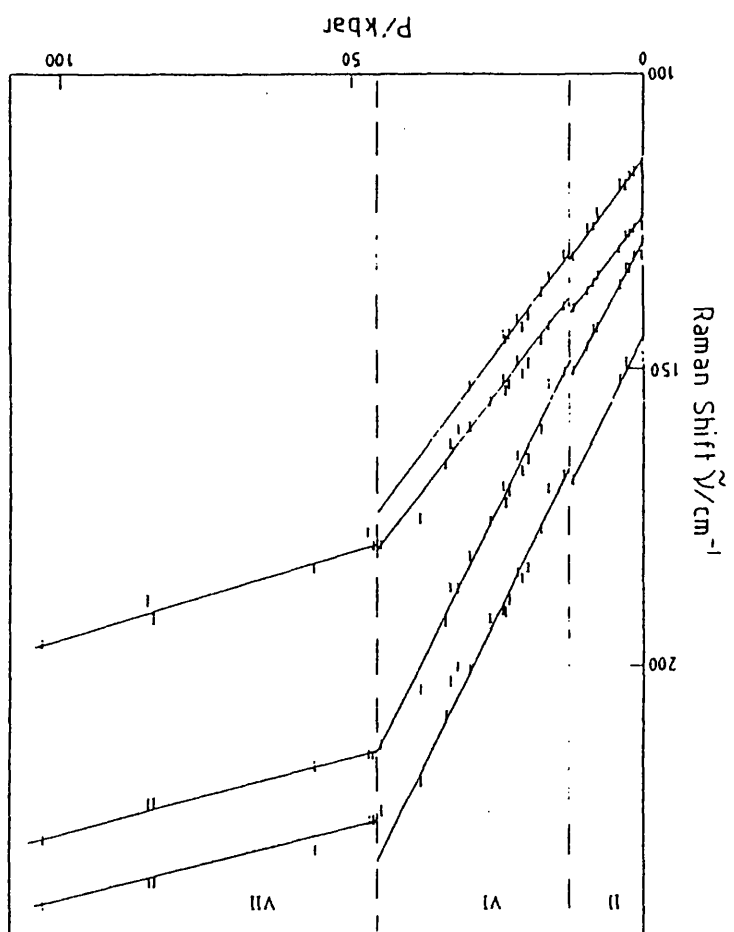
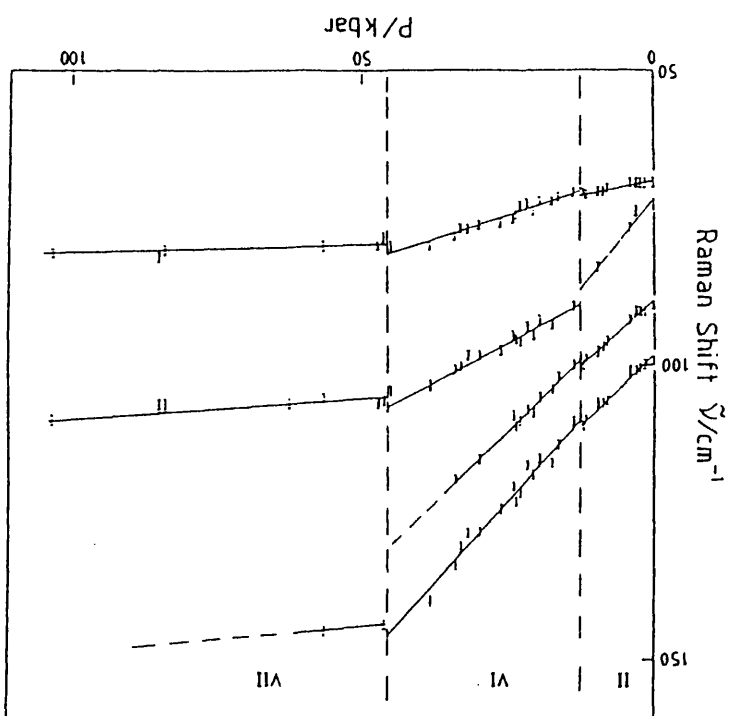


Figure 3.5c) & d)

Plot of frequency ( $\text{cm}^{-1}$ ) against pressure  
for the Raman-active external modes in  
potassium thiocyanate.



**Table 3.5(a).** Pressure dependencies of the Raman-active external modes of RbSCN.

	<u>Phase I</u>	<u>Phase III</u>	<u>Phase IV</u>
$\nu_i = 48.0$	0.024	-0.063	-0.013
53.5	-0.048	-0.175	-0.011
65.6	0.476	0.289	0.154
74.7	1.276	1.15	0.340
99.7	1.267	1.288	0.500
110.3	1.143	1.302	0.460
118.0	1.619	1.320	0.655
124.5	1.639	1.273	0.667
	-----	-----	0.869
134.8	1.654	1.520	1.024
153.0	1.095	1.160	0.857

**Table 3.5(b).** Pressure dependencies of the Raman-active internal modes of RbSCN.

	<u>Phase I</u>	<u>Phase III</u>	<u>Phase IV</u>
$\nu_i = 740.0$	0.643	0.520	0.520
742.75	0.829	0.540	0.540
748.0	0.635	0.620	0.560
2048.5	0.476	0.470	-----
2052.3	0.470	0.500	0.380
2054.75	0.333	0.490	0.520

$\nu_i$ : Initial frequency of the vibrational mode at 0.001 kbar ( $\text{cm}^{-1}$ ).

Pressure dependencies  $d\nu/dP$  in  $\text{cm}^{-1}\text{kbar}^{-1}$ .

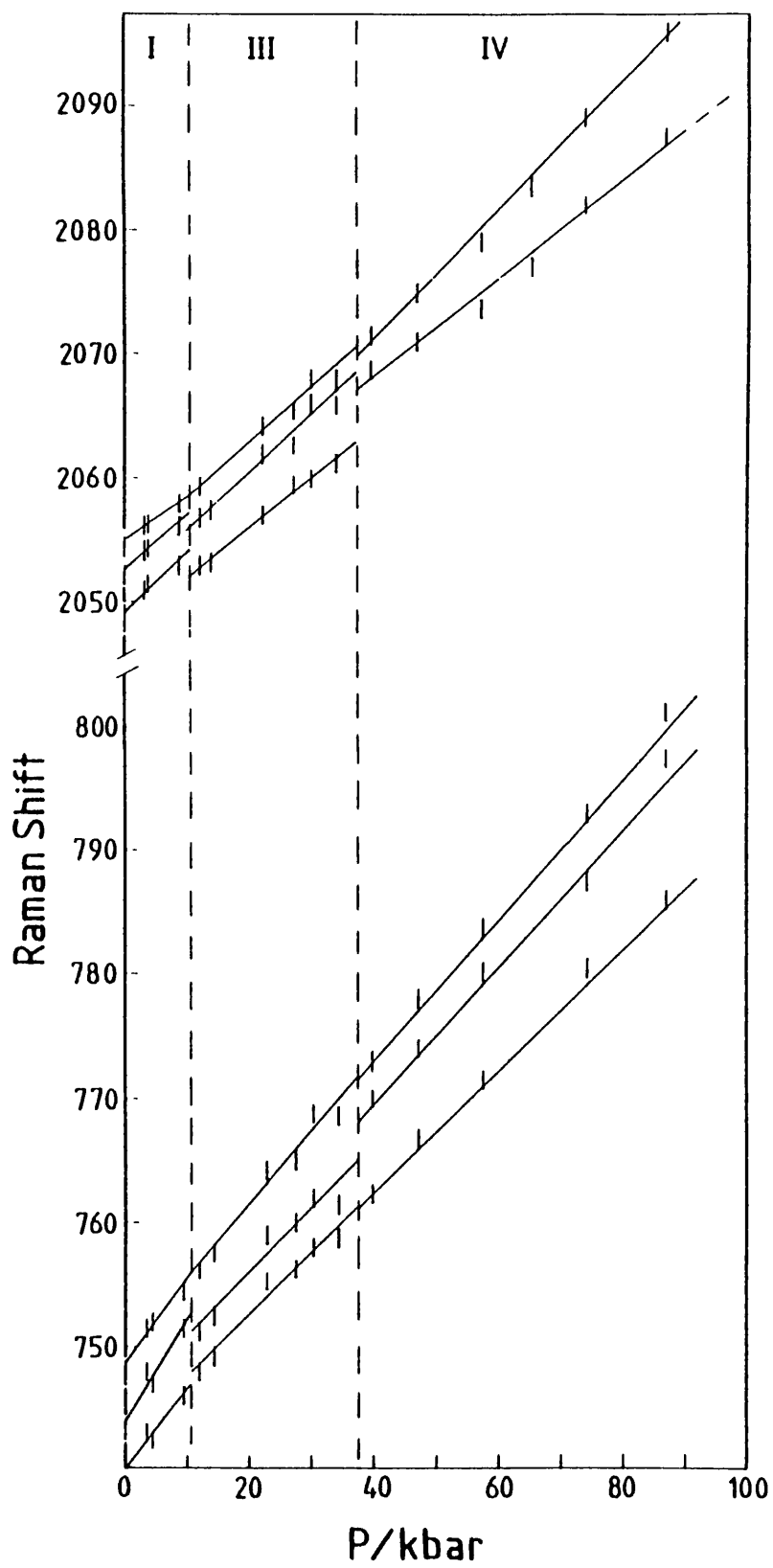


Figure 3.6a)

Plot of frequency ( $\text{cm}^{-1}$ ) against pressure  
for the Raman-active internal modes in  
rubidium thiocyanate.

Figure 3.6b)

Plot of frequency ( $\text{cm}^{-1}$ ) against pressure  
for the Raman-active external modes in  
rubidium thiocyanate.



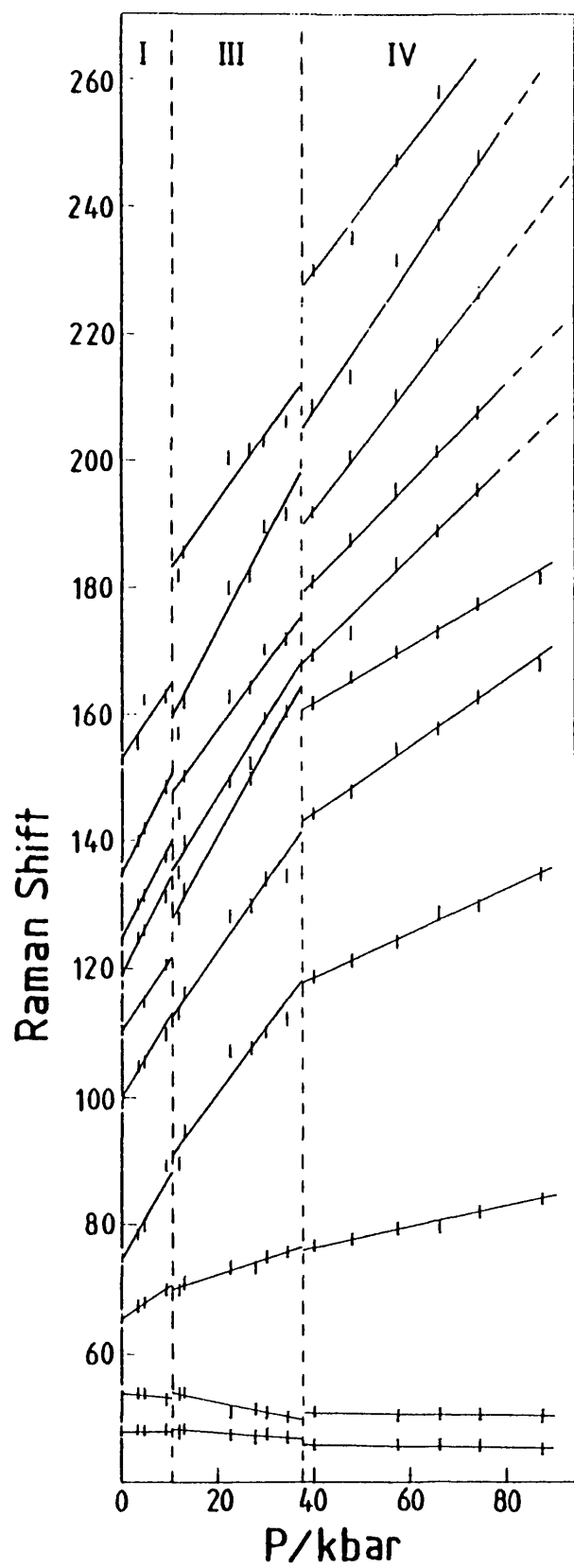
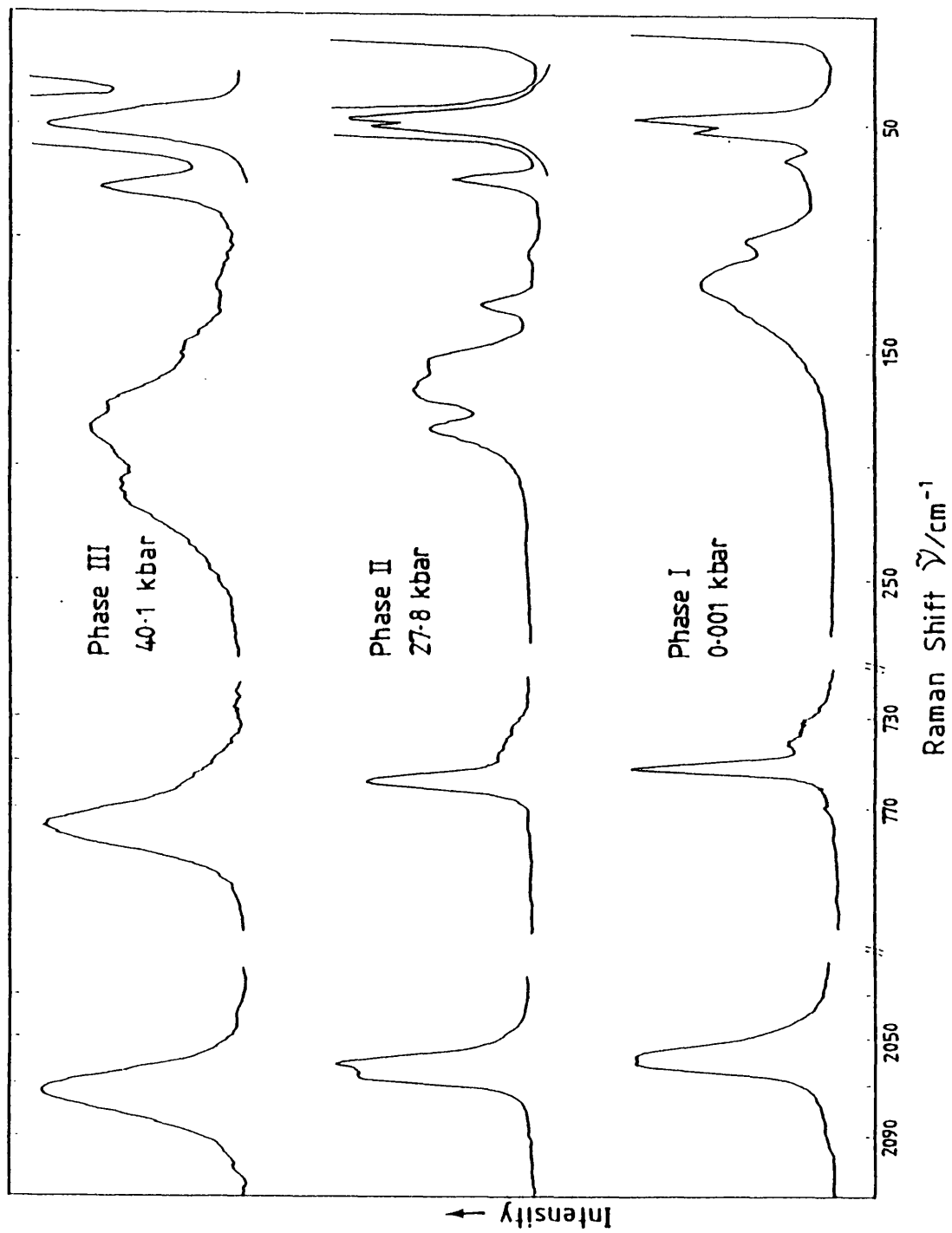


Figure 3.7

The Raman spectra of the external and internal modes for the three high-pressure phases of rubidium thiocyanate.



same throughout the ranges studied. This suggests that the mechanisms involved are probably identical in both compounds and result in the retention of the cell content and of a centre of symmetry. These facts together with the absence of reported volume anomalies in the literature suggest a transition of second order.

### 3.1.5. Discussion KSCN and RbSCN

Since KSCN and RbSCN are isostructural and their phase behaviour similar, they may be treated analogously. If they undergo phase changes of a second order nature, the space group correlation in Table 3.6 a) may be used to explain the spectral features. Hence, the first transition KSCN II-VI is to a monoclinic space group which must be a subgroup of  $D_{2h}^{11}$  ( $C_{2h}^2$  and  $C_{2h}^4$  would serve equally well in place of  $C_{2h}^5$ ). The second transition is likely to involve a change to the triclinic group  $S_2^1$ , which is accessible via all three monoclinic possibilities. The selection rules in all three structures are essentially the same, as they result in the same number of Raman active modes, the only change being formal relabelling.

A reasonable structural explanation for the observed phase transitions can be given by this series of space groups. In the parent group  $D_{2h}^{11}$  the anions lie in the (xy) planes. In  $C_{2h}^5$  (as in  $C_{2h}^4$  and  $C_{2h}^2$ ) these ions are on general positions e. If the  $SCN^-$  ions are tilted about the x-axis and translated along the z-axis, changes in  $D_{2h}^{11}$  will be such as to induce a transformation to a monoclinic space group.

In second order phase transitions there must be a vibrational mode which tends to zero energy continuously as the transition pressure is approached (soft mode),<sup>23</sup> and is considered the driving force in such a transition. However, it must not be totally symmetric in the parent phase, but totally symmetric in the daughter phase. It is possible to ascertain the symmetry of the soft-mode and then possibly the mechanism of the transition via its superimposition on the parent structure. The use of correlation tables reveal that a vibrational mode of symmetry  $B_{2g}$  when we use the standard setting of  $C_{2h}$  ( $C_2(y)$ ) may be the soft mode. It is related to the tilt  $R(x)$  and the translation  $T(z)$ , Table 3.6 b).

A further change, resulting in the loss of the  $C_2$ -axis, may result in a transformation to the triclinic space group  $S_2^1$  which is proposed for the highest pressure phase.

**Table 3.6a).** Space group and crystallographic site correlation for high pressure phases of KSCN and RbSCN.

	II		VI		VII
	$D_{2h}^{11}$		$C_{2h}^5$		$S_2^1$
K	4c	→	4e	→	2i
S*	4d	→	4e	→	2i

(\* All components of  $SCN^-$  on similar sites)

**Table 3.6b).** A correlation table showing the availability of a non totally symmetric (soft) mode in  $D_{2h}$ , with a translation along z, and a rotation about x, that correlates with a totally symmetric mode in  $C_{2h}$ .

Daughter phase	Parent phase	Site symmetry
$C_{2h}$	$D_{2h}$	$Cs(\sigma_{xy})$
	$A_g$	$A'$
$A_g$	$B_{1g}$	$A'$
$B_g$	$B_{2g}$	$A''$
	$B_{3g}$	$A''$ T(z)
	$A_u$	$A''$ Rx
$A_u$	$B_{1u}$	$A''$
$B_u$	$B_{2u}$	$A'$
	$B_{3u}$	$A'$

### 3.2. Caesium Thiocyanate CsSCN

#### 3.2.1. Introduction

Caesium thiocyanate is not isostructural with KSCN II and RbSCN. It exhibits an orthorhombic space group  $D_{2h}^{16}$  (Pnma no. 62) with four molecular units in the primitive unit cell and both cations and anions occupying sites of  $C_s$  symmetry,<sup>16</sup> Fig. 3.8.

A comprehensive single crystal study of the Raman and infrared spectra of CsSCN has been made.<sup>17</sup> Lattice dynamical calculations have been carried out upon CsSCN,<sup>18</sup> with comparisons of experimental and calculated vibrational frequencies being given.

Previously the only known solid-solid transition in CsSCN was that which occurred at 470 K and 1 bar. This was detected from X-ray diffraction results where a volume change of  $1.6 \text{ cm}^3 \text{ mol}^{-1}$  was found.<sup>16</sup> The transition was also revealed by DTA-DSC experiments.<sup>15</sup> There is some disagreement on the nature of the transition. It is unlikely to be similar to those involved in the analogous K, Rb and Tl salts because the transition is thought to be first order due to the size of the volume change and because it also shows some hysteresis on cooling and heating.

In the work submitted here an attempt has been made to identify any transitions which may occur at high pressure and room temperature. CsSCN was studied to 43.5 kbar and a transition was encountered at  $23.5 \pm 1.5$  kbar. It is likely to be second order in type, since there is no optical evidence for the transition.

#### 3.2.2. Experimental

CsSCN was synthesised using a similar method to that employed with RbSCN. The product was recrystallised twice and dried at 373 K for two days.

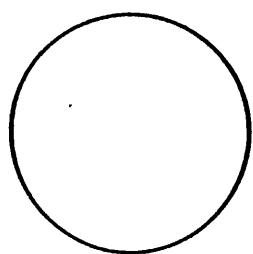
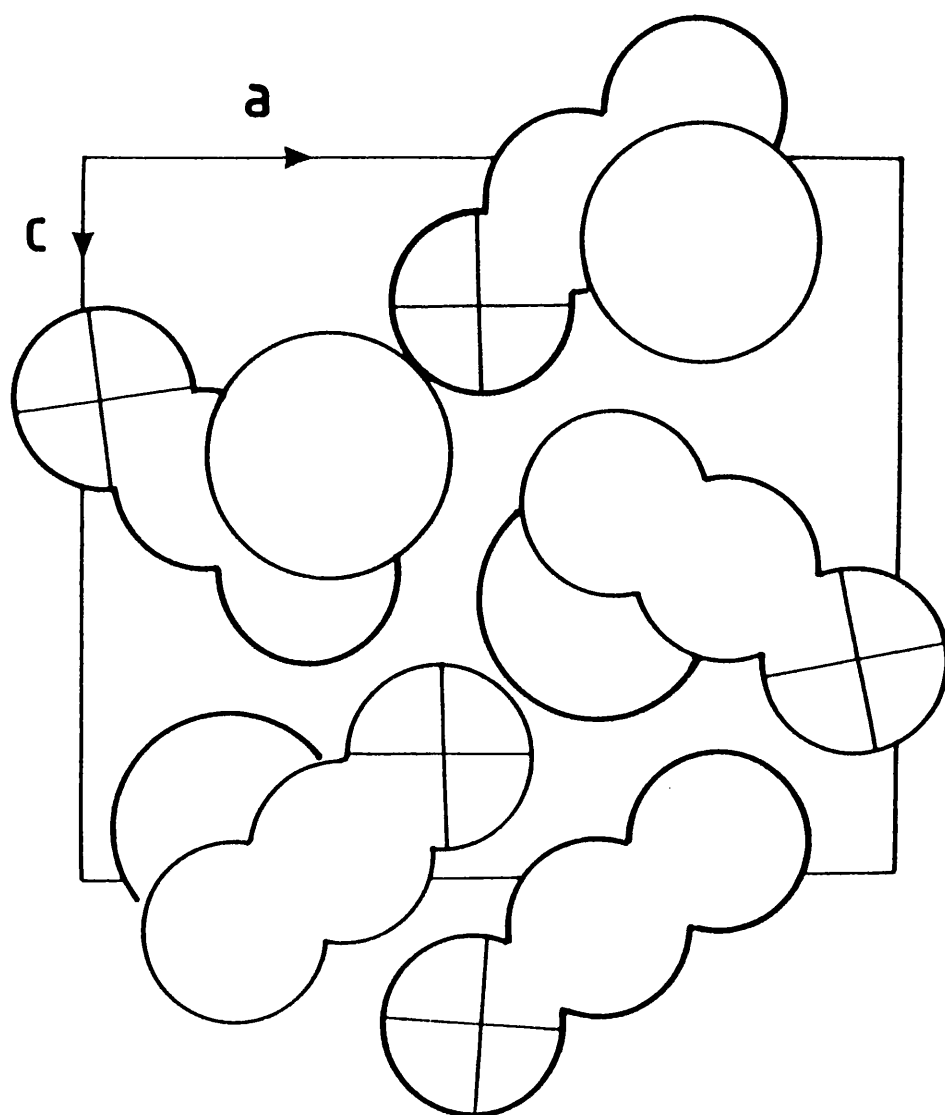
Experimental procedure was again similar to that described for KSCN and RbSCN, differing only in the power of the incident radiation which in this case was approximately 150-250 mW.

CsSCN was followed only to 43.5 kbar, where pressure induced band shifting darkened the samples, resulting in photo decomposition at pressures higher than 45-50 kbar.

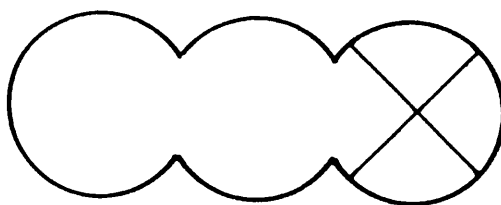


Figure 3.8

The crystal structure of ambient CsSCN. It exhibits an orthorhombic space group  $D_{2h}^{16}$ ,  $Z = 4$ . In each unit cell two  $\text{Cs}^+$  and two  $\text{NCS}^-$  ions lie on planes perpendicular to the b-axis at  $y=0.25$  and  $0.75$ , both cations and anions occupy sites of Cs symmetry. Atom marked with a cross relates to sulphur in the thiocyanate ion. The ions shown by a relatively thick line are at  $y=0.25$  and those shown by a thin line are at  $y=0.75$ .



$\text{Cs}^+$



$\text{NCS}^-$

### 3.2.3. Assignment of vibrational spectra

A factor group analysis requires 24 Raman-active modes, 17 infrared-active modes, and 4 inactive  $A_u$  modes, Table 3.7. There are eight possible Raman-active modes associated with the  $NCS^-$  ion and seven which are infrared-active. All others are associated with vibrations of the lattice. All internal modes predicted in the Raman and infrared spectra by factor group analysis are observed, Table 3.8. Fortunately, most Raman-active external modes in CsSCN are well resolved, but any ambiguity can be resolved using single crystal data<sup>17</sup> and deconvolution routines.

### 3.2.4. High Pressure Results

The observed phase behaviour of CsSCN is confined to one transition at 23 kbar and can be clearly identified by the general reduction in gradient of the vibrational mode/pressure plots, Figs. 3.9a) & b) and Tables 3.9 a) & b). The spectral changes are all subtle and have the characteristics of a second order transition, Fig. 3.10.

### 3.2.5. Discussion CsSCN

Since CsSCN displays no change in the number of Raman active bands at the transition, the cell content and centre of symmetry are likely to be retained. Based on the Landau criteria for second order transitions, sub-groups which enable the above to be maintained are  $C_{2h}^2$  and  $C_{2h}^5$ . A similar mechanism to that envisaged for the transitions, KSCN II/VI and RbSCN I/II is advanced.

## 3.3. Ammonium thiocyanate $NH_4SCN$

### 3.3.1. Introduction

$NH_4SCN$  I, is reported as crystallising in the monoclinic system, space group  $C_{2h}^5$  ( $P2_1/c$  no. 14) with four molecules per unit cell,<sup>19</sup> Fig. 3.11, with cell dimensions  $a = 4.3$ ,  $b = 7.2$ ,  $c = 13.0$  Å and  $\beta = 97^\circ 40'$ .

Raman and infrared spectra have been reported for  $NH_4SCN$  I,<sup>20</sup> and refinements made to the mid-infrared data.<sup>21</sup> The assigned Raman-active internal and external modes of ammonium thiocyanate have been

**Table 3.7.** Factor group analysis of CsSCN crystals.

$D_{2h}^{16}$	N	T'	T	R	$\Gamma_{SCN}$	i.r.	Raman
$A_g$	8		4	1	3		xx, yy, zz
$B_{1g}$	4		2	1	1		xy
$B_{2g}$	8		4	1	3		xz
$B_{3g}$	4		2	1	1		yz
$A_u$	4	2	1	1			
$B_{1u}$	8	1	3	1	3	Tz	
$B_{2u}$	4	1	1	1	1	Ty	
$B_{3u}$	8	1	3	1	3	Tz	

N: Total number of degrees of freedom of motion in a CsSCN crystal.

T': Acoustic modes.

T: Translatory modes.

R: Rotatory modes.

$\Gamma_{SCN}$ : Vibrational modes of S-C-N<sup>-</sup> ion.

**Table 3.8.** Raman-active internal modes of CsSCN.

Symmetry species	(cm <sup>-1</sup> )		
	$\nu_1$	$\nu_2$	$\nu_3$
$A_g$	2041	474	749
$B_{1g}$	----	485	---
$B_{2g}$	2051	474	749
$B_{3g}$	----	487	---

**Table 3.9.(a).** Pressure dependencies of the Raman-active external modes of CsSCN.

	<u>Phase I</u>	<u>Phase III</u>
$\nu_i = 38.0$	0.340	-0.074
40.3	-----	0.123
44.8	0.575	0.301
47.0	-----	-----
55.2	0.565	0.543
73.5	1.000	0.593
94.5	0.987	0.148
124.5	1.957	0.617
142.3	1.867	0.611

**Table 3.9.(b).** Pressure dependencies of the Raman-active internal modes of CsSCN.

	<u>Phase I</u>	<u>Phase III</u>
$\nu_i = 741.8$	0.759	0.523
746.4	0.755	0.530
751.0	0.777	0.484
2043.6	0.570	0.247
2048.8	0.545	0.138
2055.0	0.555	0.079

$\nu_i$  = Initial frequency of the vibrational mode at 0.001 kbar  
in  $\text{cm}^{-1}$

Pressure dependencies  $d\nu/dP$  in  $\text{cm}^{-1}\text{kbar}^{-1}$

Figure 3.9a)

Plot of frequency ( $\text{cm}^{-1}$ ) against pressure  
for the Raman--active external modes of  
CsSCN.

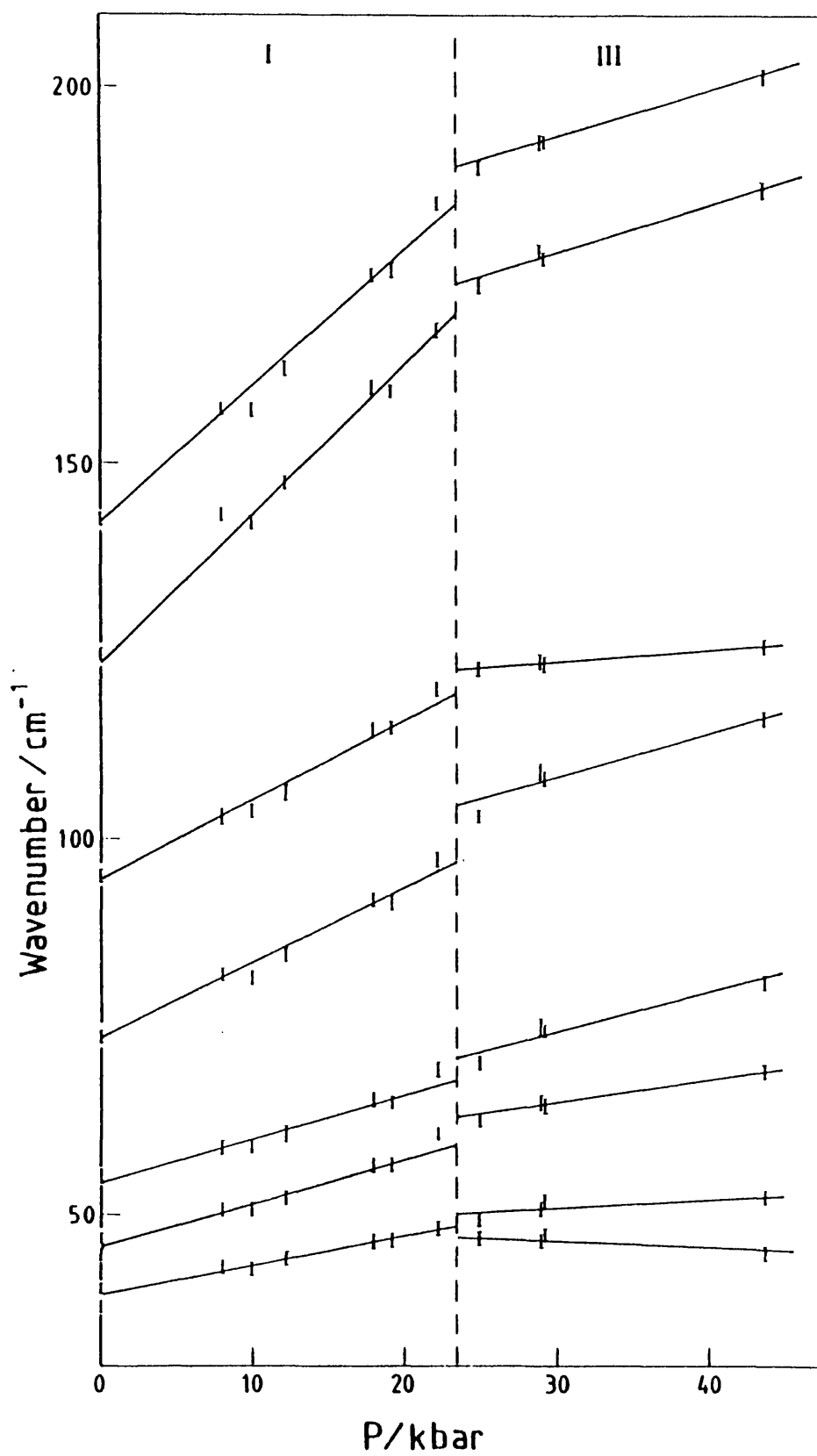


Figure 3.9b)

Plot of frequency ( $\text{cm}^{-1}$ ) against pressure  
for the Raman--active internal modes of  
 $\text{CsSCN}$ .



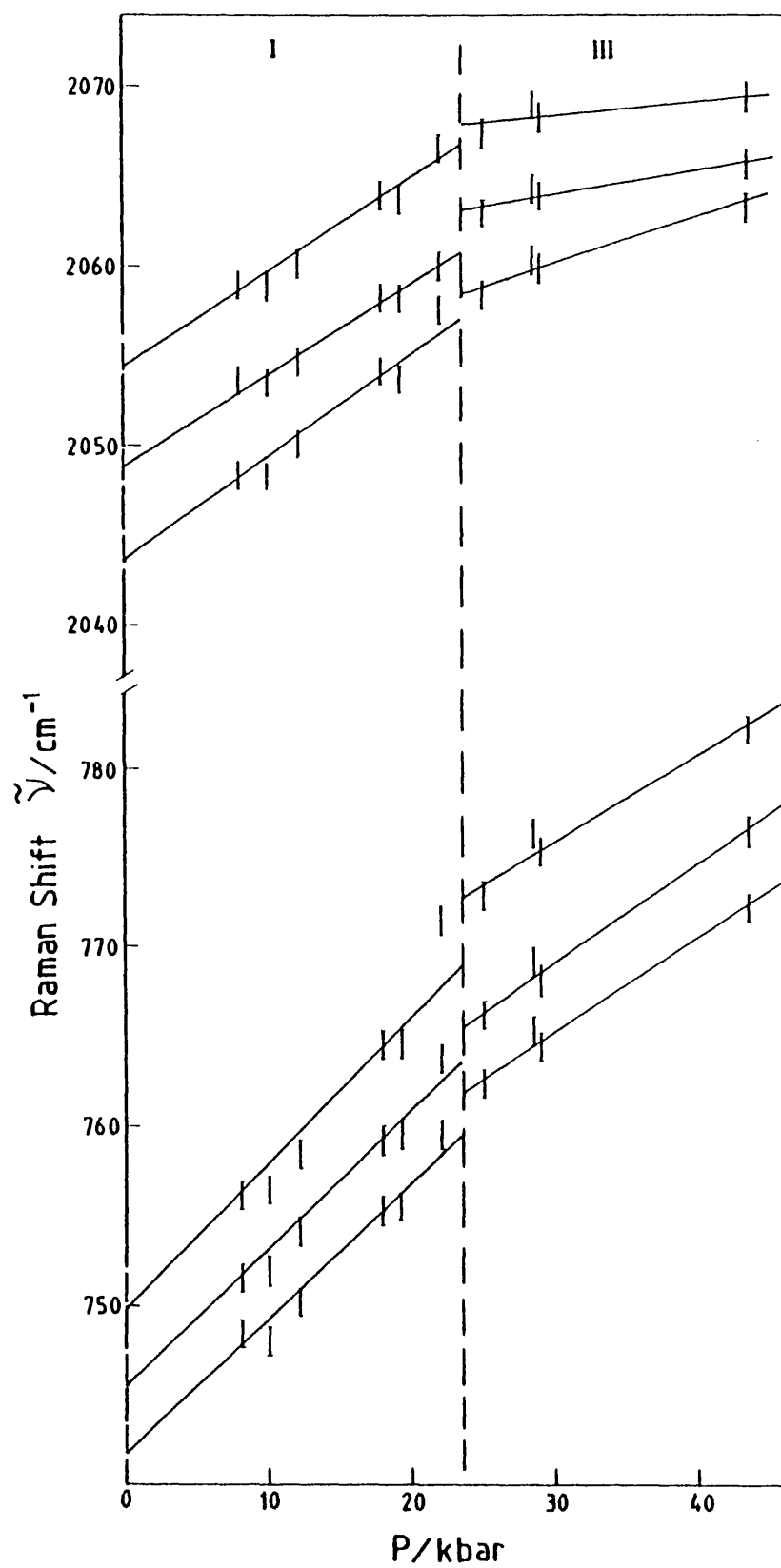


Figure 3.10

The Raman-active spectra for the two room temperature phases of CsSCN, showing both internal and external modes.

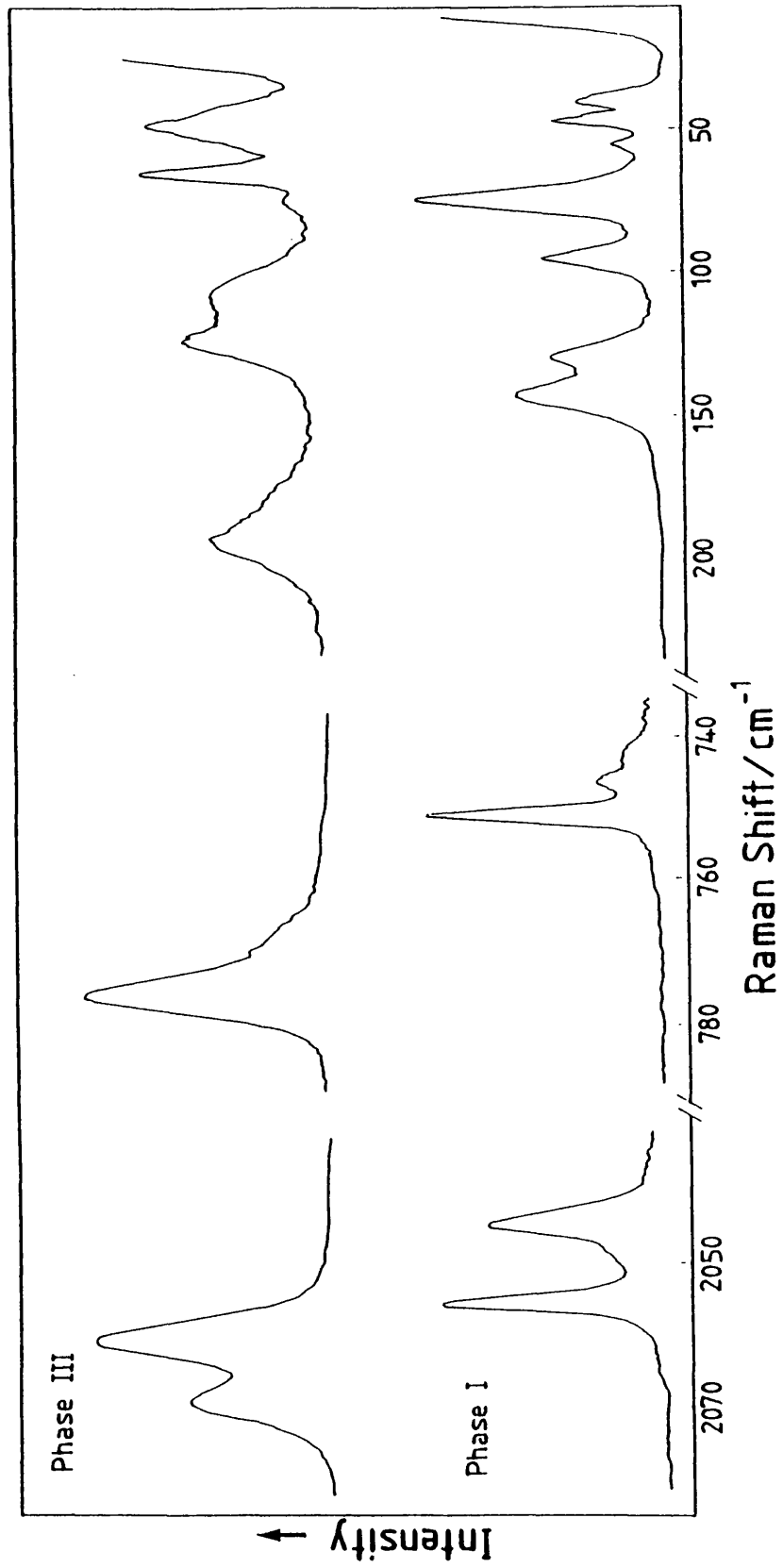
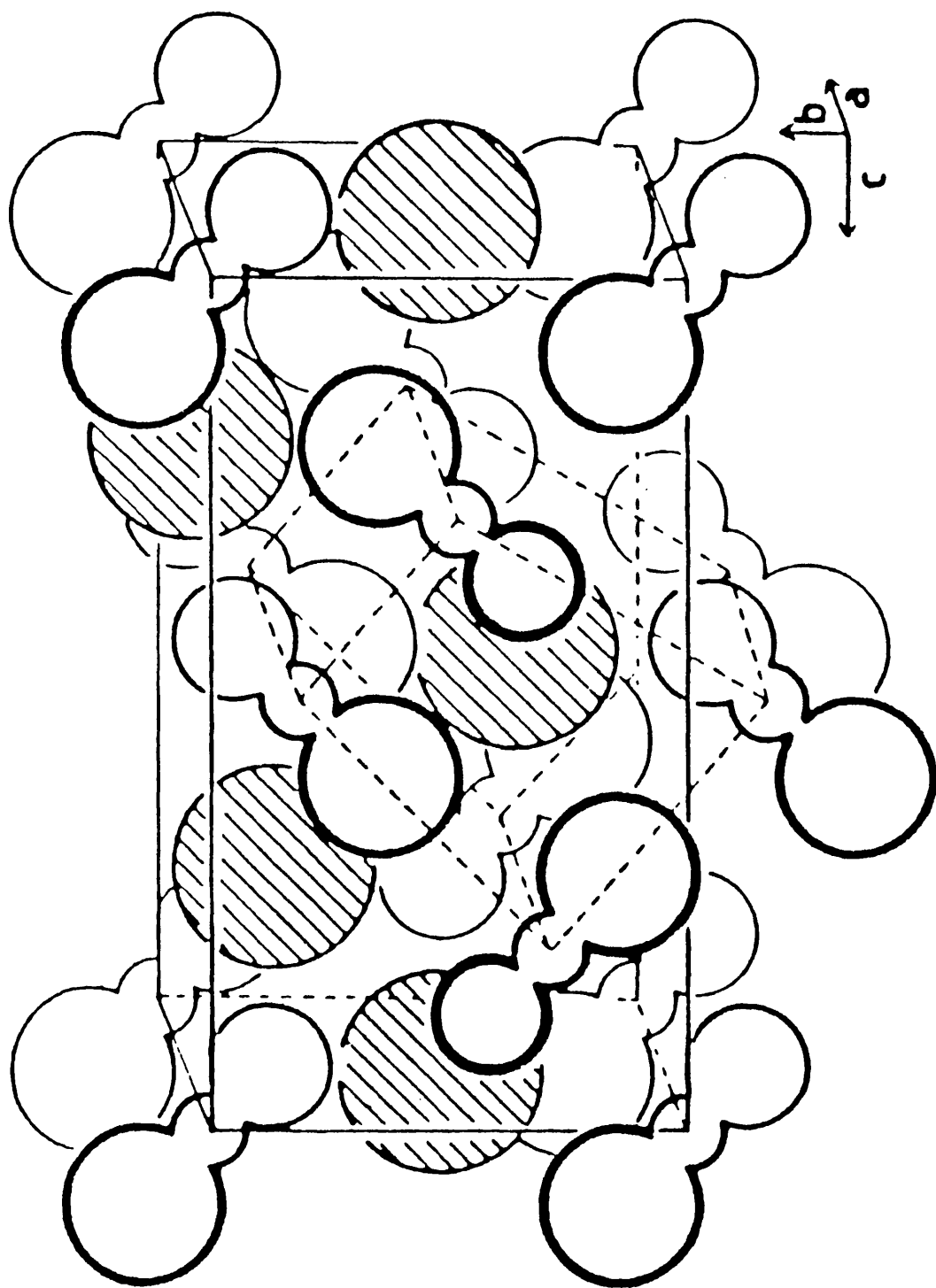
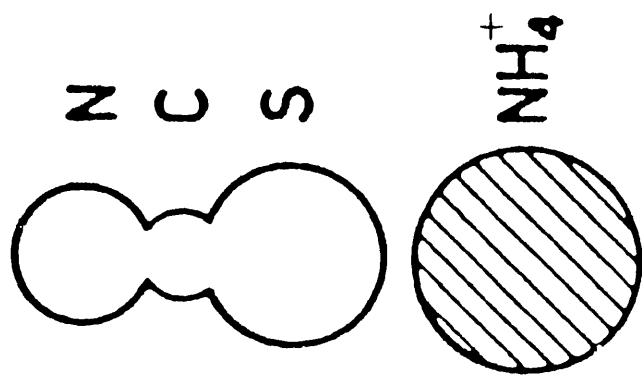


Figure 3.11

The crystal structure of ambient ammonium thiocyanate. It exhibits a monoclinic space group  $C_{2h}^5$ ,  $Z=4$ .



reported, Table 3.10.

The phase behaviour of  $\text{NH}_4\text{SCN}$  has been studied at both variable temperature<sup>10,15,22</sup> and high pressures,<sup>10</sup> and a study on melting and solid-solid transition temperatures with pressure has been attempted.<sup>15</sup> A revised phase diagram has been presented within the range 123 - 473 K and 0 - 50 kbar, Fig. 3.12. There are now five known polymorphic phases of  $\text{NH}_4\text{SCN}$ , of which four are accessible at variable temperature and ambient pressure and one at high pressure.

Phase II has been obtained on cooling to below 207 K,<sup>22</sup> and has been identified by anomalous spectral features in the mid-infrared. Phase I is stable within the range 207 K to  $355.5 \pm 4.0$  K, where the upper limit has been determined by Raman scattering measurements,<sup>21</sup> DTA, DSC<sup>10,15</sup> and X-ray powder diffraction.<sup>15</sup> Phase III, the lower of the two high pressure phases, reverts completely from phase I at atmospheric pressure by 364 K and is stable in the region up to 393 K. The transition III/I has an entropy change of approximately  $2.2 \text{ cal mol}^{-1} \text{ deg}^{-1}$ <sup>15</sup> associated with an increase in disorder.  $\text{NH}_4\text{SCN}$  III exhibits an orthorhombic structure,  $D_{2h}^{11}$  (Pbcm no. 57), as revealed by X-ray powder diffraction, with lattice parameters displayed in Table 3.11. This phase is thought to be isostructural with KSCN II and RbSCN I. This may be the case since phase I of  $\text{NH}_4\text{SCN}$  is a derivative via a monoclinic distortion of the KSCN II structure.

At still higher temperatures, above 393 K,  $\text{NH}_4\text{SCN}$  III transforms to phase IV which is stable between 393 K and 419 K, the melting temperature, displaying a transition entropy of approximately  $0.3 \text{ cal mol}^{-1} \text{ deg}^{-1}$ .<sup>15</sup>

$\text{NH}_4\text{SCN}$  IV is of tetragonal symmetry, which has been elucidated by X-ray powder diffraction Table 3.11, with the III/IV transition boundary showing a slope,  $dT/dP$ , of  $12.6 \pm 1.5 \text{ deg kbar}^{-1}$ .

In a study of the solid-liquid phase boundary, melting was found to occur at 419 K, with a melting entropy of  $5.1 \text{ cal mol}^{-1} \text{ deg}^{-1}$  recorded, with a boundary slope of approximately  $18.5 \text{ deg kbar}^{-1}$ .<sup>15</sup>

Previous work on the high pressure phases of  $\text{NH}_4\text{SCN}$  is scarce. Bridgman,<sup>10</sup> detected a volume change at approximately 2 kbar, in a study up to 12 kbar. This can be associated with the large changes in the Raman spectra presented in this work. It was initially suggested that this was a completely new modification. However, on determining the transition at other temperatures, it appeared that it was not a new form, but that the transition line runs from high to low temperatures with increase in pressure. We can say, therefore, that this high

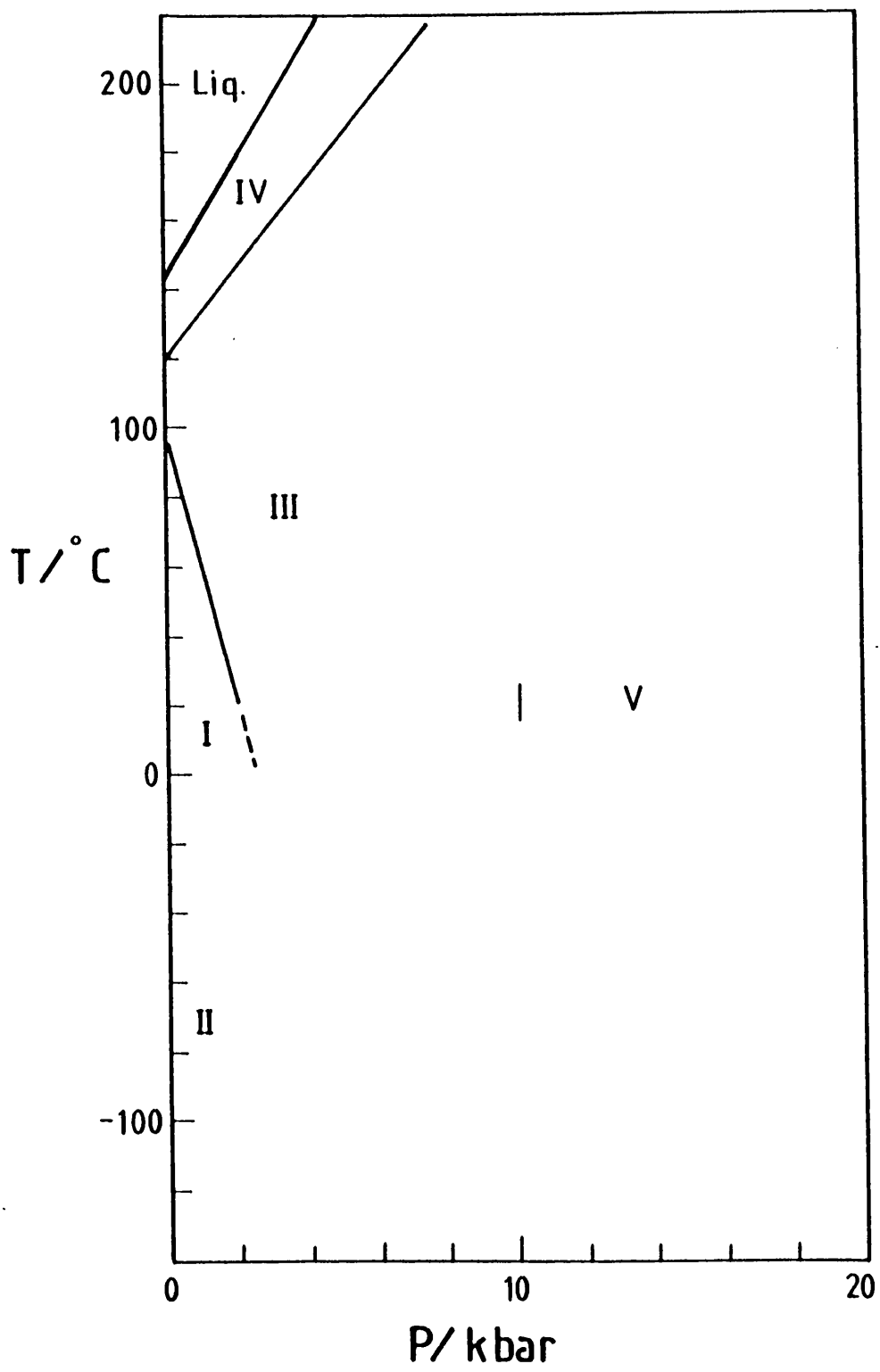
**Table 3.10.** The Raman--active internal and external modes of ambient ammonium thiocyanate.

$\nu$ (cm <sup>-1</sup> )	Symmetry Species	Type
45.2	B <sub>g</sub>	R <sub>SCN</sub>
53.0	B <sub>g</sub>	R <sub>SCN</sub>
64.5	--	--
81.0	--	--
90.0	A <sub>g</sub>	R <sub>SCN</sub>
100.0	A <sub>g</sub>	R <sub>SCN</sub>
148.0	B <sub>g</sub>	--
168.5	B <sub>g</sub>	--
187.5	A <sub>g</sub>	--
465.0	A <sub>g</sub>	$\nu_2$ $\delta$ (SCN)
479.0	B <sub>g</sub>	
746.0	A <sub>g</sub> +B <sub>g</sub>	$\nu_1$ $\nu$ (SC)
752.0		
945.0	--	2 $\nu_2$
2063.0	A <sub>g</sub>	$\nu_3$ $\nu$ (CN)
2074.0	B <sub>g</sub>	

Figure 3.12

Phase diagram of ammonium thiocyanate,  
 $\text{NH}_4\text{SCN}$ , displaying the new high pressure  
phase, V.





pressure modification is in fact  $\text{NH}_4\text{SCN}$  III with the space group  $D_{2h}^{11}$  (Pbcn). Transition III/V occurs at  $10 \pm 1$  kbar and has not been detected previously. This indicates either a very small or no volume change. This along with the small to moderate spectral changes observed suggests a transition of second order. Finally, ammonium thiocyanate was further studied to a pressure of 62.0 kbar where no additional change in the Raman spectra was recorded.

### 3.3.2. Experimental

Analar grade ammonium thiocyanate was used after recrystallisation and two days drying at 373 K. Other experimental procedures were similar to those described for potassium thiocyanate KSCN.

### 3.3.3. Assignment of Vibrational Spectra

Factor group analysis reveals 48 possible Raman-active and 45 infrared-active modes. From this analysis 22 Raman active external modes should be observable; in fact we detect only 10. However, a site group treatment reveals 11 possible Raman-active external modes, and this treatment seems appropriate for our work. The same treatment can be used for the ammonium ion fundamental modes where 10 bands are found, and a factor group analysis reveals 18 bands, but a site group analysis requires 9 bands. However, in the case of the  $\text{SCN}^-$  ion factor group splitting is necessary to accommodate the observed CN and SC doublets, reflecting a larger degree of coupling amongst the thiocyanate ions. Since  $\nu_2$  in the thiocyanate ion is required to be a quartet, we may assume that the observed doublet is in fact a pair of unresolved  $A_g + B_g$  doublets, Table 3.10.

### 3.3.4. High Pressure Results

Ammonium thiocyanate displays two phase transitions at pressures up to 62.0 kbar and 293 K, one at 2 kbar and one at 10 kbar. The first transition I/III is easily detected with large spectral changes occurring in all regions, Fig. 3.13a),b),c)& d), 3.14 and Table 3.12. The greatest change is observed in the  $\nu_{\text{CN}}$  region where the observed doublet is reduced to a singlet some  $22 \text{ cm}^{-1}$  lower than the doublet average.

**Table 3.11.** Lattice parameters of ammonium thiocyanate at high temperatures.

	a	b	c	$\beta$ (Deg)
<u>Monoclinic</u>				
T = 22.0	4.247	7.146	13.022	97.8
84.0	4.285	7.180	12.973	98.1
<u>Orthorhombic</u>				
88.0	6.874	6.903	7.878	
102.0	6.878	6.905	7.912	
117.0	6.898	6.912	7.954	
<u>Tetragonal</u>				
140.0	6.961		8.000	

**Table 3.12.** Pressure dependences of the Raman—active internal and external modes of  $\text{NH}_4\text{SCN}$ .

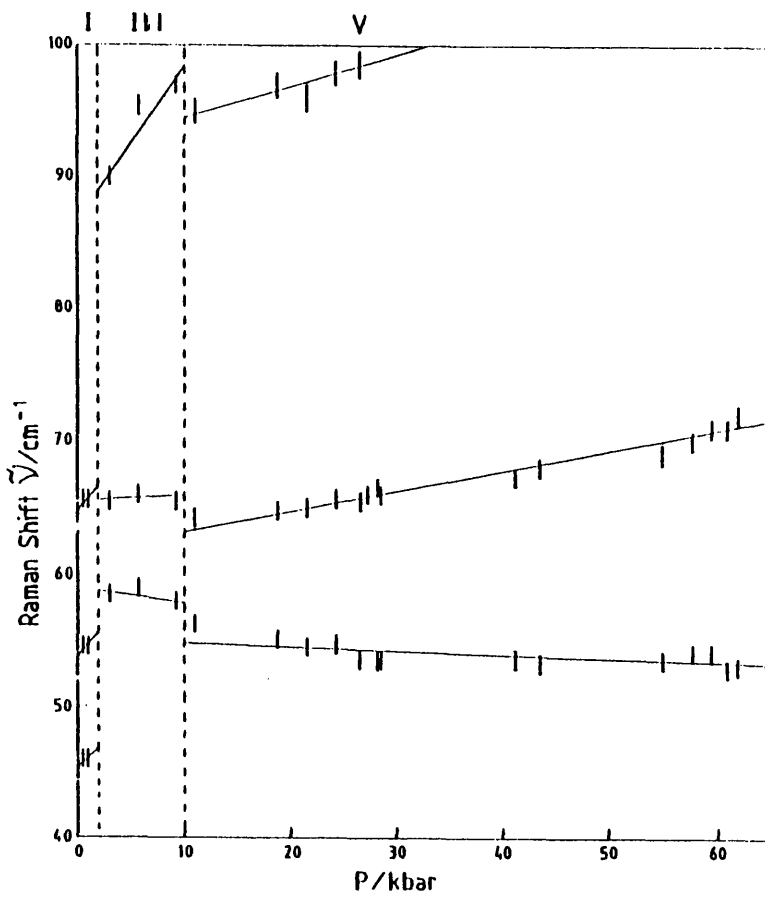
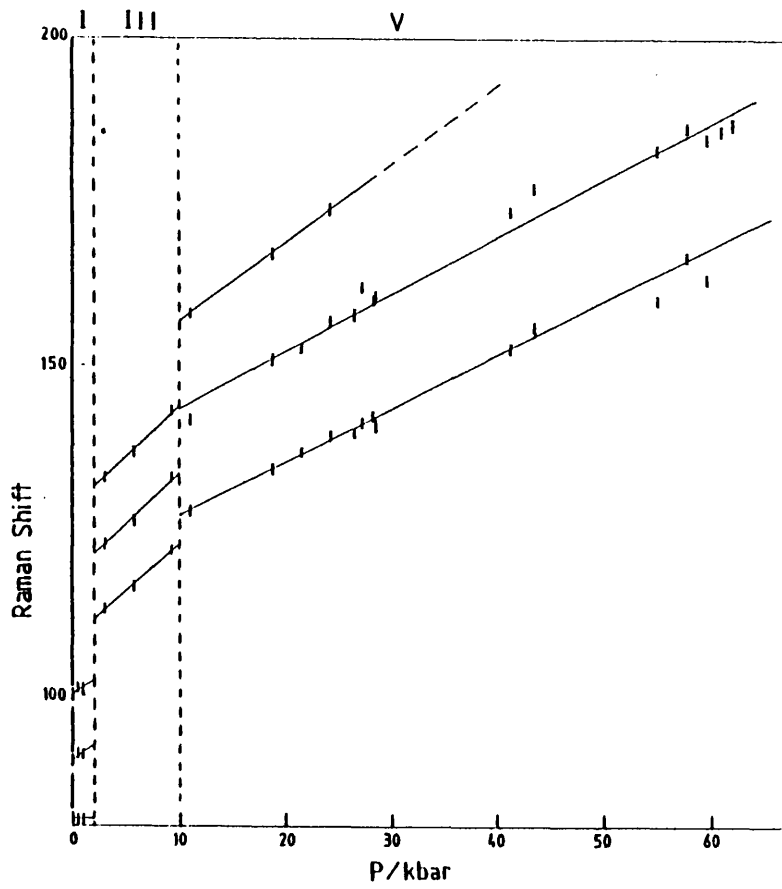
	<u>External modes</u>		<u>Internal modes</u>	
	$\nu_i$	$d\nu_i/dP$	$\nu_i$	$d\nu_i/dP$
<u>Phase I</u>	45.2	0.85	745.5	-0.15
	53.0	0.93	752.0	-0.12
	64.7	0.92	2063.0	-0.17
	81.0	0.05	2076.0	-0.18
	90.2	1.10		
	100.1	0.95		
	147.5	2.50		
	168.5	2.41		
	187.5	2.75		
<u>Phase I'</u>	58.7	-0.11	747.5	0.73
	65.5	0.04	752.2	0.82
	88.8	1.2	2044.2	0.35
	111.6	1.45		
	120.2	1.46		
	131.6	1.45		
	151.2	2.63		
	169.3	2.58		
	182.6	2.58		
<u>Phase V</u>	54.7	-0.03	752.3	0.48
	63.2	0.15	759.0	0.52
	94.4	0.24	2048.2	0.31
	127.2	0.82		
	143.5	0.82		
	156.8	1.20		
	180.0	1.65		
	198.5	1.60		
	210.0	1.61		

$\nu_i$  = Initial frequency of the vibrational mode at the phase boundary.

Pressure dependencies  $d\nu_i/dP$  in  $\text{cm}^{-1}\text{kbar}^{-1}$ .

Figures 3.13a) & b)

Plots of frequency versus pressure for  
external modes of  $\text{NH}_4\text{SCN}$ .



Figures 3.13c) & d)

Plot of frequency versus pressure for  
external modes c) and internal modes d)  
of  $\text{NH}_4\text{SCN}$ .

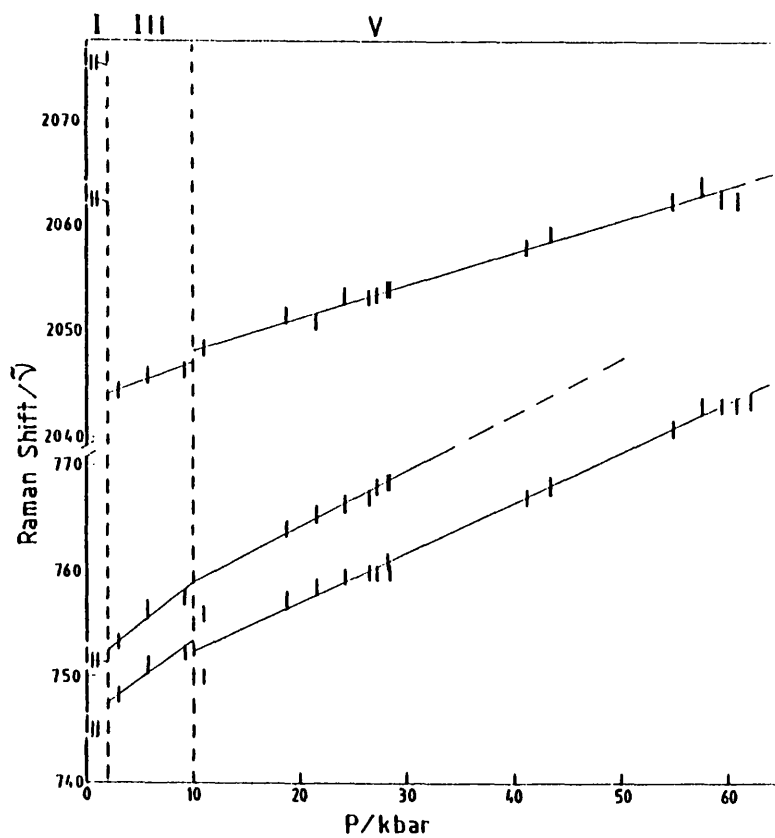
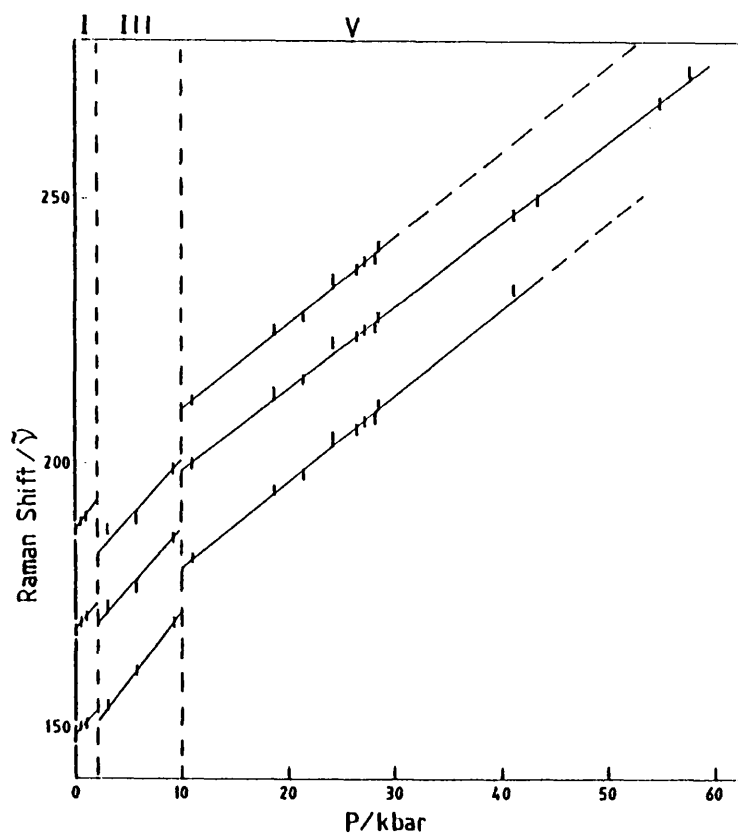
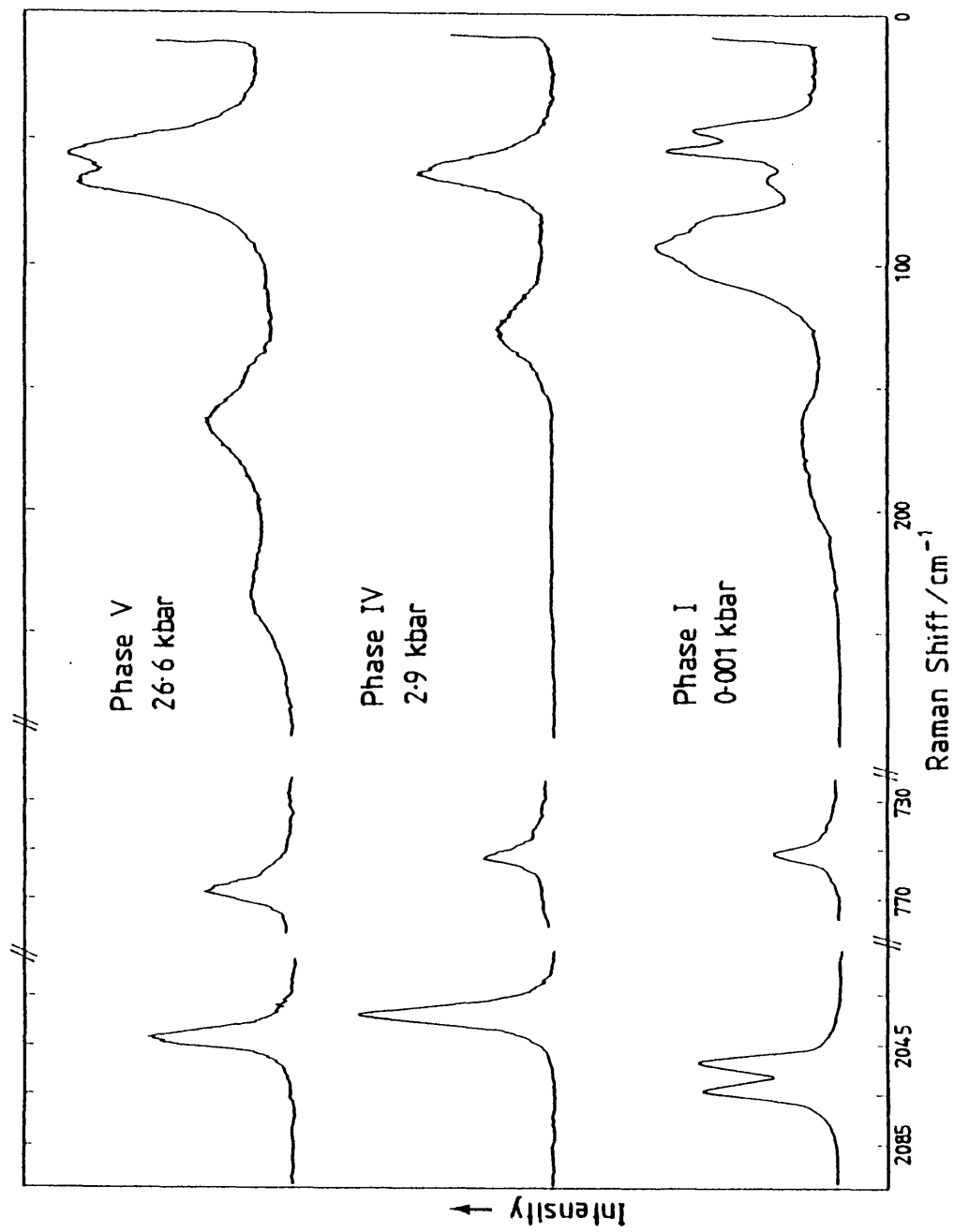




Figure 3.14

The Raman-active internal and external  
modes of  $\text{NH}_4\text{SCN}$  at high pressures



Comparable changes occur in all Raman-active bands, with slightly less dramatic changes occurring in the mid-infrared.

The second transition occurring at 10 kbar, although not as obvious, displays subtle changes in all regions. The combined evidence for the transition leaves little doubt as to its existence.

### 3.3.5. Discussion $\text{NH}_4\text{SCN}$

Since the I/III transition is accompanied by a large volume change it is almost certainly of a first order type. Although phase I is a sub-group of phase III it does not follow the Landau criteria usually associated with second order transformations where continuous changes across phase transition boundaries are expected. We are probably observing a mere coincidence and in fact there must be intermediate structure type(s) involved, following a Boyle analysis. In a Boyle analysis, the relationship between the crystal structure of two phases involved in a first order phase change may not be immediately apparent, and any similarity to a second order sub-group/super-group relationship is likely to be a coincidence. However, when using this analysis it can be shown that several stages of ascent and/or descent in symmetry may reveal a relationship. The reproducibility of such transitions argues in favour of a certain defined pathway which the atoms follow. To produce an absolutely random arrangement of atoms at the transition is probably more energetically difficult than to allow the use of more symmetrical pathways.

The second transition near 10 kbar is almost certainly second order in type. There appears to be a retention of cell content and centre of symmetry at the III/V boundary, indicated by the retention of the number of Raman active bands across the boundary. This in turn suggests that  $\text{NH}_4\text{SCN}$  V must be one of the three possible monoclinic  $C_{2h}^n$  groups where  $n = 2, 4, \& 5$ . However, it must be noted that phases I and V are likely to be totally different structures, and this may be proven by comparing the Raman spectra of each, which are evidently quite different.

## References

1. Klug, H.P. (1933), *Z. Kristallogr.*, **85**, 214.
2. Bussen, W., Gunther, P. and Tubin, R. (1934), *Z. Phys. Chem.*, **24B**, 1.
3. Akers, C., Peterson, S.W. and Willett, R.D. (1968), *Acta Cryst.*, **B24**, 1125.
4. Jones, L.H. (1956), *J. Chem. Phys.*, **25**, 1069.
5. Jones, L.H. (1958), *J. Chem. Phys.*, **28**, 1234.
6. Tramer, A. (1959), *Compt. Rend.*, **249**, 2531.
7. Iqbal, Z., Sarma, L.H. and Moller, K.D. (1972), *J. Chem. Phys.*, **57**, 4728.
8. Kettle, F.A., Ti, S.S. and Ra, Q. (1976), *Spectrochim. Acta*, **32A**, 1603.
9. Dao, N.Q. and Wilkinson, G.R. (1973), *J. Chem. Phys.*, **59**, 1319.
10. Bridgman, P.W. (1915), *Proc. Am. Acad. Arts Sci.*, **51**, 55.
11. Shinoda, T., Suga, H. and Seki, S. (1960), *Bull. Chem. Soc. Japan*, **33**, 1314.
12. Shinoda, T., Suga, H. and Seki, S. (1963), *Bull. Chem. Soc. Japan*, **36**, 1025.
13. Pistorius, C.W.F.T., Clark, J.B. and Rapoport, E. (1968), *J. Chem. Phys.*, **48**, 5123.
14. Yasusada, Y. and Watanabe, T. (1963), *Bull. Chem. Soc. Japan*, **36**, 1032.

15. Klement, W. and Pistorius, C.W.F.T. (1976), *Bull. Chem. Soc. Japan*, **49**, 2148.
16. Manolatos, S., Tillinger, M. and Post, B. (1973), *J. Solid State Chem.*, **7**, 31.
17. Ti, S.S., Kettle, F.A. and Ra, Q. (1977), *Spectrochim. Acta*, **33**, 1603.
18. Ra, Q., Ti, S.S. and Kettle, F.A. (1978), *J. Chem. Phys.*, **68**, 2638.
19. Zdanov, G.S. (1949), *Zurnal Fiz. Khimii*, **23**, 1495-1501.
20. Tramer, A. (1959), *Compt. Rend.*, **249**, 2755.
21. Oden, L.L. and Decius J.C. (1964), *Spectrochim. Acta*, **20(4)**, 667-74.
22. Tewari, G.D., Raghuvanshi, G.S., Khandelwal, D.P. and Bist H.D. (1984), *Chem. Phys. Lett.*, **103**, 328.
23. Scott, J.F. (1974), *Rev. Mod. Phys.*, **46(1)**, 83-128.
24. Boyle, L.L. Walker, J.R. and Wanjie, A.C., (1980), *Faraday Discussion*, **69**, 115-119.

## CHAPTER FOUR

A RAMAN SCATTERING STUDY OF UNIVALENT NITRITES  $\text{MNO}_2$  (M = Na & K)

AT HIGH PRESSURES

## CHAPTER FOUR

### A RAMAN SCATTERING STUDY OF UNIVALENT NITRITES $\text{MNO}_2$ ( $\text{M} = \text{Na} \text{ \& \; K}$ ) AT HIGH PRESSURES

#### Sodium Nitrite $\text{NaNO}_2$

##### 4.1. Introduction

The determination of the  $\text{NaNO}_2$  structure was first attempted by Ziegler 1931, and the orthorhombic space group  $\text{C}_{2v}^{20}$  was suggested.<sup>1</sup> This was subsequently revised by Carpenter 1952,<sup>2</sup> and further refinements were made to the structure by Truter 1953<sup>3</sup> and Carpenter 1955.<sup>4</sup> All these attempts at the structural determination of  $\text{NaNO}_2$  again yielded a space group of  $\text{C}_{2v}^{20}$  (Imm2 no. 44) with a unimolecular primitive cell. The structure was found to consist of a body-centred array of  $\text{Na}^+$  and  $\text{NO}_2^-$  ions, with dimensions  $1.23(6) \pm 3(5)$  Å for the N-O bond and  $115.4^\circ \pm 1.73^\circ$  for the angle O-N-O, Fig. 4.1.<sup>4</sup>

The original work on the assignment of the vibrational spectrum of  $\text{NaNO}_2$  did not prove conclusive.<sup>5-7</sup> An extensive single crystal study by Asawa and Barnoski 1970,<sup>8</sup> has been used as our reference. The Raman spectrum although potentially simple, is greatly complicated by the existence of l.o.-t.o. splitting, and a strong dependence of some phonon frequencies upon propagation direction. Further mid-infrared spectra of this compound have been reported by Tsuboi, Terada and Kajiura, 1968<sup>9</sup> and 1969.<sup>10</sup>

Studies of this compound at conditions other than standard temperature and pressure are plentiful. The vast majority of them concentrate on the structural variations with temperature and the ferroelectric - paraelectric incommensurate relationship at  $163\text{--}164.5^\circ\text{C}$  in particular.<sup>11-14</sup> There has been an attempt at rationalising the incommensurate phase with a group theoretical approach by MacConnell 1983.<sup>16</sup> A study of the high-temperature paraelectric phase I revealed the space group  $\text{D}_{2h}^{23}$ .<sup>12</sup> At 178 K  $\text{NaNO}_2$  III undergoes a second-order phase transition to  $\text{NaNO}_2$  IV, which occurs without discontinuous change in both the dielectric constant, volume thermal expansion and without

Figure 4.1

The crystal structure of sodium nitrite  
at ambient temperature and pressure.

Orthorhombic space group,  $C_{2v}^{20}$  (Imm2),  
with a unimolecular primitive cell.

Unit cell dimensions:  $a=3.55 \text{ \AA}$

$b=5.38 \text{ \AA}$

$c=5.56 \text{ \AA}$

Atomic positions: Na in 2(a) with  $z=0.597$

N in 2(a) with  $z=0.118$

O in 4(d) with  $z=0$  and  
 $y=0.194$

Interatomic distances and angles:

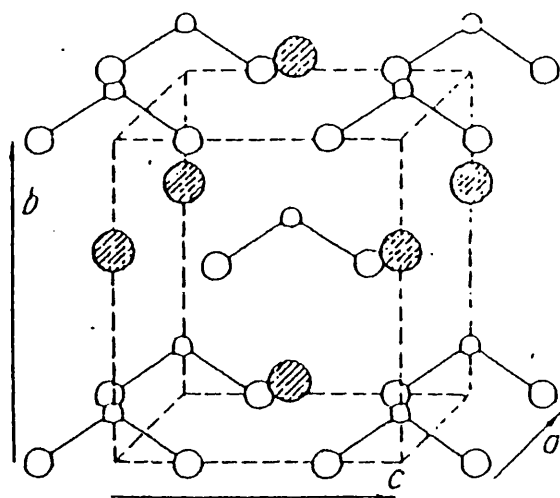
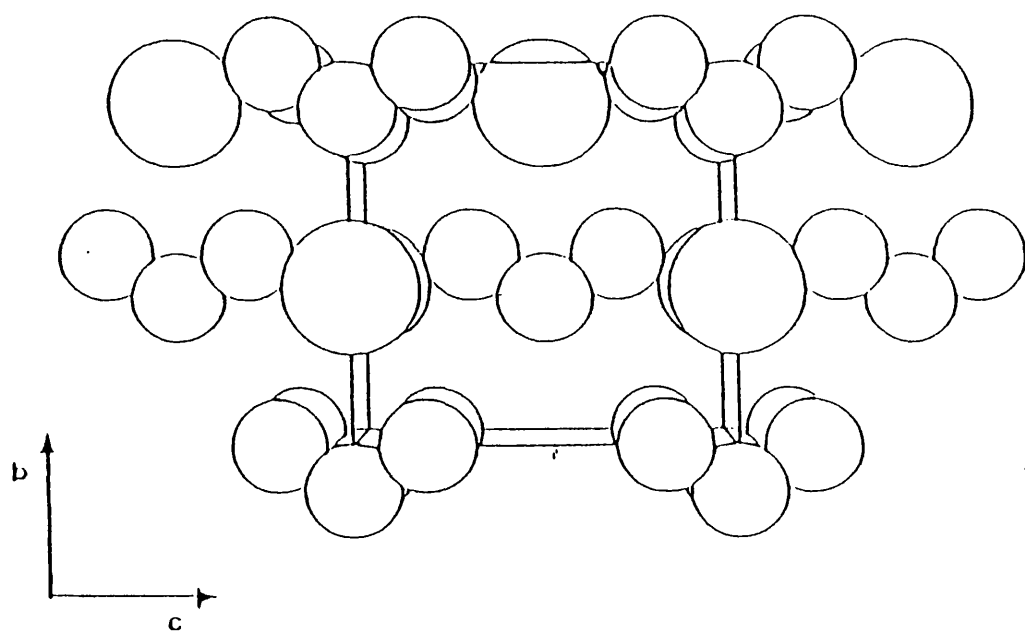
Na-O = 2.47, Na-O = 2.52, Na-N = 2.61.

N-O = 3.22, O-O = 3.35 (exterior to the  
 $\text{NO}_2$  group).

The dimensions of the  $\text{NO}_2$  ion are N-O =  
1.233, angle O-N-O = 115.7 Deg.

(All distances are in  $\text{\AA}$ )





thermal hysteresis,<sup>17</sup> implying a second order mechanism. Other anomalies have been recorded at 100, 178 and 215 °C, and atmospheric pressure, with changes in thermal expansion, dielectric constants and piezoelectric properties. These are thought to be related to the anisotropic vibrorotary states of the NO<sub>2</sub><sup>-</sup> ions.<sup>17</sup>

Besides the variable temperature transitions, Bridgman,<sup>18</sup> found a pressure-induced transition from volume compression experiments. Rapoport 1966,<sup>19</sup> studied NaNO<sub>2</sub> to determine its phase diagram between 0–40 kbars and room temperature–500°C, Fig. 4.2. He showed five modifications of sodium nitrite, of which two were pressure dependent, phase IV and V. Phase IV was found to be identical to the high pressure phase Bridgman had first described and a fifth was found to exist just below the melting point above 10 kbar.

The III/IV transition has been further investigated using vibrational spectroscopy by Adams and Sharma 1981,<sup>20</sup> in a study up to 40 kbar; this confirmed both Bridgman and Rapoport. Adams and Sharma have suggested a number of possible space groups for NaNO<sub>2</sub> IV based on the assumption that it must be a zellengleich sub-group of Imm2 due to the second-order nature of the transition. This analysis yields P1, P2, B2, Pm or Bm as the possible space groups.

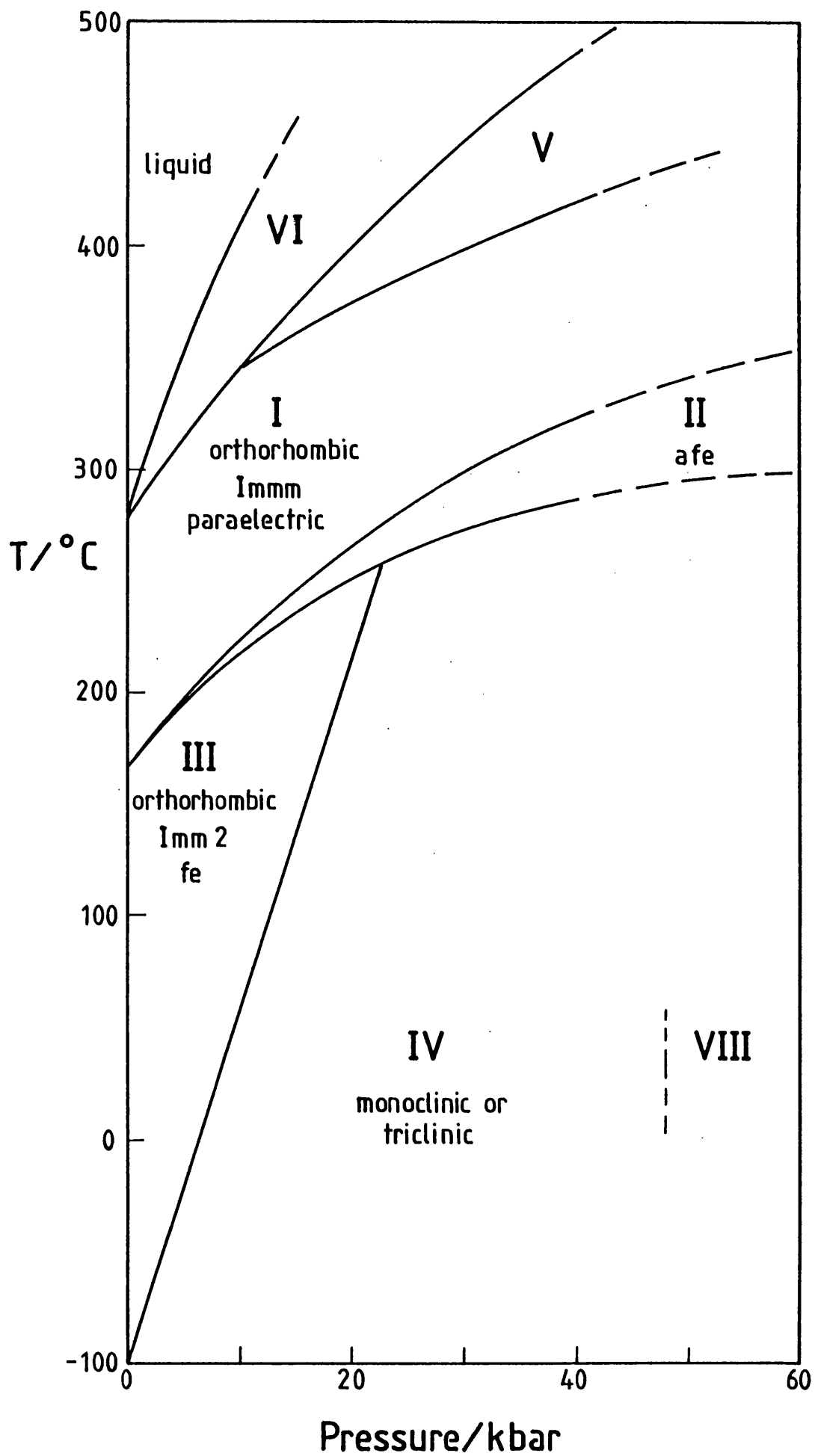
This present study investigates sodium nitrite at room temperature up to 100 kbar, and subsequently confirms the transition III/IV at 8.5 kbar, also it has revealed a new transition at 48.0 kbar which appears to be of a first-order nature and is thought to involve a cell doubling.

#### 4.2. Experimental

Analar grade NaNO<sub>2</sub> was used in a diamond anvil high pressure cell. Pressures were estimated by the ruby R-line method. The samples were contained within stainless steel or inconel gaskets with a hole diameter 0.4 mm and 0.2 mm thick (initial dimensions). Spectra were excited with 488.0 nm and 514.5 nm Ar<sup>+</sup> radiation of approximately 400 mW power. Any modes arising from the  $\nu_1$ ,  $\nu(\text{NO}_2)_s$ , could not be followed at any time, as they were obscured by the intense first-order phonon line of diamond at 1332 cm<sup>-1</sup>.

**Figure 4.2**

Phase diagram of Sodium Nitrite,  $\text{NaNO}_2$ .



#### 4.3. Assignment of Raman spectrum

Sodium nitrite displays a unimolecular unit cell in which the anion is a bent triatomic with angle O-N-O,  $115.4^{\circ} \pm 1.73$ . The nitrogen atoms occupy sites of  $C_{2v}$  symmetry. A standard factor group analysis, Table 4.1, reveals that there are nine Raman active vibrational modes,  $3A_1 + A_2 + 2B_1 + 3B_2$  and eight infrared active modes  $3A_1 + 2B_1 + 3B_2$ .

There are three internal modes representing the vibrations of the nitrite ion and the rest in both cases are due to lattice vibrations of the sodium ion against the nitrite ion.

The internal modes are represented by the strong  $\nu_1$ ,  $\nu(\text{NO}_2)_s$  which is located at  $1330 \text{ cm}^{-1}$ , the medium strength  $\nu_2$ ,  $\delta(\text{NO}_2)$  at  $830 \text{ cm}^{-1}$  and the weak broad  $\nu_3$ ,  $\nu(\text{NO}_2)_{as}$  at  $1230 \text{ cm}^{-1}$ .<sup>8</sup> Under normal conditions the lattice mode region was difficult to resolve although an attempt has been made by the use of a deconvolution routine, Fig. 4.3.

#### 4.4. High pressure results

Representative Raman spectra recorded at various pressures are shown in Figs. 4.3 and 4.4, with mode shifts versus pressure given in Figs. 4.5 & 4.6.

The clearest indication of the III/IV transition, which occurs at 8.5 kbar is the behaviour of the two lattice modes, initially at  $188 \text{ cm}^{-1}$  ( $B_1$ ) and  $224 \text{ cm}^{-1}$  ( $B_2$ ). They converge, and then appear to merge at the phase boundary, yielding a broad band with two overlapping components Fig. 4.3. Such behaviour confirms that these two modes are of different symmetry species,<sup>8</sup> they have not been followed in earlier studies.<sup>20</sup> The pair which were at  $155 \text{ cm}^{-1}$  ( $B_1$ ) and  $163 \text{ cm}^{-1}$  ( $B_2$ ) were also not followed in detail in the initial study. The lattice mode initially at  $121 \text{ cm}^{-1}$  ( $A_1$ ) has been observed to exhibit identical behaviour to that reported by Adams and Sharma.<sup>20</sup>

The internal mode  $\nu_3$ ,  $\nu(\text{NO}_2)_{as}$ , also drops by  $2.3 \text{ cm}^{-1}$  at the III/IV transition, but  $\nu_2$ ,  $\delta(\text{NO}_2)$  is virtually unaffected ( $<1 \text{ cm}^{-1}$ ), Fig. 4.6.

However, at 48.0 kbar a previously unobserved phase change occurs with evidence for its existence being the appearance of a new lattice mode at  $87 \text{ cm}^{-1}$ . Simultaneously there is a  $3.7 \text{ cm}^{-1}$  rise in  $\nu_2$ , nitrite

**Table 4.1** Factor group analysis for sodium nitrite.

$C_{2v}$	$A_1$	$A_2$	$B_1$	$B_2$
Na.(a).	1	0	1	1
N (a)	1	0	1	1
O (2d)	2	1	1	2
$N_{TOT}$	4	1	3	4
$T_A$	1	0	1	1
$N_{OPT}$	3	1	2	3
R	0	1	1	1
T	1	0	1	1
$N_{INT}$	2	0	0	1
Activity	R,i.r.	R	R, i.r.	R, i.r.

$N_{TOT}$  = Total number of modes.

$T_A$  = Acoustic Translatory modes.

T = Non-acoustic Translatory modes.

R = Rotory modes.

$N_{OPT}$  = Total number of optical modes.

$N_{INT}$  = Total number of internal modes.

**Figure 4.3**

Deconvoluted lattice mode spectra of the ambient pressure and high pressure phases of sodium nitrite.

Spectral slit width  $1.0\text{ cm}^{-1}$ , 400 mW  
488.0 nm radiation at sample.

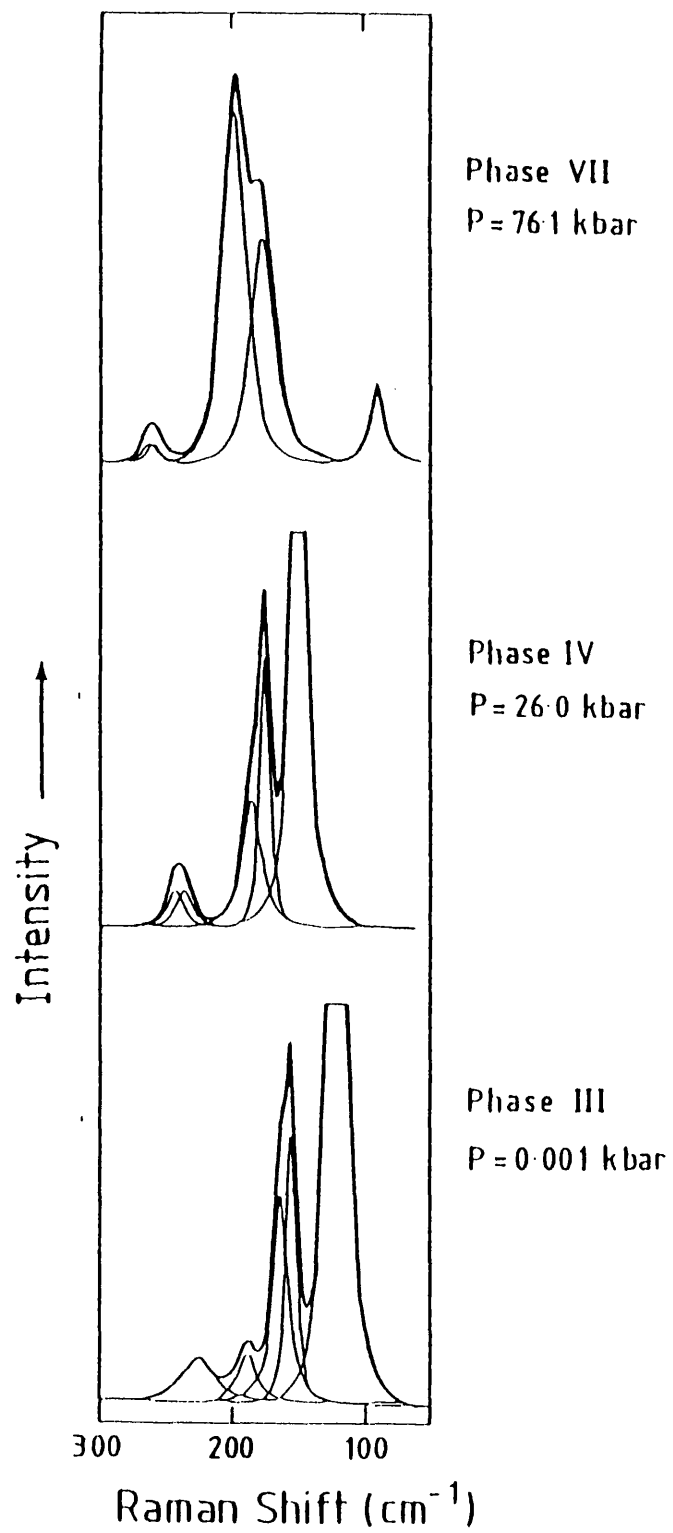




**Figure 4.4**

Raman spectra of  $\text{NaNO}_2$  at high pressure in the internal mode region. Spectral slit width  $1.5\text{ cm}^{-1}$  above  $1000\text{ cm}^{-1}$ ,  $1.0\text{ cm}^{-1}$  below  $1000\text{ cm}^{-1}$ , with 400 mW of 488.0 nm and 514.5 nm radiation at the sample.

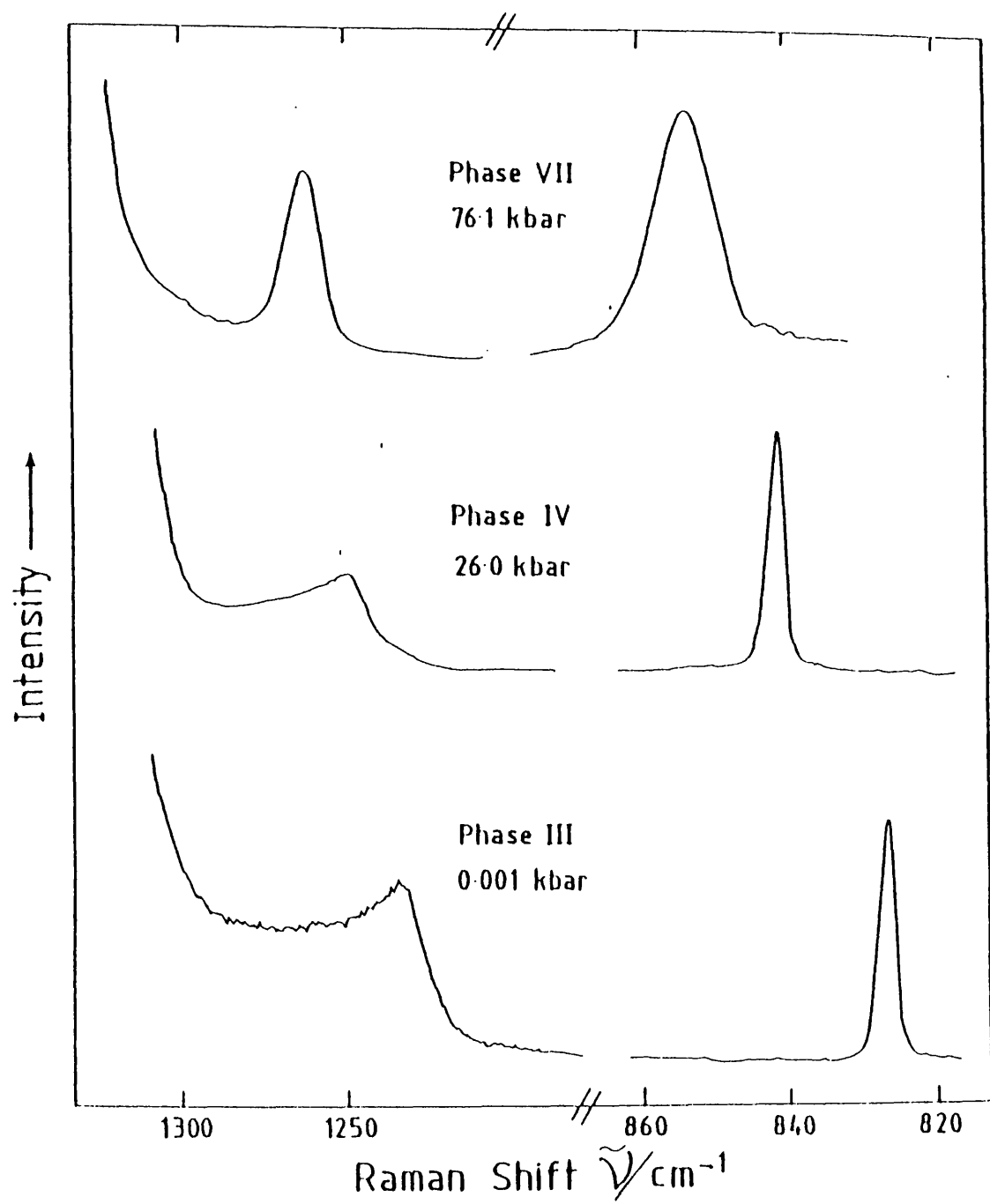


**Figure 4.5**

Presssure dependencies of Raman—active  
lattice modes at room temperature.

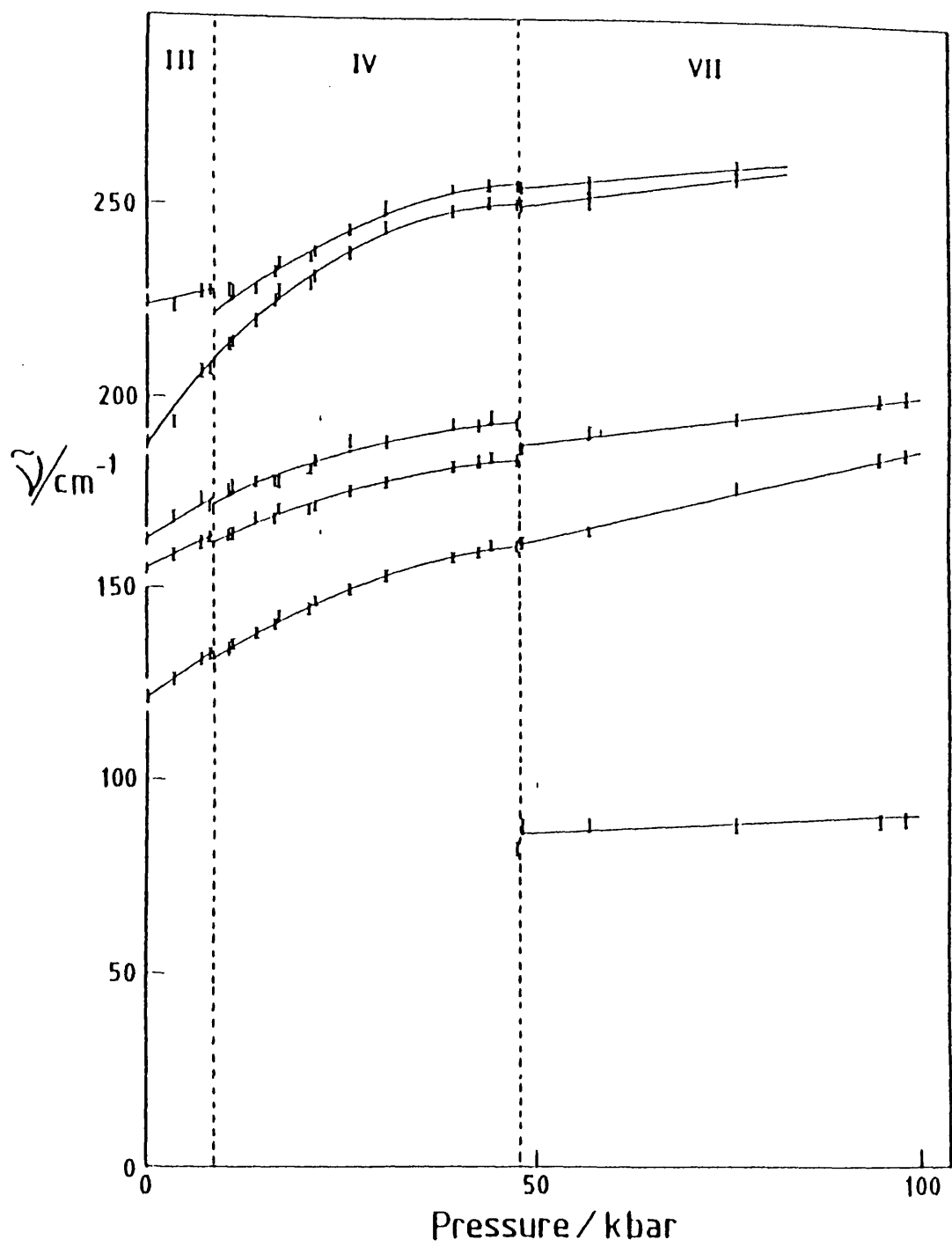
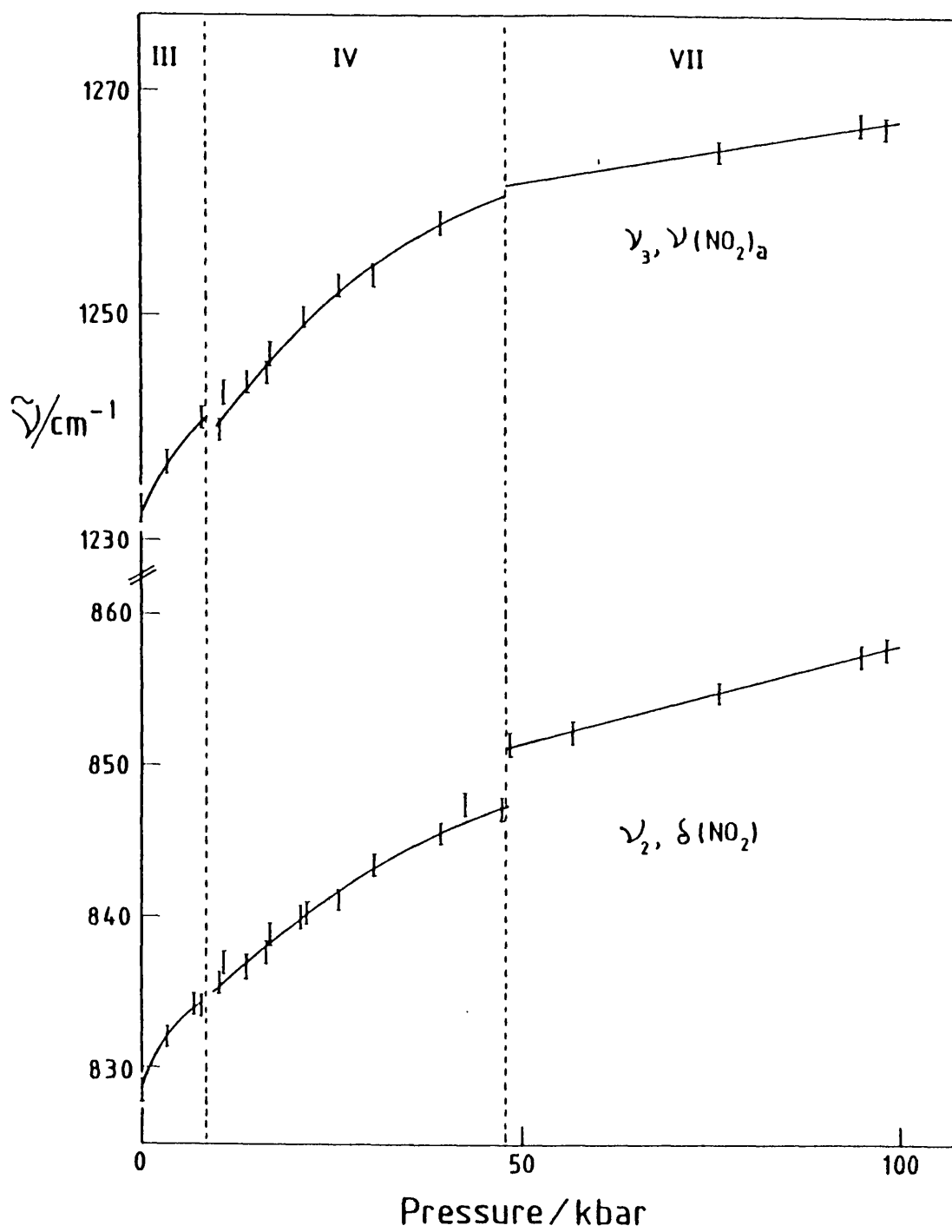


**Figure 4.6**

Pressure dependencies of Raman-active  
internal modes of sodium nitrite at room  
temperature.



deformation, accompanied by a significant increase in integrated intensity and half-band width. This is also accompanied by a lesser although similar enhancement of  $\nu_3$ .

#### 4.4.1 Structure of sodium nitrite, phase IV

The discussion of the structure of phase IV is attempted in the absence of any conclusive structural data. However, the existence of the III/IV transition is not in doubt, and a discussion of the nature of phase IV is possible from the available data. The transition III/IV is almost certainly of a second-order nature, with the evidence for this provided from the very small volume change, 0.6%, which is inconsistent with a fully first-order phase change, but may be consistent with one of second-order.<sup>21</sup> X-ray diffraction maxima broaden slightly above 10 kbar, indicating a deviation from orthogonality of less than  $1^\circ$ , which is likely to be due to a monoclinic distortion at high pressure.<sup>22</sup> Low temperature, ambient pressure Raman spectra of sodium nitrite exhibiting phase IV ie.  $< 178\text{K}$  do not show any spectral changes other than those associated with cooling, further supporting a second-order mechanism.

Since there is no change in the number of Raman active bands in the lattice mode region, we may say that phase IV must have the same cell occupancy. Also, phase IV is required to have a factor-group which is a sub-group of  $C_{2v}$ , by the Landau criterion. The choice of factor-groups is between  $C_1$ ,  $C_2$  and  $C_s$ , this corresponds to the possible space groups,

i) Triclinic      $P1 (C_1^1)$

ii) Monoclinic      $P2 (C_1^2), B2 (C_2^3), Pm(C_s^1)$

or  $Bm (C_s^3)$

All of these space groups are non-centric and will allow a unimolecular unit cell. Since all species in  $C_{2v}$ ,  $C_1$ ,  $C_2$ , and  $C_s$  carry Raman activity there will be no change in the Raman selection rules, other than formal relabelling.

#### 4.4.2 Structure of sodium nitrite phase VII

The IV/VII transition appears to be of a first-order nature, as revealed by the accompanying spectral changes.

Since the lattice mode region appears to stay relatively sharp, disordering as an explanation for the intensity and line width increases observed in the internal modes is unlikely. However, there are two possible explanations for the appearance of the lattice mode at  $87\text{ cm}^{-1}$ .

i) The lattice has repacked, corresponding to a large reduction in some interatomic repulsions, but remains unimolecular at all times, allowing the  $A_2$  mode initially at  $121\text{ cm}^{-1}$  to drop by almost 50% to its new position, or,

ii) the cell has doubled, and the  $87\text{ cm}^{-1}$  band is the result of a zone-boundary phonon.

This latter explanation is the more likely, since any drop in wave number of the type seen in i) would almost certainly be mirrored by a similar movement in the internal modes, as they are not we may disregard this theory with some confidence. The doubling of the unit cell in real space corresponds to a halving in reciprocal space, and can be thought of as bringing the zone boundary phonon back on itself, giving a new value  $\omega'$ .

#### 4.5. Summary

Sodium nitrite displays two high-pressure phase transitions upto 100 kbar, one at 8.5 kbar and one at 48.0 kbar. They are shown to be second-order and first-order respectively.

A list of space groups are given for phase IV based on a Landau sub-group relationship, and evidence for the nature of phase VII is discussed, with no specific reference to space groups, since no adequate structural data are available. Phase VII is almost certainly of a B2 structure type, and all the remaining phases are likely to be of a B1 structure type. Some discussion of this structural relationship will be given with some reference to potassium nitrite in the final section.

#### Potassium Nitrite $\text{KNO}_2$

#### 4.6. Introduction

The structure of  $\text{KNO}_2$  II, the ambient phase, was first reported by,



Ziegler, (1936)<sup>23</sup> with a monoclinic structure being proposed. This was later revised by Chang 1963<sup>24</sup> Tanisaki 1965<sup>25</sup> and then conclusively by Solbakk and Strömme 1969<sup>26</sup> to a rhombohedral system. The space group of phase II is  $D_{3d}^5$  (R3m no. 166), with three molecules per unit cell, displaying dimensions,  $a = 5.006 \text{ \AA}$ ,  $c = 10.190 \text{ \AA}$ . It is considered to be disordered, with a configurational entropy of Rln 12 from Pistorius and Richter 1972<sup>27</sup>, this is supported by a lack of superlattice reflections.<sup>25</sup>

A vibrational assignment, with Raman and mid-infrared data on phase II, has been supplied by Brooker and Irish 1971.<sup>6</sup> All assigned internal modes are reported, Table 4.2, but a broad, featureless Rayleigh scatter instead of a distinct lattice mode region was observed. This is consistent with the disordered structure proposed.<sup>25-27</sup>

#### 4.7.Phase behaviour of potassium nitrite

The phase behaviour of potassium nitrite has been extensively studied at both variable temperature<sup>24-30</sup> and at high pressure.<sup>31-38</sup> The revised phase diagram, Fig 4.7 shows all the known phases of potassium nitrite, including the new phases proposed by this work. There are now thought to be nine polymorphic forms of potassium nitrite, of which four are available at variable temperatures and ambient pressure; I, II, III and VII, and five which are only accessible at elevated pressures; IV, V, VI, VIII and IX. This is deduced from studies covering the P-T range -150 to +180 °C and 0 to 125 kbar.

##### 4.7.1.Ambient pressure phases of potassium nitrite

Phase I displays a cubic structure with a space group  $O_h^5$  (Fm3m) and is known to be highly disordered, with a configurational entropy of Rln 32, Table 4.3, and exhibits an accordingly featureless Rayleigh wing, Fig. 4.8. On lowering the temperature phase I goes through successive phases II, III and VII where phase II is also disordered and is probably closely related to  $\text{KNO}_2$  I.  $\text{KNO}_2$  II subsequently gives way to  $\text{KNO}_2$  III at about -13 °C where the temperature of the transition varies depending on the purity of the sample. This phase exhibits some spectral features in its lattice mode region, which is indicative of a phase displaying some structural order.  $\text{KNO}_2$  III is considered to have a monoclinic space group, probably  $P2_1/c$  ( $C_{2h}^5$ ),  $Z = 4$ .<sup>27</sup>

$\text{KNO}_2$  III evolves into another lower temperature phase at some

**Table 4.2** Vibrational frequencies of  $\text{KNO}_2$  II at ambient temperature and pressure.

Infrared	Raman	Assignment
806(m, shp)	806(m, shp)	$\nu_2 (A_1) \text{NO}_2^-$
837(vw)		$\nu_2 (A_2'') \text{NO}_3^- \text{imp.}$
	1058(w)	$\nu_1 (A_1') \text{NO}_3^- \text{imp.}$
1225(vs)	1240(br)	$\nu_3 (B_2) \text{NO}_2^-$
	1322(vs, shp)	$\nu_1 (A_1) \text{NO}_2^-$
1390(w)		$\nu_3 (E') \text{NO}_3^- \text{imp.}$

(From, Brooker and Irish, 1971)

**Table 4.3** Crystallographic data for polymorphs of  $\text{KNO}_2$ .

<u>Phase</u>		<u>Symmetry</u>		<u>Z</u>	<u>Config.Entropy</u>
I	Cubic	Fm3m	(O <sub>h</sub> <sup>5</sup> )	4	Rln32
II	Rhomb.	R3̄m	(D <sub>3d</sub> <sup>5</sup> )	3	Rln12
III	Monoclinic	P2 <sub>1</sub> /c	(C <sub>2h</sub> <sup>5</sup> )	4	ordered
IV	Rhomb.	R3̄m	(D <sub>3d</sub> <sup>5</sup> )	1	Rln2
V	Cubic	Pm3m	(O <sub>h</sub> <sup>h</sup> )	1	Rln12
VI	Tetragonal	P4 <sub>2</sub> /nmc	(D <sub>4h</sub> <sup>15</sup> )	4	Rln4
	or	P4/ncc	(D <sub>4h</sub> <sup>8</sup> )		
VII	Monoclinic	P2 <sub>1</sub>	(C <sub>2</sub> <sup>2</sup> )	4	ordered
	or	P2 <sub>1</sub> /m	(C <sub>2h</sub> <sup>2</sup> )		
VIII	Unknown				
IX	Unknown				

**Figure 4.7**

The phase diagram of potassium nitrite,  
 $\text{KNO}_2$ .

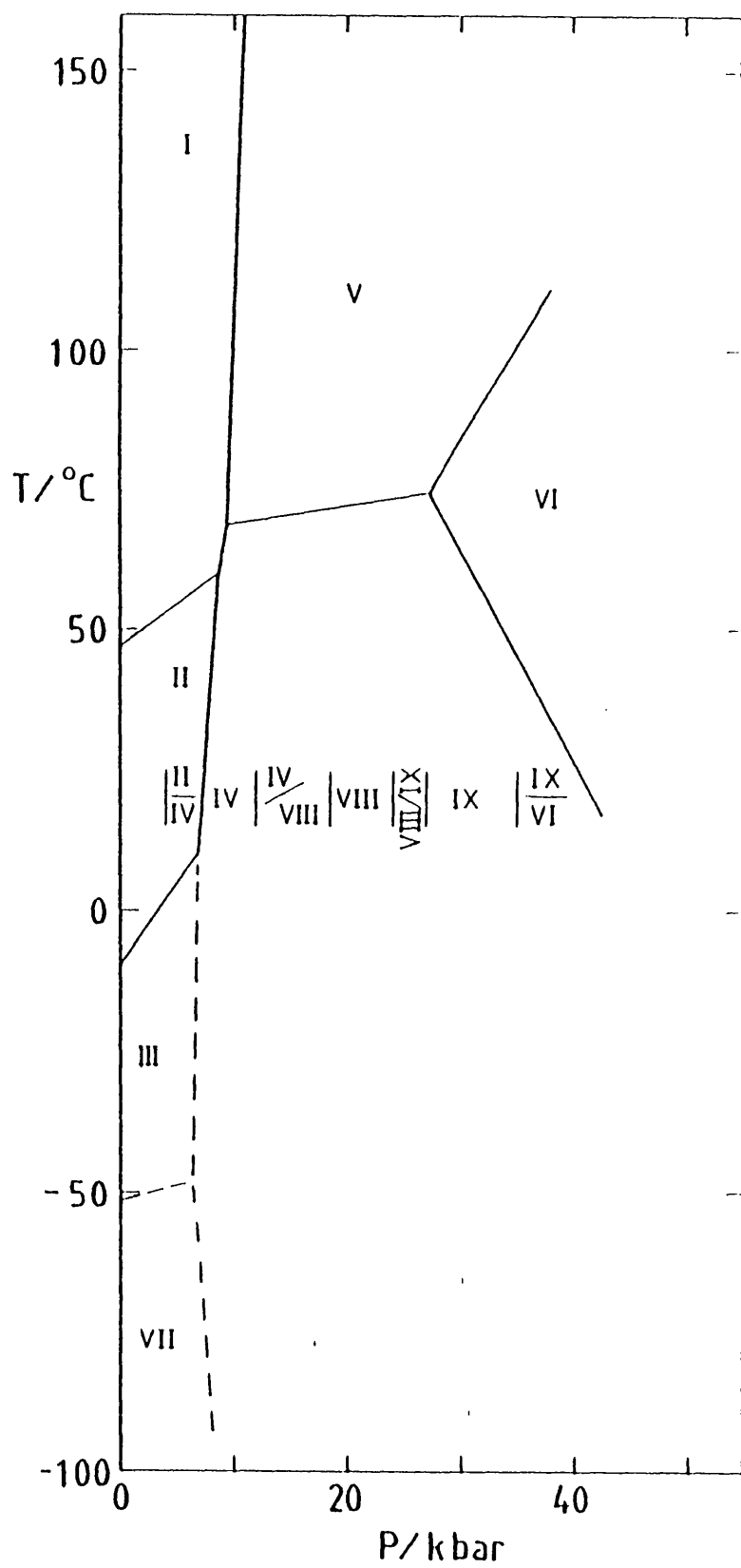


**Figure 4.8**

Raman-active lattice modes of  $\text{KNO}_2$ ,  
phases stable at ambient pressure.  
Spectral slit width  $1.25 \text{ cm}^{-1}$ , 300 mW of  
5.14.5 nm radiation at the sample.

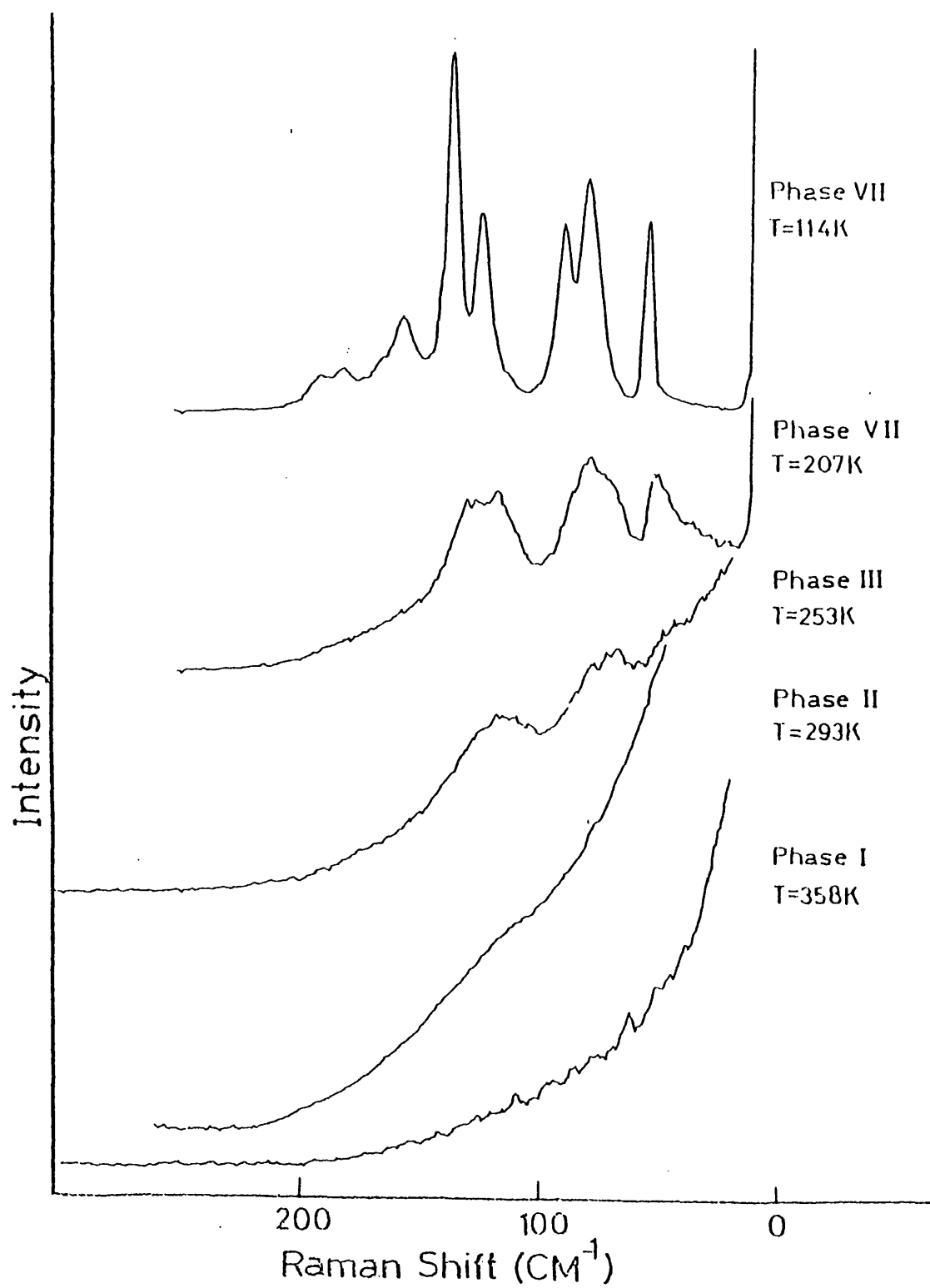


**Table 4.4** Stability regions for high pressure phases and biphasic mixture.

Phase/Mixture	Stability region (kbar)
II	0 – 4.0
II – IV	4.0 – 5.8
IV	5.8 – 12.0
IV – VIII	12.0 – 18.8
VIII	18.8 – 24.0
VIII – IX	24.0 – 27.0
IX	27.0 – 35.0
XI – VI	35.0 – 42.5
VI	42.5 – 125.7



undetermined temperature between  $-35$  to  $-66$   $^{\circ}\text{C}$ . This phase has been designated phase VII and it is thought to display a monoclinic space group, either  $P2_1 (C_2^2)$  or  $P2_1/m (C_{2h}^2)$ , both with  $Z = 4$ .<sup>27</sup> A well defined lattice mode region is indicative of this phase.

#### 4.7.2. High pressure phases of potassium nitrite

The result of increasing pressure on phase II at 293 K is a partial transformation to  $\text{KNO}_2$  IV at 4.0 kbar, as revealed by the  $\nu_2$  region. There is a full transformation to phase IV at 6.0 kbar, which is indicated by all spectral regions studied. This fits well with the reported transition pressures of 5.9 kbar<sup>38</sup> and  $6.4 \pm 0.4$  kbar.<sup>32</sup> The distinctive feature of phase IV is the emergence of a strong lattice mode spectrum with no residual Raleigh wing, Fig. 4.9. This new ordered phase  $\text{KNO}_2$  IV, has had its powder pattern indexed on the basis of a rhombohedral cell with the same space group as phase II but lattice parameters  $a = 4.050 \pm 0.015$  Å and  $\alpha = 82.9 \pm 0.5^{\circ}$ ,  $Z = 1$ ,<sup>37</sup> although this is unlikely to be correct as judged by a spectral study on phase IV.

Further increases of pressure at room temperature result in  $\text{KNO}_2$  going through a number of structural changes, which are illustrated by Figs. 4.9 and 4.10. All phase boundaries are obscured by the existence of an area of intergrowth between adjoining phases. The areas of stability of both pure phases and biphasic intergrowth are displayed, Fig. 4.11 a), b) & c) and Table 4.4.

Phase IV gives way to phase VIII which has been previously reported,<sup>38</sup> although no suggestion of the exact transition pressure was given. At 22.7 kbar a change was detected at approximately  $100 \text{ cm}^{-1}$ ; this is now thought to be a mixture of phases VIII/IX with pure phase VIII shown in Fig. 4.9. The region of stability of pure phase VIII is from present work, 18.8 kbar – 24.0 kbar.

At still higher pressures a previously undetected phase was encountered. It was initially thought to be of a similar structural type to phase VIII and has been labelled phase IX. However, the small volume change between it and phase VI, as well as the change in relative intensities of the lattice mode regions compared to phases IV and VIII, suggests that it may be more akin to phase VI. Adams and Sharma 1977, thought that  $\text{KNO}_2$  VIII continued through the area of stability now designated phase IX, but the use of deconvolution routines (see experimental chapter) and accurate phonon shift data have now revealed

**Figure 4.9**

The deconvoluted Raman-active lattice modes of  $\text{KNO}_2$  at ambient temperature and high pressures. Both pure phases and biphasic mixtures are shown. The bands which are outlined are considered to be indicative of the phase changes displayed. Spectral slit width  $1.5 \text{ cm}^{-1}$ , power 400 mW, 488.0 nm and 514.5 nm radiation at sample.

# Lattice Modes of $\text{KNO}_2$

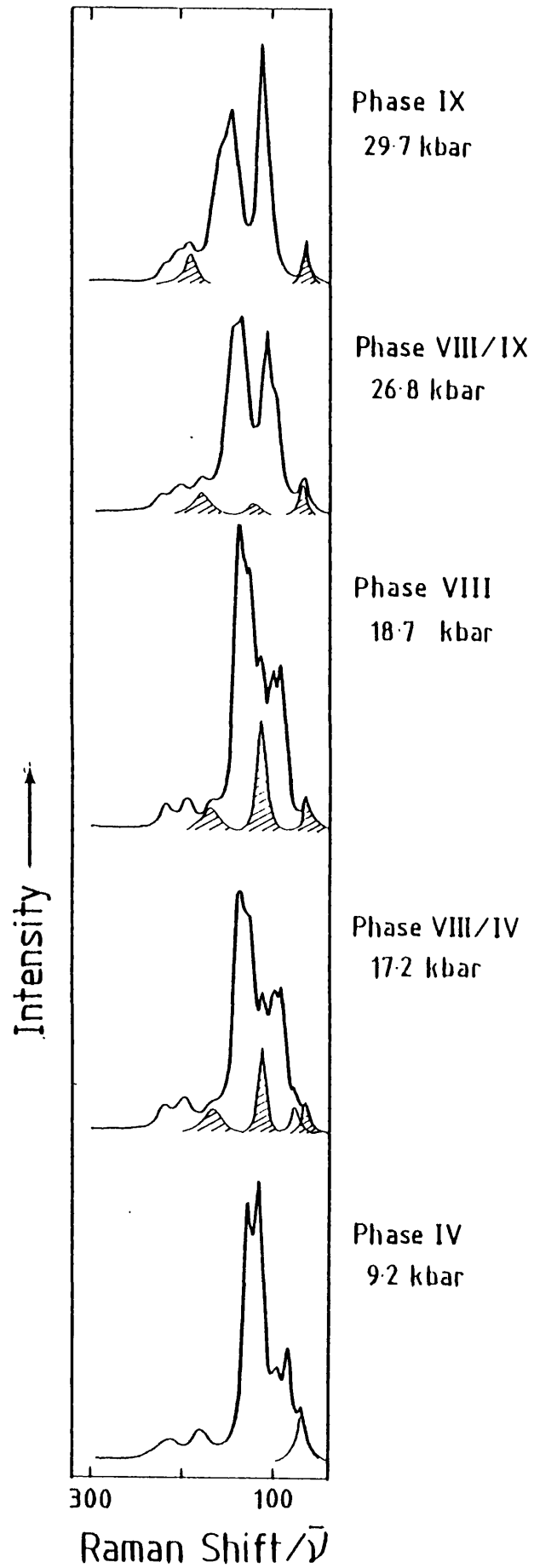


Figure 4.10

Raman-active internal modes of  $\text{KNO}_2$  at ambient temperature and high pressures. Spectral slit width  $2.0 \text{ cm}^{-1}$  above  $1000 \text{ cm}^{-1}$ ,  $1.0 \text{ cm}^{-1}$  below  $1000 \text{ cm}^{-1}$ , except in phase VI when  $1.0 \text{ cm}^{-1}$  resolution was used above  $1000 \text{ cm}^{-1}$ . 400 mW, 488.0 nm and 514.5 nm radiation at sample.

# Internal Modes of $\text{KNO}_2$

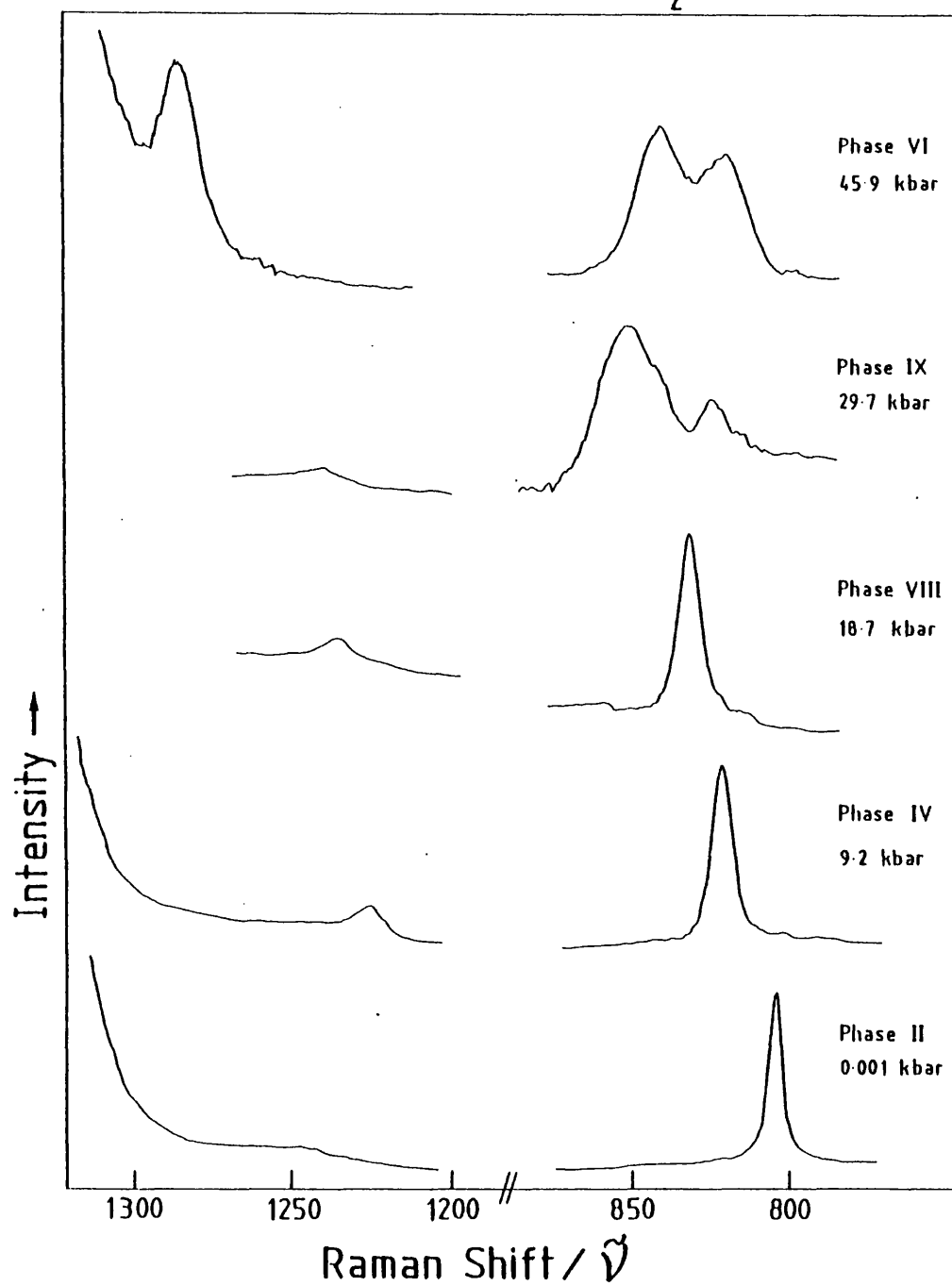


Figure 4.11 a)

Pressure dependencies of Raman—active  
lattice modes of potassium nitrite at  
ambient temperature.

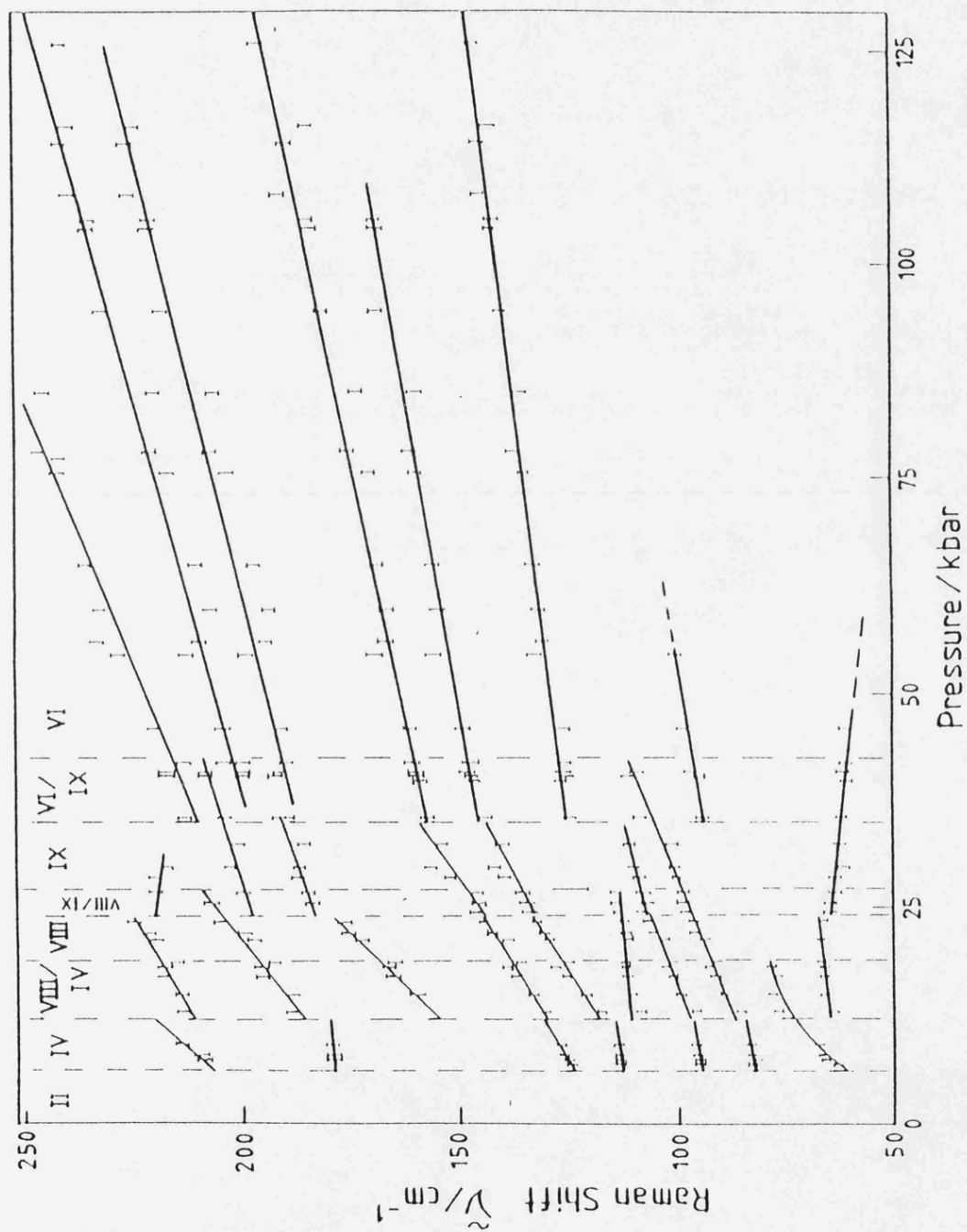


Figure 4.11 b)

Pressure dependencies of Raman-active  $\nu_2$ ,  
 $\delta(\text{NO}_2)$  region of  $\text{KNO}_2$ .



$\nu_2$  Region,  $\delta(\text{NO}_2)$  of  $\text{KNO}_2$

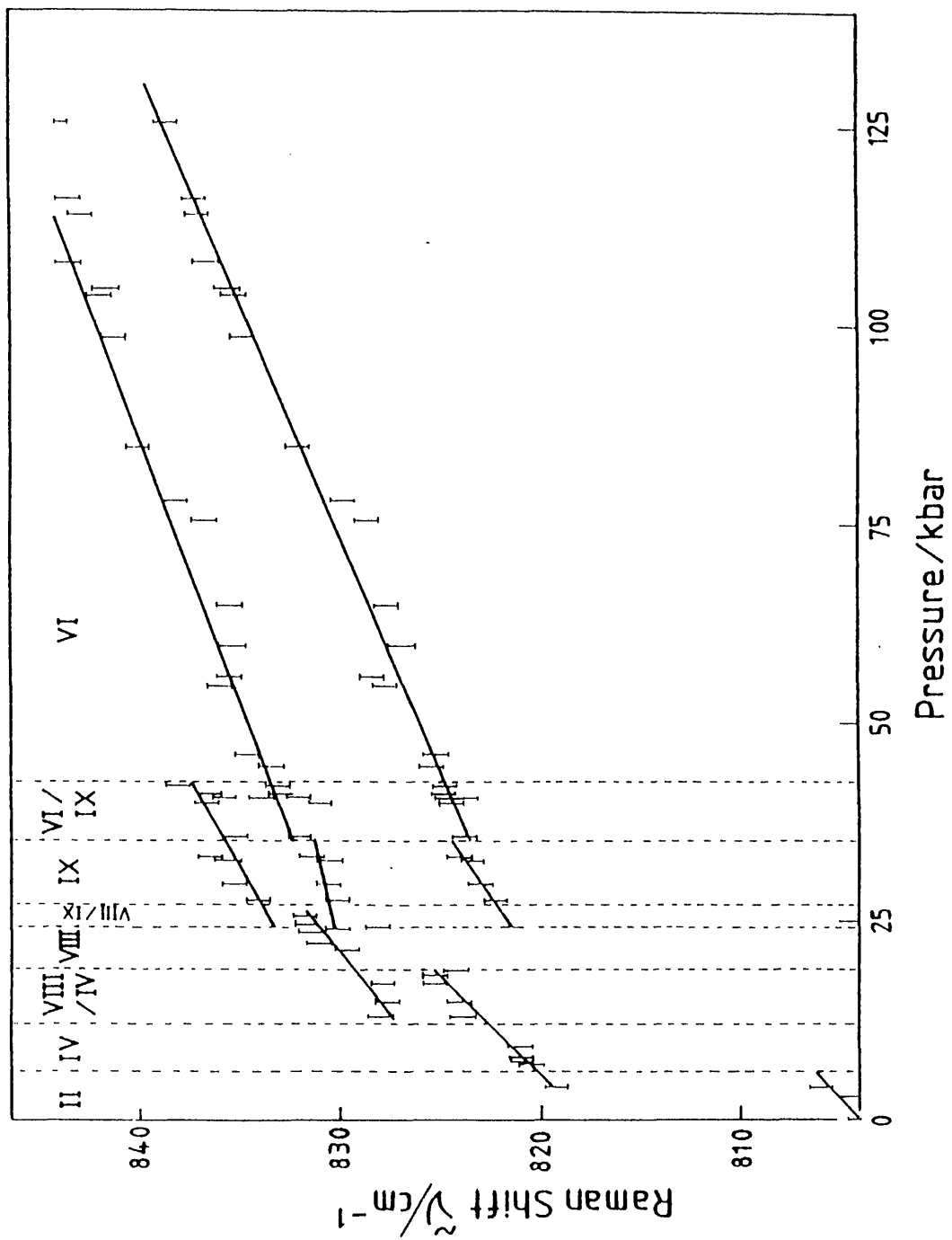
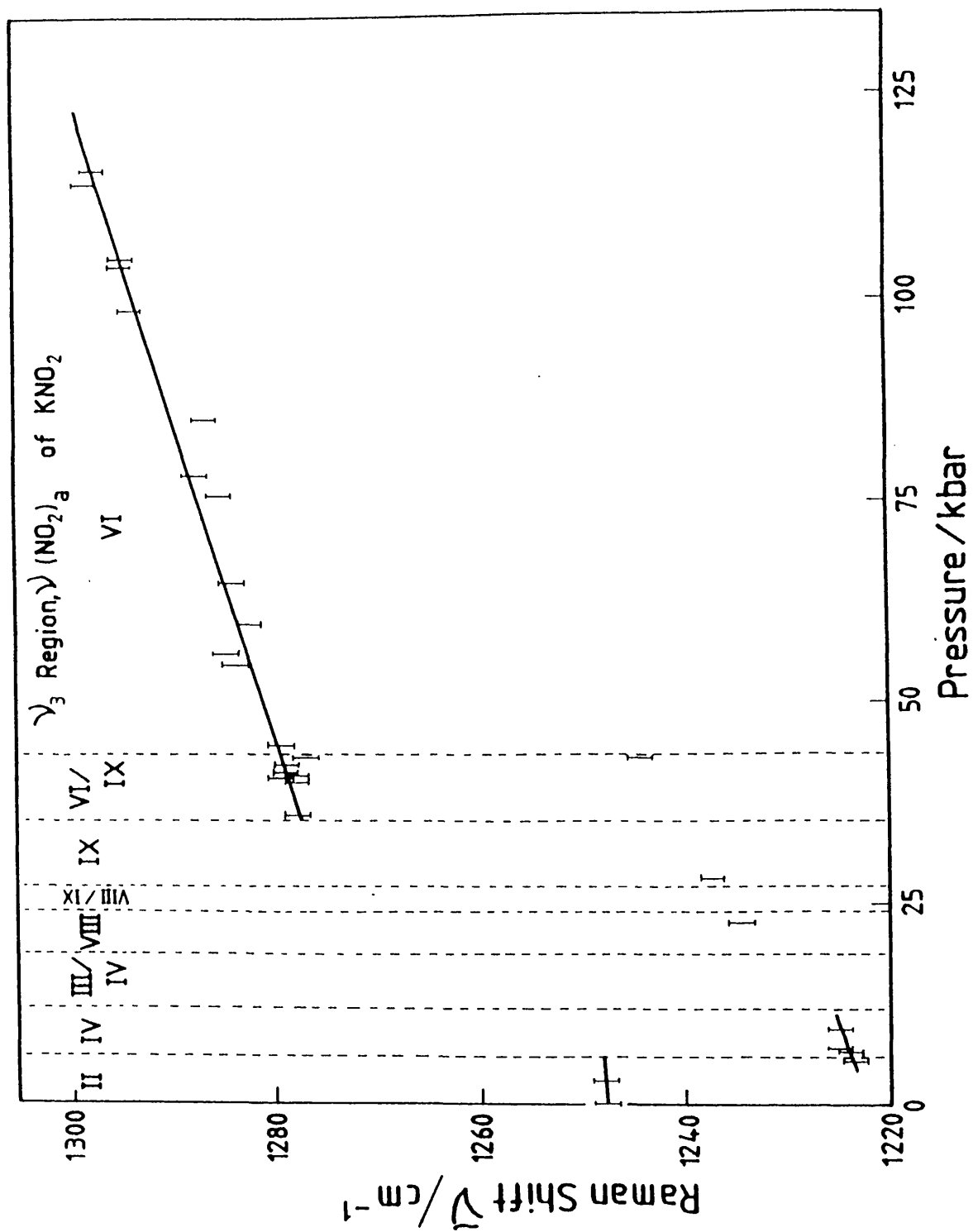


Figure 4.11 c)

Pressure dependencies of Raman-active  $\nu_3$ ,  
 $\nu(\text{NO}_2)_{\text{as}}$  of  $\text{KNO}_2$ .



this extra phase. The region of stability of pure phase IX is 27.0 kbar to 35 kbar. At 42 kbar phase VI has been detected, this is at a lower pressure than the 51.6 kbar previously reported.<sup>38</sup> A tetragonal space group of  $D_{4h}^8$  (P4/ncc) or  $D_{4h}^{15}$  (P4<sub>2</sub>/nmc),  $Z = 4$  was suggested. The IX/VI transition is first order, since a small volume change of  $0.36 \pm 0.13 \text{ cm}^3 \text{ mol}^{-1}$  is detected.<sup>37</sup> DTA experiments also revealed the transition at 326.5 K and 40 kbar.<sup>32</sup> No further changes were detected up to 125 kbar pressure and 293 K.

Finally, there exists a high pressure, high temperature phase which is designated  $\text{KNO}_2$  V. It is thought to be a cubic transformation, space group  $O_h^1$  (Pm3m)  $a = 3.887 \text{ \AA}$  and  $Z = 1$ , and has been detected in its pure form at 360 K and 18.5 kbar<sup>37</sup> also 336 K and 10.5 kbar.<sup>38</sup> It is disordered and closely related to  $\text{KNO}_2$  I, showing a similar broad Rayleigh line in the lattice mode region.

#### 4.8. Experimental

Analar grade  $\text{KNO}_2$  was used in a diamond anvil high pressure cell (DAC). Pressures were estimated by the ruby R-line method. The samples were contained within stainless steel or inconel gaskets with hole diameter 0.4 mm and thickness 0.2 mm (initial dimensions). Spectra were excited with 488.0 nm and 514.5 nm  $\text{Ar}^+$  radiation of approximately 400 mW power.

Any modes arising from the  $\nu_1$ ,  $\nu(\text{NO}_2)_s$  could not be followed at any time as they were obscured by the intense first-order phonon line of diamond at  $1332 \text{ cm}^{-1}$ . All samples and equipment were dried over night at 393 K and loading the DAC was done in a dry environment, this is necessary due to the hygroscopic nature of potassium nitrite.

#### 4.9. High pressure results

Representative Raman spectra recorded at various pressures and ambient temperatures, are shown in Figs. 4.8–4.10. Phonon shifts with pressure are displayed in Figs. 4.11a–c, and Tables 4.5.

i) II–IV This transition is complete by 6.0 kbar, although phases II and IV co-exist over a short range, Table 4.4. The clearest indication of this transition is the appearance of a strong, clear lattice mode spectrum, with strong features centred around  $80 - 130 \text{ cm}^{-1}$  replacing the broad Rayleigh wing. Large shifts in the positions of both the  $\nu_2$  region, which rises  $14 \text{ cm}^{-1}$  from  $806 - 820 \text{ cm}^{-1}$ , and the  $\nu_3$

**Table 4.5** Raman shifts and their pressure dependencies for pure phases of potassium nitrite.

	External modes		Internal modes	
	$\nu_i \text{ cm}^{-1}$	$d\nu_i/dP$	$\nu_i \text{ cm}^{-1}$	$d\nu_i/dP$
<u>Phase II</u>	(broad featureless Rayleigh wing)		803.9	0.414
			1247.5	0.069
<u>Phase IV</u>	60.0	(curve)	820.2	0.387
	82.5	0.3	1224.0	0.258
	94.8	0.307		
	113.2	0.259		
	124.3	1.113		
	178.8	0.016		
	206.3	2.258		
<u>Phase VIII</u>	66.2	0.212	829.2	0.327
	92.3	0.808		
	97.6	1.039		
	112.3	0.269		
	127.0	1.269		
	138.5	1.192		
	168.5	2.096		
	196.2	1.596		
	218.7	1.154		

Cont.

**Table 4.7** (Continued)

<u>Phase IX</u>	63.0	-0.133	822.2	0.172
	99.4	0.516	830.5	0.054
	109.0	0.305	833.9	0.133
	136.5	0.601		
	148.5	0.836		
	185.5	0.429		
	199.5	0.383		
	219.2	-0.172		

<u>Phase IV</u>	60.7	0.200	824.8	0.167
	97.0	0.300	833.4	0.149
	127.8	0.238	1279.4	0.250
	148.3	0.165		
	150.5	0.414		
	191.0	0.484		
	202.0	0.544		
	216.0	0.831		

$\nu_i$  : Initial Raman shift at phase  
boundary.

region which drops  $24\text{cm}^{-1}$  from  $1248 - 1224\text{ cm}^{-1}$  also occur. This is indicative of the ordering taking place at this transition.

ii) IV-VIII This is a sluggish transition with a region of intergrowth spanning 6.8 kbar, upto 18.8 kbar, and pure phase VIII up to 24.0 kbar.

The spectrum has become more complicated in the lattice mode region with the emergence of three new bands, initial wavenumbers 65.0, 111.0 and  $154\text{ cm}^{-1}$ . However, one band is also lost, initial wave number  $63\text{ cm}^{-1}$ . The  $\nu_2$  region shows a further rise of  $4.2\text{ cm}^{-1}$  with no notable change of intensity. The  $\nu_3$  band becomes increasingly difficult to follow and for phase VIII only one phonon position was available  $1227.3\text{ cm}^{-1}$ . Nevertheless, the  $\nu_3$  band appears to be shifting upwards with pressure.

iii) VIII-IX This transition is also sluggish with a biphasic region spanning 3 kbar, between 24.0 - 27.0 kbar. The transition can be recognised easily by the appearance of a complex  $\nu_2$  region with apparently three components. The two lower frequency components, from phonon shift measurements, appear to be the new additions. The  $\nu_3$  region follows a similar pattern to that of phase VIII, although still difficult to follow, there is evidence for a steady increase in frequency.

The lattice mode spectrum is similar to that of phase VIII, with differences in intensity of some bands between  $100 - 170\text{ cm}^{-1}$ . The disappearance of a band at approximately  $113\text{cm}^{-1}$ , although difficult to follow is also an indicator.

iv) IX-VI This transition is probably of a first order type, displaying obvious spectral changes along with anomolous volume changes. Pure phase VI is obtained at 44.0 kbar with an observed region of intergrowth between 35.0 kbar and 43.5 kbar.

The spectral features indicating phase VI are the well defined doublet at  $824.8\text{ cm}^{-1}$  and  $833.5\text{ cm}^{-1}$  in the  $\nu_2$  region and the re-emergence of a strong and greatly shifted  $\nu_3$ , at  $1277\text{cm}^{-1}$ . Although the lattice mode region has not apparently lost or gained bands, the change in intensity is quite striking and almost certainly indicates a change of structure type.

On characterising these "lower" pressure phases, spectra were then obtained at pressures up to 125.7 kbar. There were no abrupt changes in the gradient of the frequency versus pressure plots and no new Raman active modes, which suggests that no further phase transformation occurs between 43.5 kbar and 125.7 kbar at room temperature.

#### 4.10. Structural implications of Raman spectra

Of the nine phases of  $\text{KNO}_2$  a known or postulated space group has been suggested for seven of them, Table 4.3, the four ambient pressure phases I, II, III and VII, and the three high pressure variants IV, V and VI. Of these seven polymorphs the three high pressure phases were deduced via X-ray powder patterns, and do not have a full and accurate range of crystallographic data.

However, reasonable crystallographic data have been obtained for the ambient pressure variants. Of these four phases the two highest temperature phases are disordered, "statistical" structures with phase I displaying a NaCl type arrangement, where no full factor group analysis to reveal its vibrational spectrum is possible, although the internal vibrations of  $\text{KNO}_2$  II have been identified.<sup>28</sup> Phases III and VII when subjected to factor group analysis yield inconsistent results when compared with actual Raman spectra.

The three phases which are known to have very high configurational entropies (I, II and V) have two features in common:

i) Below  $200\text{ cm}^{-1}$  they show only a broad Rayleigh wing with little or no structure.

ii)  $\nu_3$  is absent from the spectra as a discrete band, but is replaced by a broad region of scatter.

$\text{KNO}_2$  V differs significantly from I and II in showing a broad and structured  $\nu_2$  region rather than a single sharp band. It is suggested that with increase of pressure the lifetimes of the various configurations contributing to the disordered state are lengthened. Accordingly the Raman process will sample a variety of different configurations and has subsequently yielded the observed broad envelope near the  $\nu_2$  position.

It is also possible that this structure observed in phase V is due to the anions interchanging via two different mechanisms. The expected rotation about  $C_2$ -axis of  $\text{NO}_2^-$  the axis normal to the plane of the anion may be disfavoured at high pressures relative to rotation about an axis parallel to the O-O, direction which involves a "flip" of the nitrogen positions. This type of process has been detected in ferroelectric  $\text{NaNO}_2$ .<sup>39</sup>



In contrast to  $\text{KNO}_2$  I, II and V, phases III, IV, VI, VII, VIII and IX show lattice mode spectra which are plainly indicative of a much higher degree of order. The broad similarities between those spectra of phases III, IV, VI, VII, VIII and IX in terms of frequency and relative band intensities seems to suggest that they are all variants of one structure type (B2) where phases I, II, and V are likely to be B1 related. Although on further inspection  $\text{KNO}_2$  VI may be unique based on this criterion. The small volume change accompanying the IX to VI (previously IV to VI) transition led Pistorius 1972 and ourselves to suggest, when considering the complexity of the nitrite deformations, that both are a further variation of the B2 lattice type.

$\text{KNO}_2$  IV has been initially assigned a rhombohedral structure, Table 4.3,  $R3m (D_{3d}^5)$  with  $Z = 1$ . A feasible interpretation of our discovery of the second-order phase transition IV/VIII, is a disorder - order mechanism with phase VIII possessing the ordered form of phase IV. This may be extended to phase IX, which has a similar lattice mode spectrum to phases IV and VIII, less one band, implying perhaps further ordering. Further evidence for this ordering may be gained from comparing phase IX with phase VII. The number and positions of the bands and the overall profile of the lattice mode region suggests that they may have similar structures, perhaps being ordered variants of phases IV and VIII.

However, it is unlikely that the structure proposed on the basis of the X-ray data for phase IV is correct in that it cannot account for the lattice mode spectra of either phase IV or VIII containing nine bands, or phase IX containing eight bands. If we attempt to predict the lattice mode spectrum on the basis of a rhombohedral cell with the proposed sites for potassium being (1a) and nitrogen being (1b) we acquire the selection rules;

Rotatory  $A_{2g} + E_g$  (both Raman active)

Translatory(optic)  $A_{2u} + E_u$  (ir active)

This gives a maximum of only two Raman active lattice modes, implying that phases IV, VIII and IX are not related to this structure. If these phases are fully ordered and are related to this rhombohedral cell, the Raman spectra would imply a unit cell of some complexity, certainly  $Z = 4$ .

We note that the ordered phase VII shows eight bands in the lattice mode region. Unfortunately, a factor group analysis based on the proposed tetramolecular monoclinic cells  $P2_1/m$  and  $P2_1$  give  $9A_g + 9B_g$  (rotatory plus translatory) and  $17A + 16B$  (all Raman active) respectively, implying that we have either the wrong space group or the wrong cell occupancy.

Since  $KNO_2$  VII is an ordered phase and there is no observable factor-group splitting for  $\nu_2$  in this phase, the presence of the well separated  $\nu_2$  doublet in phase VI is to be understood in terms of anions on two distinct sites. This fact taken together with the apparently unique lattice mode spectrum, suggests that  $KNO_2$  VI has a complicated structure with a unit cell containing more than one crystallographically distinct set of anions. The proposed structures do not account for the lattice mode spectrum of phase VI, which reveals eight Raman active modes. Two space groups of tetragonal symmetry were proposed,<sup>37</sup>  $P_4/ncc$  and  $P_4/nmc$  both with  $Z = 4$ . When considering  $P_4/ncc$ , sites of (4b) for potassium and (4c) for nitrogen, give the lattice mode selection rules for Raman active modes as,

$$\text{Rotatory } A_{2g} + E_{2g}$$

$$\text{Translatory(optic) } A_{1g} + A_{2g} + B_{1g} + B_{2g} + 4E_g$$

giving a total of eleven Raman active lattice modes. For the space group  $P_4/nmc$ , sites (2a) for potassium and (4d) for nitrogen, give the lattice mode selection rules for Raman active modes;

$$\text{Rotatory } A_{2g} + 2E_g$$

$$\text{Translatory(optic) } A_g + 3B_{1g} + 4E_g$$

again revealing a total of eleven bands. These inconsistencies may be accounted for by supposing that when the powder pattern of phase VI was taken an orthorhombic distortion of the unit cell, i.e.  $a \sim b$  was masked. This immediately suggests new possibilities, however, without better resolved powder patterns this distinction will not be made clear.

#### 4.11. The structural relationship of the univalent nitrites

The polymorphism of the univalent nitrites should prove particularly interesting because of the variety of possible closely related structures imposed upon them by the spatial requirements of the V-shaped nitrite ion. There are also possibilities for progressive disordering at higher temperatures. These types of simple salts display a B1/B2 structural relationship. Hence, analogies can be drawn between the phase diagrams of both sodium nitrite and potassium nitrite.

Although no crystallographic data are available for  $\text{NaNO}_2$  V and VI, it is plausible that phase VI may be the disordered B1 structure of  $\text{KNO}_2$  I and, if so,  $\text{NaNO}_2$  V may well be rhombohedral with the  $\text{KNO}_2$  II structure. All phases of sodium nitrite are B1 related except phase VII which is almost certainly B2. If it is B2 related it may be of a structural type similar to either  $\text{KNO}_2$  IV, V, VI, VIII or IX. Phases V and VI may be eliminated, since V is an ordered variant of the disordered  $\text{KNO}_2$  I and phase VI is a tetragonal or orthorhombic distortion of the B2 arrangement. This leaves phases IV, VIII and IX but without detailed crystallographic data drawing further analogies is difficult. However, broad analogies may be made when considering progressive ordering with temperature, in particular  $\text{NaNO}_2$  III with  $\text{KNO}_2$  III, also  $\text{KNO}_2$  VII with  $\text{NaNO}_2$  IV which both appear to be monoclinic with possible non-centrosymmetric space groups.

## References

- 1) Ziegler, G.E. (1931), *Phys. Rev.*, 38, 1040.
- 2) Carpenter, G.B. (1952), *Acta Cryst.*, 5, 132–135.
- 3) Truter, M.R. (1954), *Acta Cryst.*, 7, 73–77.
- 4) Carpenter, G.B. (1955), *Acta Cryst.*, 8, 852–853.
- 5) Chisler, E.V. and Shur, M.S. (1966), *Phys. Status Solidi*, 17, 163.
- 6) Chisler, E.V. and Shur, M.S. (1966), *Phys. Status Solidi*, 17, 173.
- 7) Tramer, A. (1959), *Compt. Rend.*, 248, 3546.
- 8) Asawa, C.K. and Barnoski M.K. (1970), *Phys. Rev. B*, 2, 205.
- 9) Tsuboi, M., Terada, M. and Kajiura, T. (1968), *Bull. Chem. Soc. Japan*, 41, 2545.
- 10) Tsuboi, M., Terada, M. and Kajiura, T. (1969), *Bull. Chem. Soc. Japan*, 42, 1871.
- 11) Tanisaki, S. (1963), *J. Phys. Soc. Japan*, 18(8), 1181.
- 12) Yamada, Y., Shibuya, I. and Hoshino, S. (1963), *J. Phys. Soc. Japan*, 18(11), 1594.
- 13) Böhm, H. (1978), *Z. Kristallog.*, 148, 207–220.
- 14) Böhm, H. (1983), *Am. Min.*, 68, 11–17.
- 15) Heine, V. and MacConnel, J.D.C. (1981), *Phys. Rev. Letters*, 46(16), 1092.
- 16) MacConnel, J.D.C. (1983), *Am. Min.*, 68, 1–10.

- 17) Gesi, K. (1969), *J. Phys Soc. Japan*, 26(4), 953.
- 18) Bridgman, P.W. (1937), *Proc. Am. Soc. Arts Sci.*, 72, 45.
- 19) Rapoport, E. (1966), *J. Chem. Phys.*, 45, 2721.
- 20) Adams, D.M. and Sharma, S.K. (1981), *J. Mol. Structure*, 71, 121-129.
- 21) Richter, P.W., Clark, J.B. and Wolbarst, A.B. (1977), *High Temp. - High Pressures*, 9, 103.
- 22) Hazen, R.M. and Finger, L.W., private communication.
- 23) Ziegler, G.E. (1936), *Z. Krist.*, 94, 491.
- 24) Chang, Shih-Chi (1963), *Diss. Abstr.*, 24, 1668.
- 25) Tanisaki, S. and Ishimatsu, T. (1965), *J. Phys. Soc. Japan*, 20, 1277.
- 26) Solbakk, J.K. and Stromme, K.O. (1969), *Acta. Chem. Scand.*, 23, 300-313.
- 27) Pistorius, C.W.F.T. and Richter, P.W. (1972), *Z. Anorg. Allgem. Chem.*, 389, 315-320.
- 28) Brooker, M.H. and Irish, D.E. (1971), *Canad. J. Chem.*, 49, 1289.
- 29) Ray, J.D. (1960), *J. Inorg. Nucl. Chem.*, 15, 290-292.
- 30) Ray, J.D. and Ogg, R.A. (1956), *J. Phys. Chem.*, 15, 1599-1600.
- 31) Bridgman, P.W. (1915), *Proc. Am. Acad. Arts Sci.*, 51, 55-125.
- 32) Rapoport, E. (1966), *J. Chem. Phys.*, 45, 2721-2728.

- 33) Clark, J.B. and Rapoport, E. (1968), *J. Chem. Phys.*, 49, 2453-2454.
- 34) Pistorius, C.W.F.T., Clark, J.B. and Rapoport, E. (1968a), *J. Chem. Phys.*, 48, 5123-5131.
- 35) Pistorius, C.W.F.T., Clark, J.B. and Rapoport, E. (1968b), *Z. Phys. Chem. (Frankfurt)*, 59, 200-205.
- 36) Larionov, L.V. and Livshitz, L.D. (1970), *Izv. Phys. Solid Earth*, 697-698.
- 37) Pistorius, C.W.F.T. (1972), *High temp.-High pressure*, 4, 77-84.
- 38) Adams, D.M. and Sharma S.K. (1977), *Solid State Comm.*, 23, 729-731.
- 39) Hartwig, C.M., Wiener-Arnebar, E. and Porto, S.P.S. (1972), *Phys. Rev. B.*, 5, 79.

## CHAPTER FIVE

A RAMAN STUDY OF THE PHASE BEHAVIOUR OF METHYL MERCURY HALIDES, CH<sub>3</sub>HgX,  
(X = Cl, Br & I), AT HIGH PRESSURE AND RELATED SOFT MODES.

## CHAPTER FIVE

### A RAMAN STUDY OF THE PHASE BEHAVIOUR OF METHYL MERCURY HALIDES, $\text{CH}_3\text{HgX}$ , ( $\text{X} = \text{Cl}, \text{Br} \text{ \& \; I}$ ), AT HIGH PRESSURE AND RELATED SOFT MODES.

#### 5.1. Introduction

Several solid state phase transitions involving molecular internal torsion are known. Examples of this type of behaviour have been previously observed in the series of hexaammine salts  $[\text{M}(\text{NH}_3)_6]\text{X}_2$ ,  $\text{M} = \text{Cd}, \text{Ni}$ . Here, the initially cubic ambient temperature crystal is compatible with a model in which there is free rotation about the Ni-N bonds but, phase transitions occur with change of temperature<sup>1-4</sup> or pressure,<sup>5</sup> yielding lower-symmetry structures in which the H-positions are ordered. Also, with increased pressure both  $\text{M}_2(\text{CO})_{10}$  where  $\text{M} = \text{Mn}$  and  $\text{Re}$ , undergo first-order phase transitions in which the initially staggered configuration is replaced by the eclipsed one.<sup>6</sup>

A study on the series  $\text{CH}_3\text{HgX}$  where  $\text{X} = \text{Cl}, \text{Br}$  and  $\text{I}$  has been made. This group of compounds has been chosen for their apparent simplicity of structure and because they display only one torsional mode.

This study has revealed a number of phase transitions, which by analogy with the above examples would be expected, since the observed tetragonal space group of  $\text{CH}_3\text{HgCl}$  is compatible with free methyl rotation. All studies were carried out at elevated pressure or low temperature, each material shows at least one phase change, which are indicated by changes in the Raman spectrum. Also, a soft mode has been observed in each material.

#### 5.2. Experimental

Commercial samples of  $\text{CH}_3\text{HgX}$  ( $\text{X} = \text{Cl}, \text{Br} \text{ \& \; I}$ ) were sublimed or recrystallized from benzene or methanol. Spectra recorded under high pressure were obtained using a diamond anvil cell with gaskets made from



either inconel or stainless steel, with initial dimensions of 0.2 mm thickness and sample hole diameter of 0.4 mm. Pressures were estimated using the ruby R-line method. Spectra were recorded on a Coderg T800 triple monochromator using approximately 30-50 mW of 514.5 nm excitation. An Oxford Instrument DN 704 cryostat was used for the low-temperature runs. High temperatures were achieved by heating small capillaries within a furnace based upon an electrical heating coil design.

### 5.3 Evidence for phase transitions

When the three compounds in the series MeHgX were studied optically in the ungasketed mode within the diamond anvil cell (d.a.c.), the resulting pressure gradient revealed distinct changes in refractive index at the phase boundaries, these being displayed as the so-called Becke lines. They have been observed in all three compounds. This further suggests that the transitions are first order in type, since this change in refractive index is accompanied by a volume change, unlike continuous second order transitions, where Becke lines are not observed.

For  $\text{CH}_3\text{HgCl}$  we observed three Becke lines. The mode shifts with pressure, Figs. 5.1 & 5.2 and Table 5.1, indicate the existence of three phase transitions. The first at  $1.5 \pm 0.3$  kbar, is shown by several breaks and changes of slope in the  $\text{d}\omega/\text{d}P$  plots, but there is apparently no change in the number of bands observed from one phase to the next. Subsequent evidence from soft mode data supports the first order nature of the transition.

Major changes are also observed at 5.9 kbar, with the appearance of several new bands. Above 8.0 kbar the spectrum, whilst characteristically different from those at low pressures, remains unchanged on increasing pressure to approximately 41 kbar, apart from steady hardening of the vibrational modes. The region between 5.9 kbar and 8.0 kbar is best understood in terms of a very narrow phase which has been designated phase III, followed by a region dominated by the sluggish transition III-IV which exhibits characteristic intergrowth of phases displayed in first order systems. The variation in band intensities between III and IV can be seen in Figs. 5.3 & 5.4. In practice, phase III is virtually impossible to isolate in its pure form at room temperature, since its region of stability is so small. Thus

**Table 5.1** Raman shifts and their pressure dependencies for the phases of  $\text{CH}_3\text{HgCl}$ .

	External modes		Internal modes	
	$\nu_i \text{ cm}^{-1}$	$d\nu_i/dP$	$\nu_i \text{ cm}^{-1}$	$d\nu_i/dP$
<u>Phase I</u>	37.2	2.35	288.3	2.1
	48.8	2.3	290.5	3.36
	67.5	2.8	554.2	2.73
			1185.3	-0.91
			2923.3	2.27
<u>Phase II</u>	90.0 <sup>a</sup>		291.2	-0.16
	39.0	1.22	295.2	0.11
	51.5	0.01	556.3	1.93
	70.3	0.73	1186.2	-0.96
			2925.5	2.37
Phase III <sup>b</sup>				
Phase IV	24.0	0.38	301.3	0.23
	36.5	0.35	306.7	0.19
	48.8	0.34	547.8	0.63
	71.8	0.97	553.0	0.64
	111.0	1.05	1180.2	0.07
			2931.5	0.78

a: The two points are related to a curve which would represent the evolution of the soft mode involved in the I/II transition.

b: It is difficult to assess the exact peak positions and number of peaks for phase III since pure phase III has never been isolated.

$\nu_i$ : Initial Raman shift at phase boundary.

Figure 5.1

Plot of frequency versus pressure for the  
internal modes of methyl mercury  
chloride,  $\text{CH}_3\text{HgCl}$ .

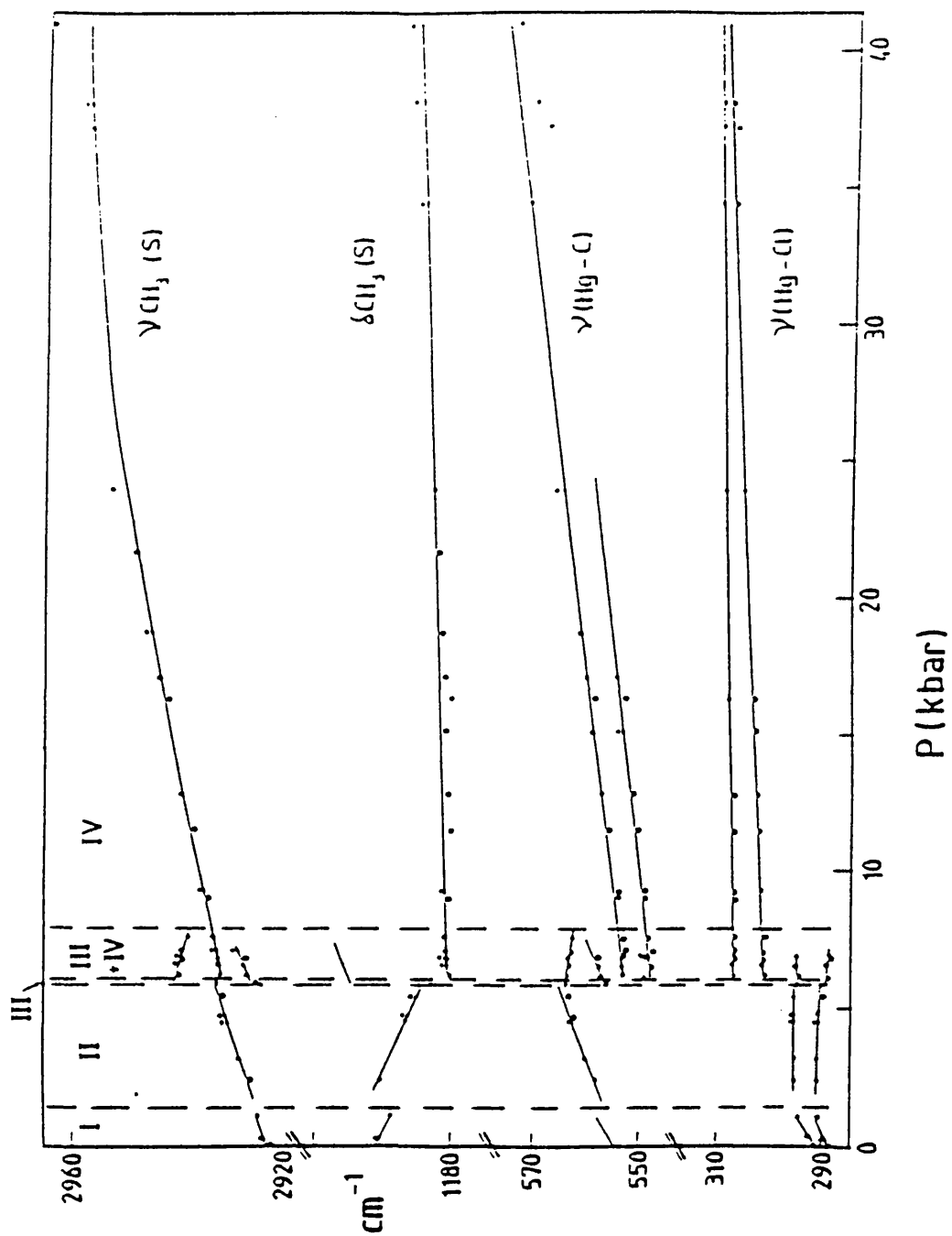


Figure 5.2

Plot of frequency versus pressure for the  
external modes of methyl mercury  
chloride,  $\text{CH}_3\text{HgCl}$ .

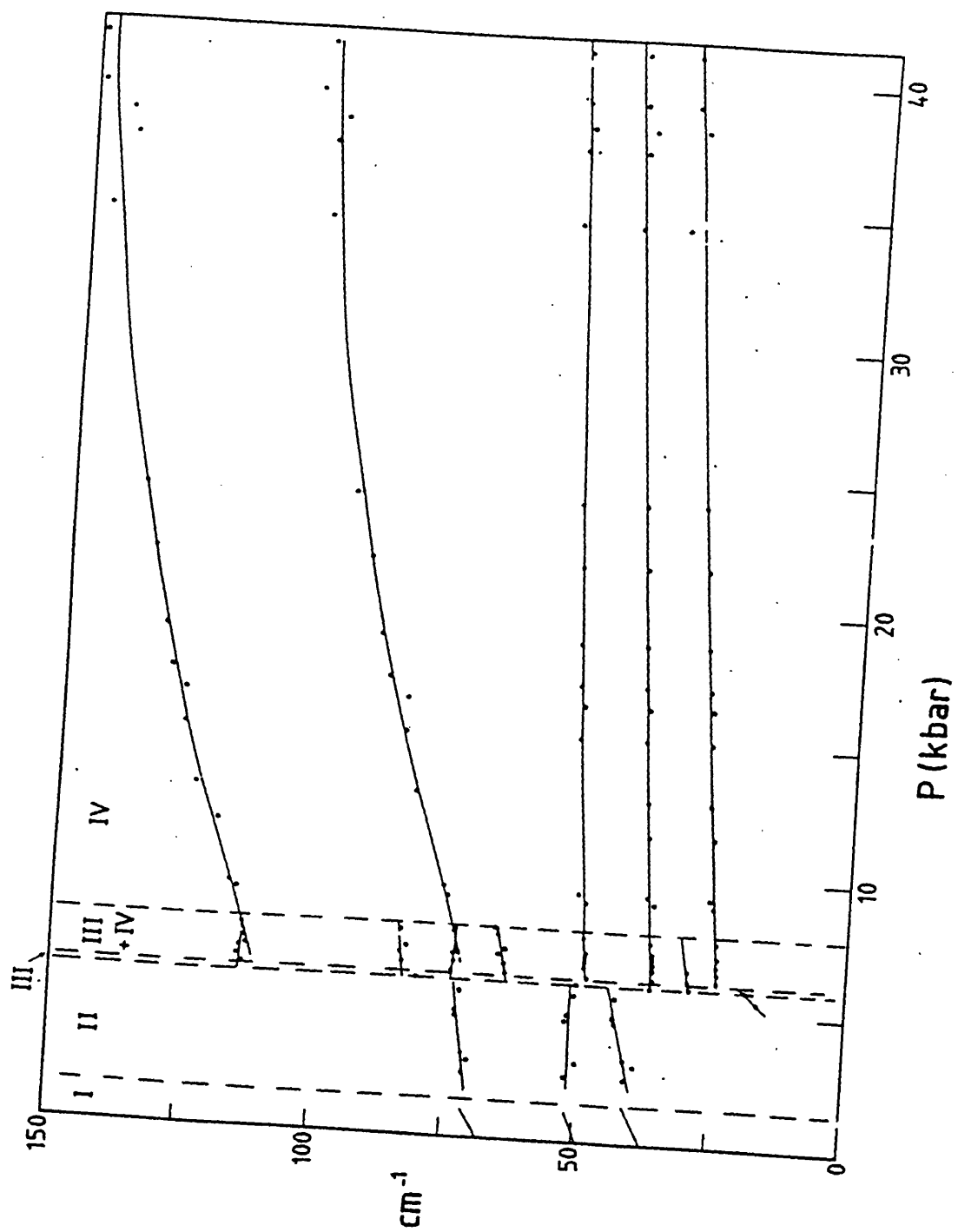


Figure 5.3

The deconvoluted Raman-active external mode spectra of the high pressure phases of methyl mercury chloride,  $\text{CH}_3\text{HgCl}$ . This diagram shows the evolution of  $\text{CH}_3\text{HgCl}$  from phase II at 4.74 kbar, through phase III into pure phase IV at 7.63 kbar. The three middle spectra show a biphasic region with varying amounts of phases III and IV (with the amount of Phase IV increasing with increase pressure).

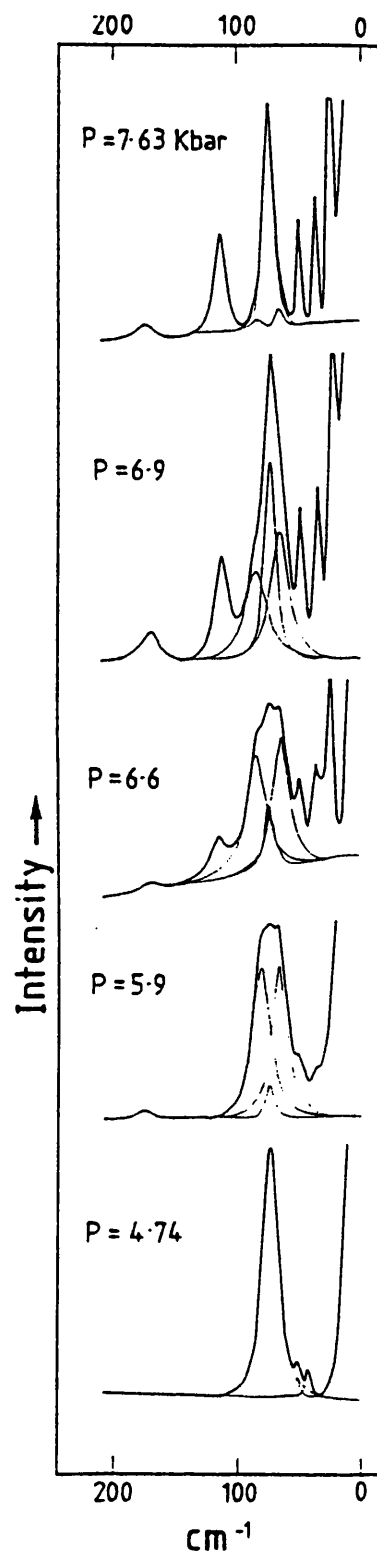




Figure 5.4

The deconvoluted Raman spectra of  $\text{CH}_3\text{HgCl}$   $\nu(\text{Hg-Cl})$  at high pressures. The spectra at 4.74 and 7.63 kbars are of pure phases II and IV respectively. The three spectra 5.9 to 6.9 kbar show a biphasic region with varying amounts of phases III and IV (with the amount of phase IV increasing with increase pressure).

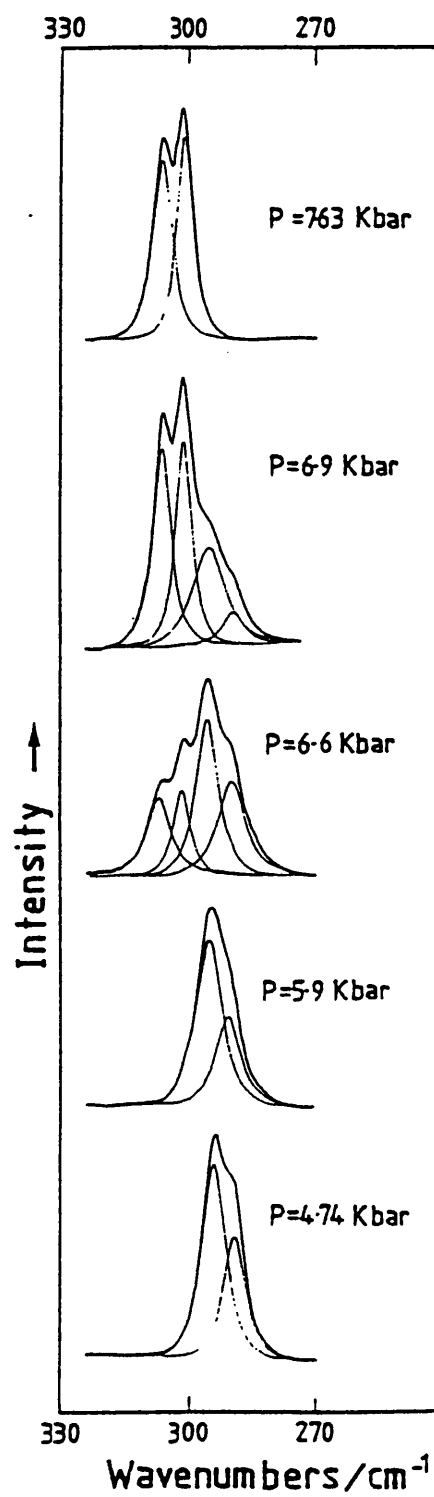


Figure 5.5

The Raman-active internal mode spectrum of the high pressure phases in methyl mercury chloride. The diagram displays representative spectra of all known phases in all regions studied. Spectral slit width is  $1.0\text{ cm}^{-1}$  below  $600\text{ cm}^{-1}$ ,  $1.5\text{ cm}^{-1}$  between  $1000$  and  $1250\text{ cm}^{-1}$  and  $2.0\text{ cm}^{-1}$  above  $2900\text{ cm}^{-1}$ .

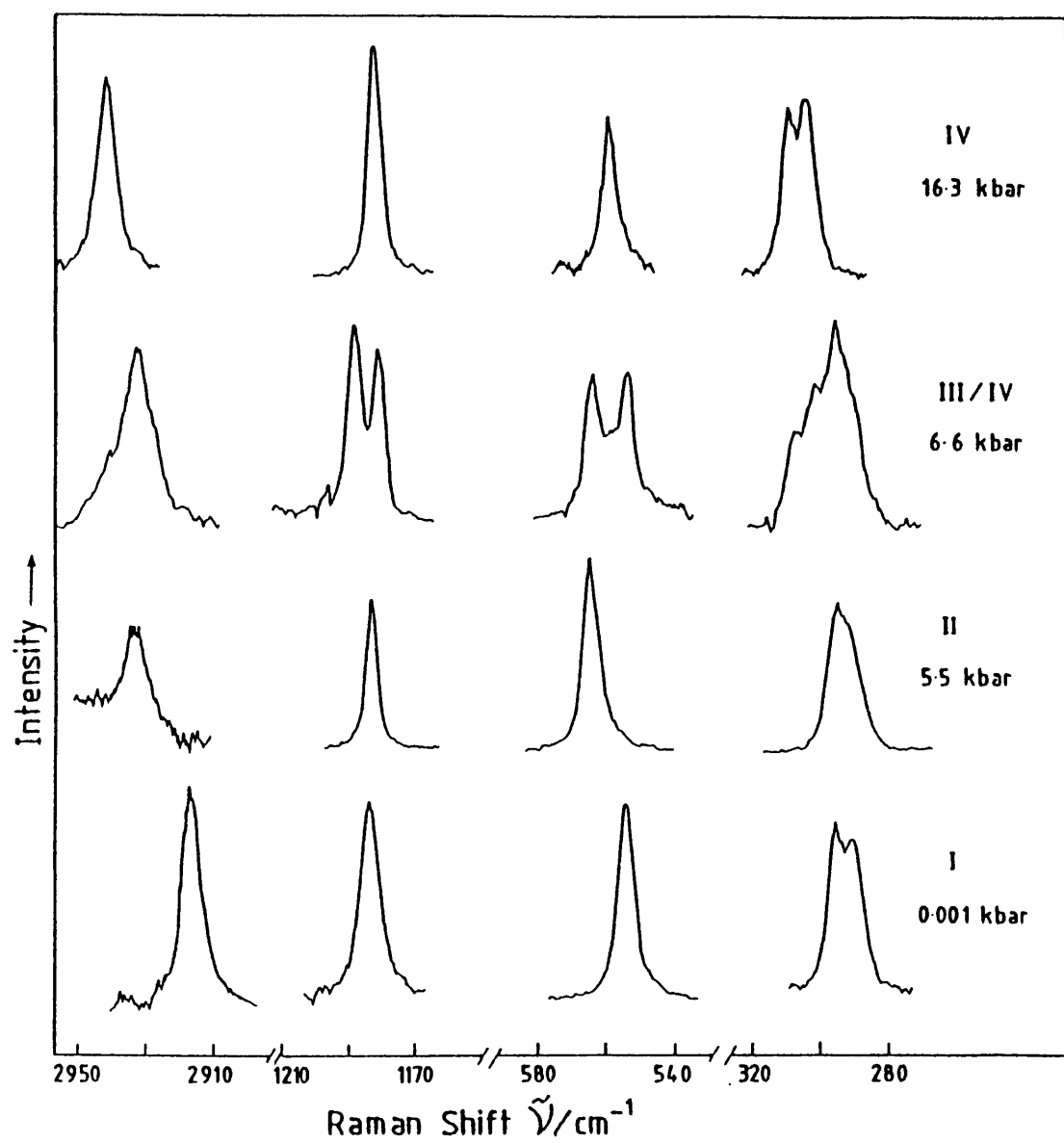
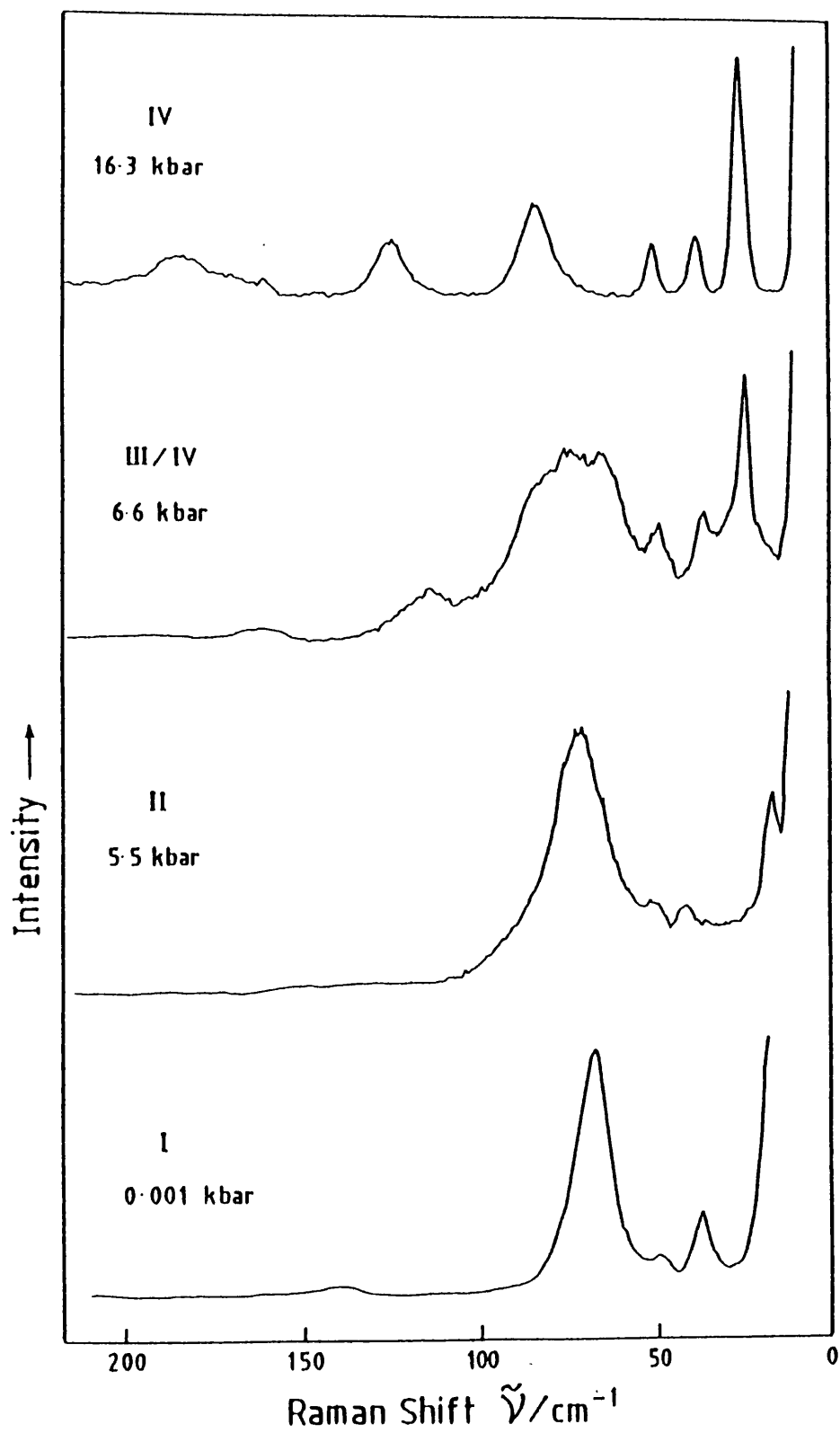


Figure 5.6

The Raman-active external modes of the high pressure phases in methyl mercury chloride. Spectral slit width in all cases was  $1.25\text{ cm}^{-1}$ .



bands characteristic of phase IV are seen as soon as phase III is apparently entered, whilst those due to phase III are gradually lost. This behaviour can be seen clearly in the lattice mode region when observing the bands near 83 and 65  $\text{cm}^{-1}$  for example. When considering the internal modes, a good example is given by the  $\nu(\text{Hg-Cl})$  part of the spectrum, documented in detail in Fig. 5.4, with further evidence given by  $\nu(\text{Hg-C})$  and  $\nu(\text{C-Cl})$  modes, Fig. 5.5. Fig. 5.3 & 5.6, show these series of changes rather well. The spectra at 4.7 and 7.6 kbar are of phases II and IV respectively and are seen to be distinctly different from each other. On reaching 5.9 kbar the intense band at  $\sim 70 \text{ cm}^{-1}$  broadens. On deconvolution, three Lorentzian components were found to be necessary to provide a good fit, with a further feature appearing at 175  $\text{cm}^{-1}$ . At 6.6 kbar another new band appears at 114  $\text{cm}^{-1}$  and is seen to be due to phase IV. Meanwhile, the two strong contributions to the main feature centered at 75  $\text{cm}^{-1}$  decreases in intensity with increase in pressure, almost vanishing by 7.6 kbar, leaving the central component as the dominant feature.

For  $\text{MellgBr}$  at least two Becke lines were observed, although, the mode shifts with pressure, Figs. 5.7 & 5.8 and Table 5.2, indicate the existence of only one phase transition at 12.4 kbar which is followed by a region of intergrowth 1.2 kbar wide incorporating both phases I and IV. Since, it is difficult to establish what pressure the compound is at under ungasketted conditions, then the other observed Becke line may have been at some higher pressures than this study attained. The reason for stopping below 35.0 kbar is due to the compound darkening under pressure and becoming substantially more photo sensitive.

At this phase boundary there is an approximate doubling of Raman active modes. No other changes upto 35 kbar were observed. The spectral variations between phases I and IV can be seen in Figs. 5.9, showing deconvoluted spectra of the lattice modes and Fig. 5.10, showing the internal modes. The plot of mode shifts with pressure of the  $\text{CH}_3\text{HgBr}$  lattice mode region has revealed one unusual feature. On inspection, the pressure-dependence of this lowest frequency mode (7  $\text{cm}^{-1}$  at s.t.p.) suggested that it was a soft mode, with confirmation being obtained in the form of a linear  $\omega^2$  vs. pressure plot, Fig. 5.21 (see section 5.6.2). The extrapolation of this line suggested a phase transition near -0.7 kbar, implying that this transition should be observed at some elevated temperature at ambient pressure. This was found to be the case. The evolution of this soft mode with temperature from 80 to 340 K is

**Table 5.2** Raman shifts and pressure dependencies of the high pressure phases of  $\text{CH}_3\text{HgBr}$ .

	External modes		Internal modes	
	$\nu_i$	$d\nu_i/dP$	$\nu_i$	$d\nu_i/dP$
<u>Phase I</u>	$\rightarrow 0.0^a$		205.4	0.39
	40.09	0.05	528.7	$0.43^b$
	46.0	$0.40^b$	1174.4	-0.32
	51.94	0.89	2923.0	1.73
	70.18	0.99		
<u>Phase IV</u>	19.2	0.54	211.0	$0.63^b$
	30.2	0.23	546.2	0.61
	38.8	0.15	554.8	0.61
	49.8	0.07	1168.4	-0.04
	56.2	0.78	1171.4	-0.01
	72.0	0.60	1187.2	0.40
	76.8	0.64	2941.3	0.78
	79.8	0.75		

a: The curve shows the evolution of the soft mode discussed in section 5.6.3.

b: These data represent a best fit line through points which were considered to be represented by a curve most accurately.

$\nu_i$ : Initial Raman shift at phase boundary.



Figure 5.7

Plot of frequency versus pressure for the  
Raman-active internal modes of methyl  
mercury bromide.

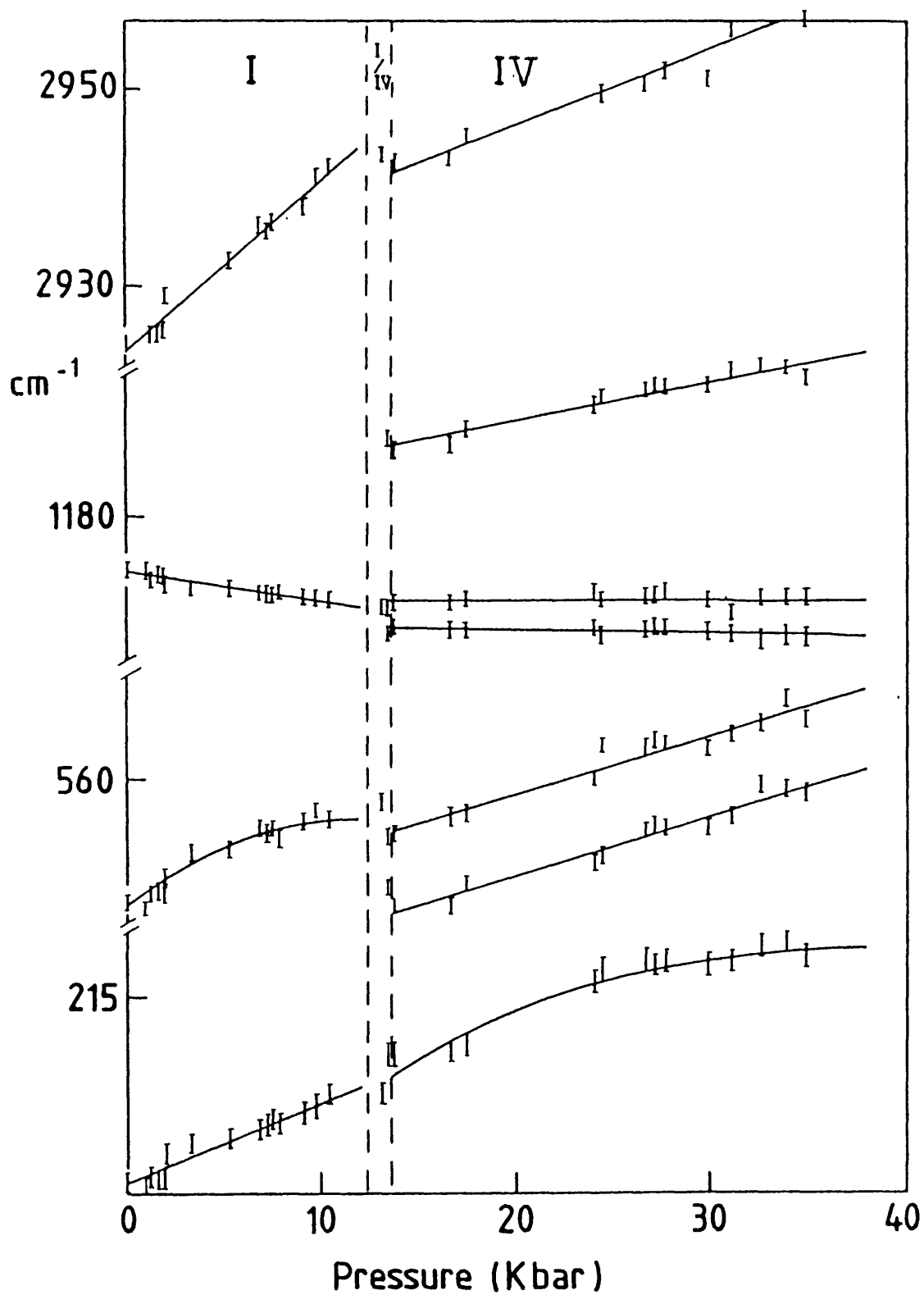


Figure 5.8

Plot of frequency versus pressure for the Raman-active external modes of methyl mercury bromide, showing the emergence of the soft mode (ca.  $7\text{ cm}^{-1}$  s.t.p.) being studied.

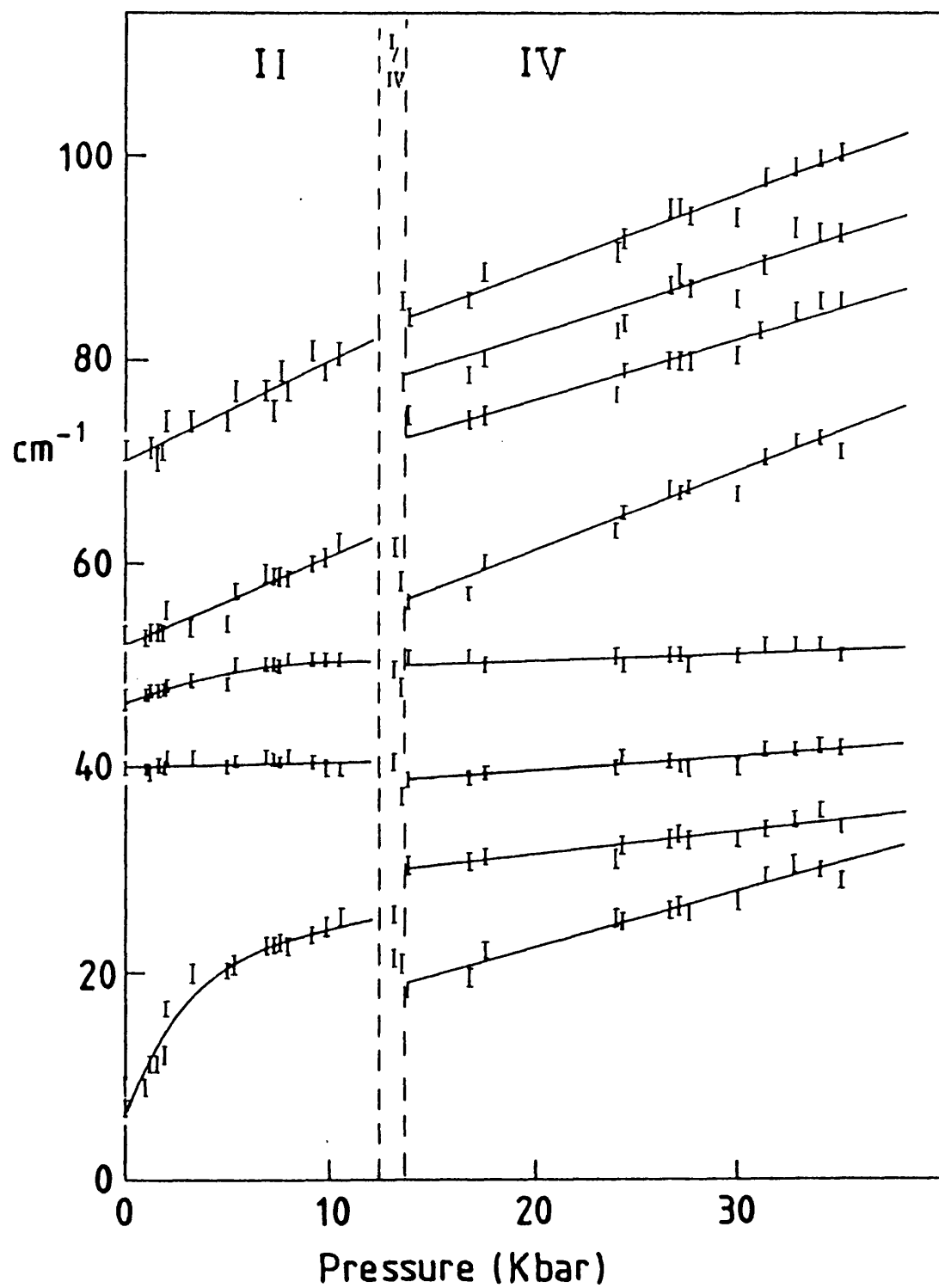


Figure 5.9

Deconvoluted lattice mode spectrum of  $\text{CH}_3\text{HgBr}$  in both phase I and the high pressure phase IV of methyl mercury bromide. Spectral slit width of original spectra were  $1.0 \text{ cm}^{-1}$ .

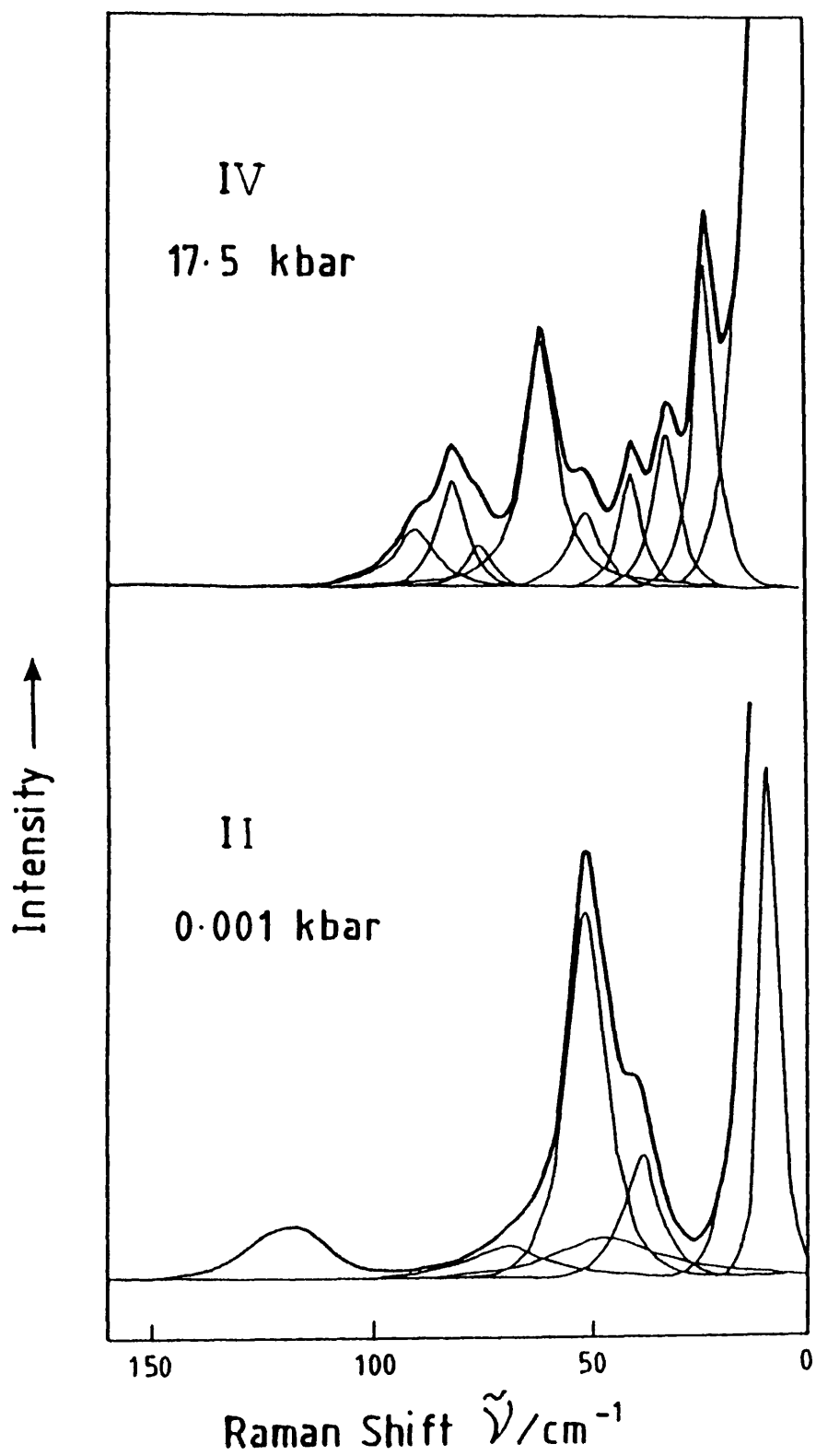
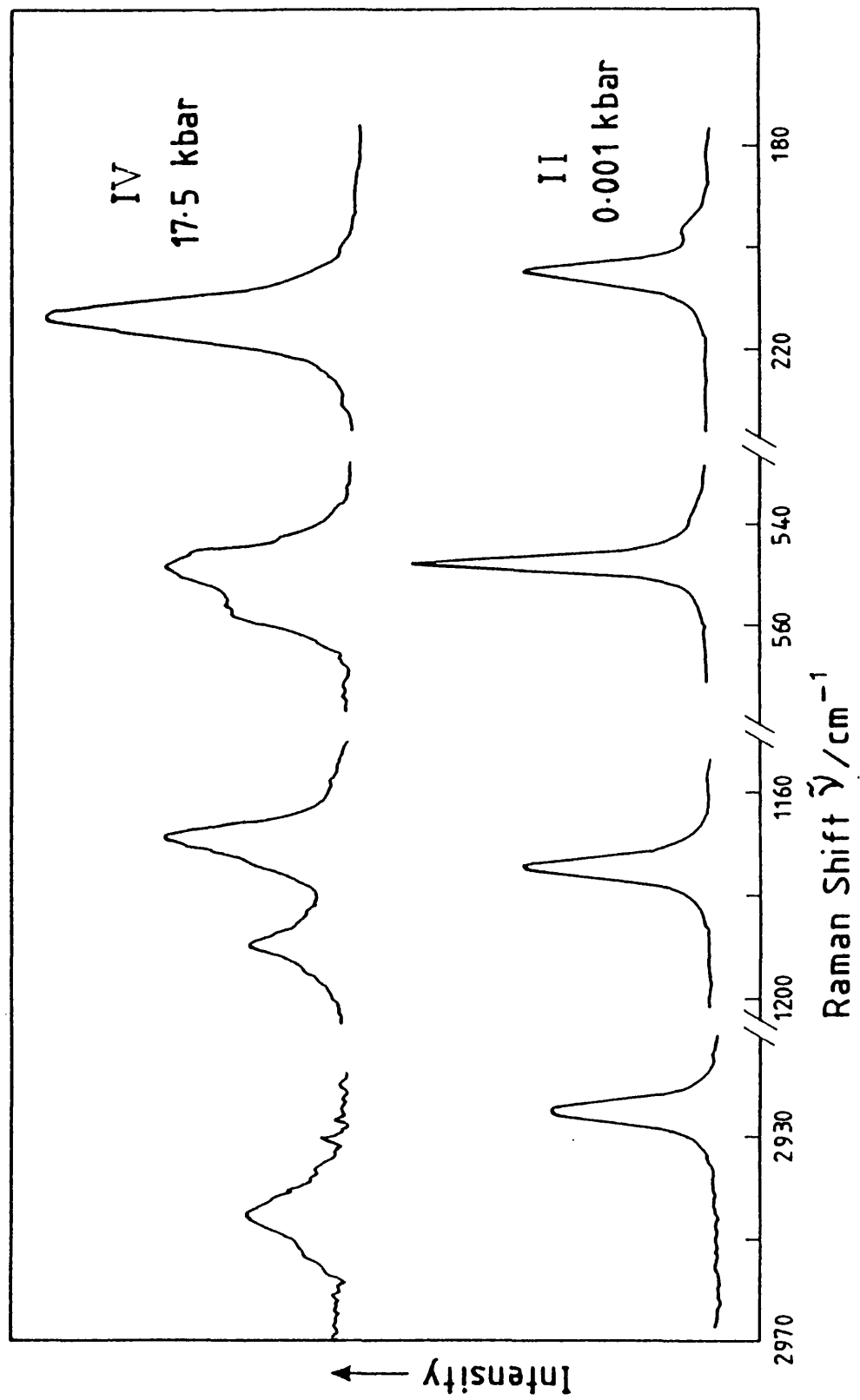


Figure 5.10

Raman-active internal mode spectrum of both the ambient pressure phase I and the high pressure phase IV of methyl mercury bromide. Spectral slit width  $1.0\text{ cm}^{-1}$  below  $1000\text{cm}^{-1}$  and  $1.5\text{ cm}^{-1}$  above  $1000\text{ cm}^{-1}$ .





shown in Fig. 5.19, from which, in conjunction with a  $\omega^2$  vs. temperature plot, a value of  $T_c = 310$  K was obtained.

The high pressure data from  $\text{CH}_3\text{HgCl}$  were then studied in retrospect, and two points at very low frequency (ca.  $17\text{ cm}^{-1}$  at 5.5 kbar) were seen to exist. Their dependence could not be followed to lower pressure because the band was lost in the exciting line. If these two points represent a soft mode analogous to that observed in the bromide, then an analogous variable temperature experiment, from perhaps 80 K to room temperature, should reveal its existence. Fig. 5.22, shows that this is the case and that  $T_c = 162.5$  K. A schematic phase diagram for  $\text{CH}_3\text{HgX}$  is shown in Fig. 5.18. However, there is still a need for much high pressure, variable temperature data in order to establish the exact details of the phase diagrams of these compounds.

In the case of  $\text{MeHgI}$  there appear to be two phase transitions upto 20.0 kbar one at 5.0 and one at 11.5 kbar, which is backed up by Becke lines observed in optical investigations. Mode shifts for all three phases are given in, Figs. 5.11, 5.12 & Table 5.3, with representations of the spectral changes being given in, Figs. 5.13 & 5.14.

Changes are observed at 5.0 kbar and 11.5 kbar. At the first boundary the transition is revealed by a number of breaks in the lines resulting in both shifts upwards and downwards, also, changes in the slope of some mode shifts occur. However, there are no changes in the number of Raman-active components at this phase boundary. At the 11.5 kbar, II-III transition, there are again breaks in lines and changes of slope but there is also the appearance of a new band in the low lattice mode region at approximately 19.0 kbar which then softens under pressure, but not to zero frequency. Also there is a pronounced change in the slope of  $\nu(\text{Hg-I})$  which is a sharp feature easily measured accurately. Continual softening is also observed in the symmetric deformation of the methyl group throughout the regions studied. Spectra of  $\text{CH}_3\text{HgI}$  also show a mode which softens similarly to those in the chloride and the bromide, Fig. 5.25. A plot of  $\omega^2$  vs. pressure suggests  $P_c = -1.7$  kbar, Fig. 5.26. If we assume a phase diagram similar to those of the chloride and the bromide, the probable transition temperature at ambient pressure is ca.  $\sim 340$  K. Further work on this material will be worthwhile only when the crystallography has been fully resolved.

**Table 5.3** Raman shifts and pressure dependencies of the high pressure phases of  $\text{CH}_3\text{HgI}$ .

	External modes		Internal modes	
	$\nu_i$	$d\nu_i/dP$	$\nu_i$	$d\nu_i/dp$
<u>Phase I</u>	12.8	1.41	165.7	0.35
	31.9	0.17	530.4 <sup>a</sup>	0.68
	33.8	0.16	1161.4	-0.62
	37.2	0.69	2917.4	1.08
	42.8	1.42		
<u>Phase II</u>	19.7	0.51	166.9	0.01
	32.7	0.09	532.8	0.91
	40.1	0.35	1154.2	-0.56
	49.2	0.67	2922.4	1.03
	58.5	0.13		
<u>Phase III</u>	19.1	-0.36	167.6	0.89
	23.8	16.62	536.5	0.81
	32.2	0.53	1156.0	-0.4 <sup>b</sup>
	41.1	0.86	2928.5 <sup>c</sup>	
	50.3	28.58		
	54.9	27.87		

a: These data represent a best fit line through a set of points which were considered to be represented by a curve most accurately.

b: Only two available data points in this phase, therefore these values are inaccurate estimates.

c: Only one point available in this phase.

$\nu_i$ : Initial Raman shift at phase boundary.

Figure 5.11

Plot of frequency versus pressure for the internal modes of methyl mercury iodide,  $\text{CH}_3\text{HgI}$ .

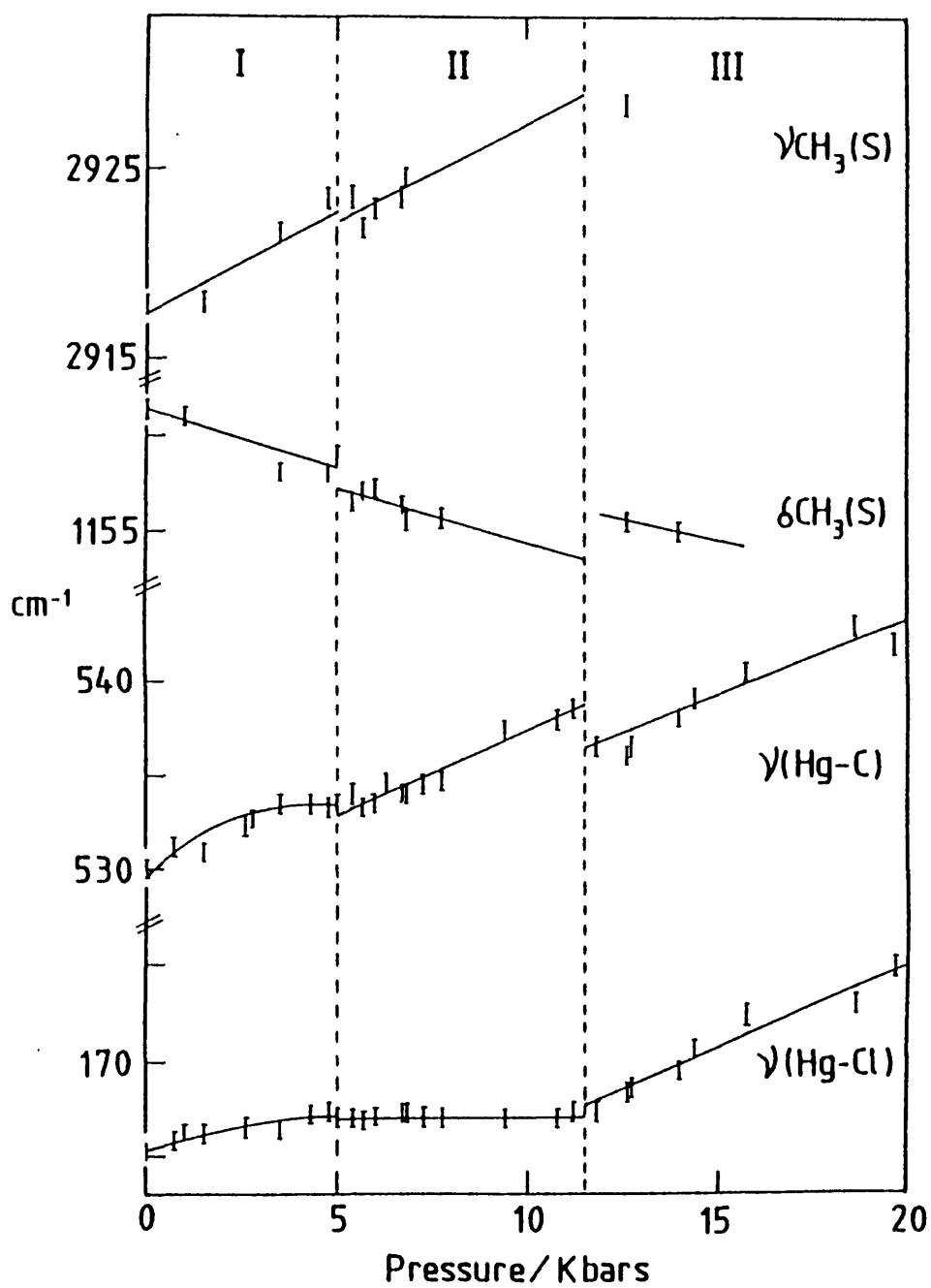
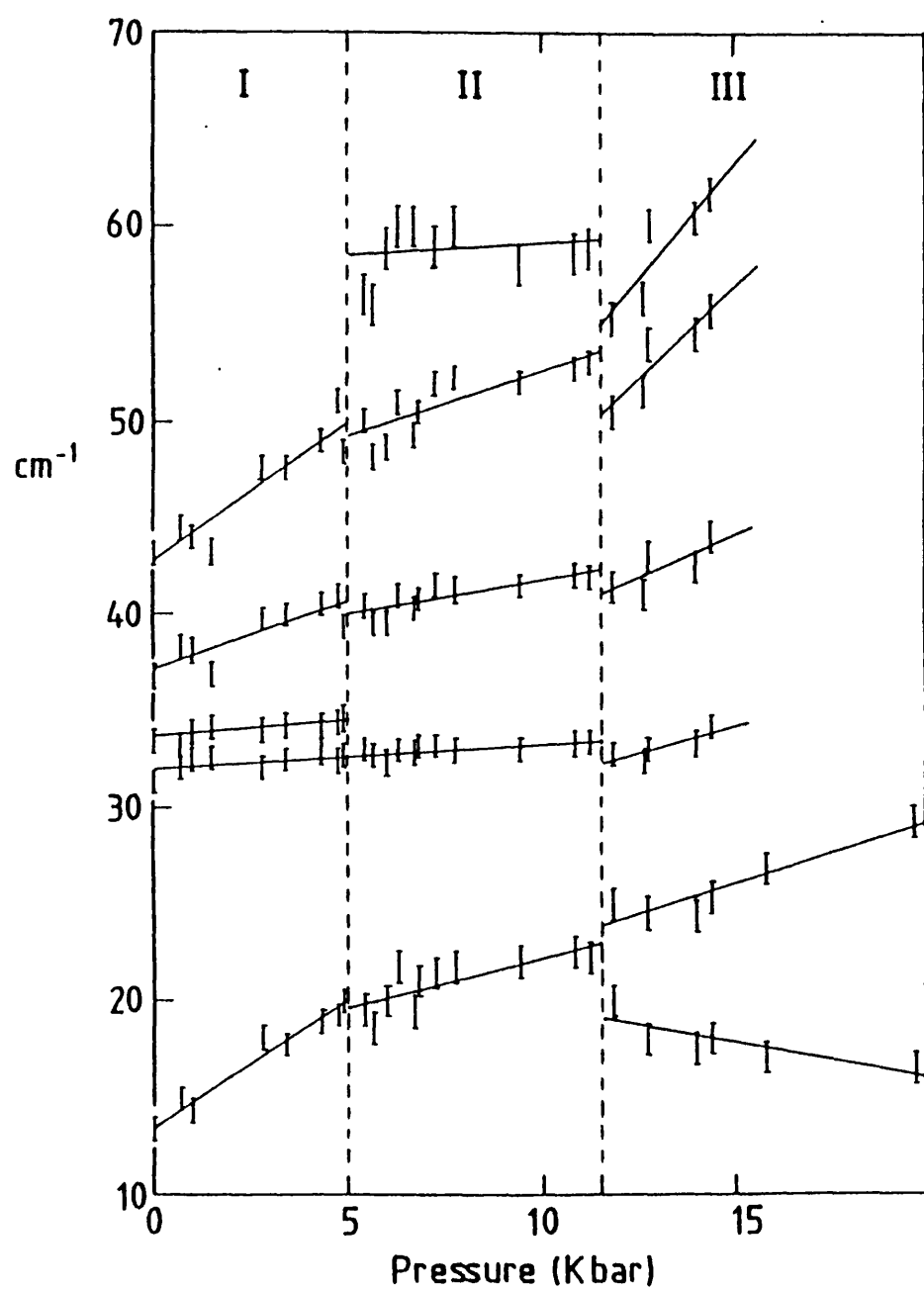


Figure 5.12

Plot of frequency versus pressure for the Raman-active external modes of methyl mercury iodide,  $\text{CH}_3\text{HgI}$ .



**Figure 5.13**

Raman-active external mode spectrum of both ambient and high pressure phases of methyl mercury iodide. Spectral slit width  $1.0\text{ cm}^{-1}$ .

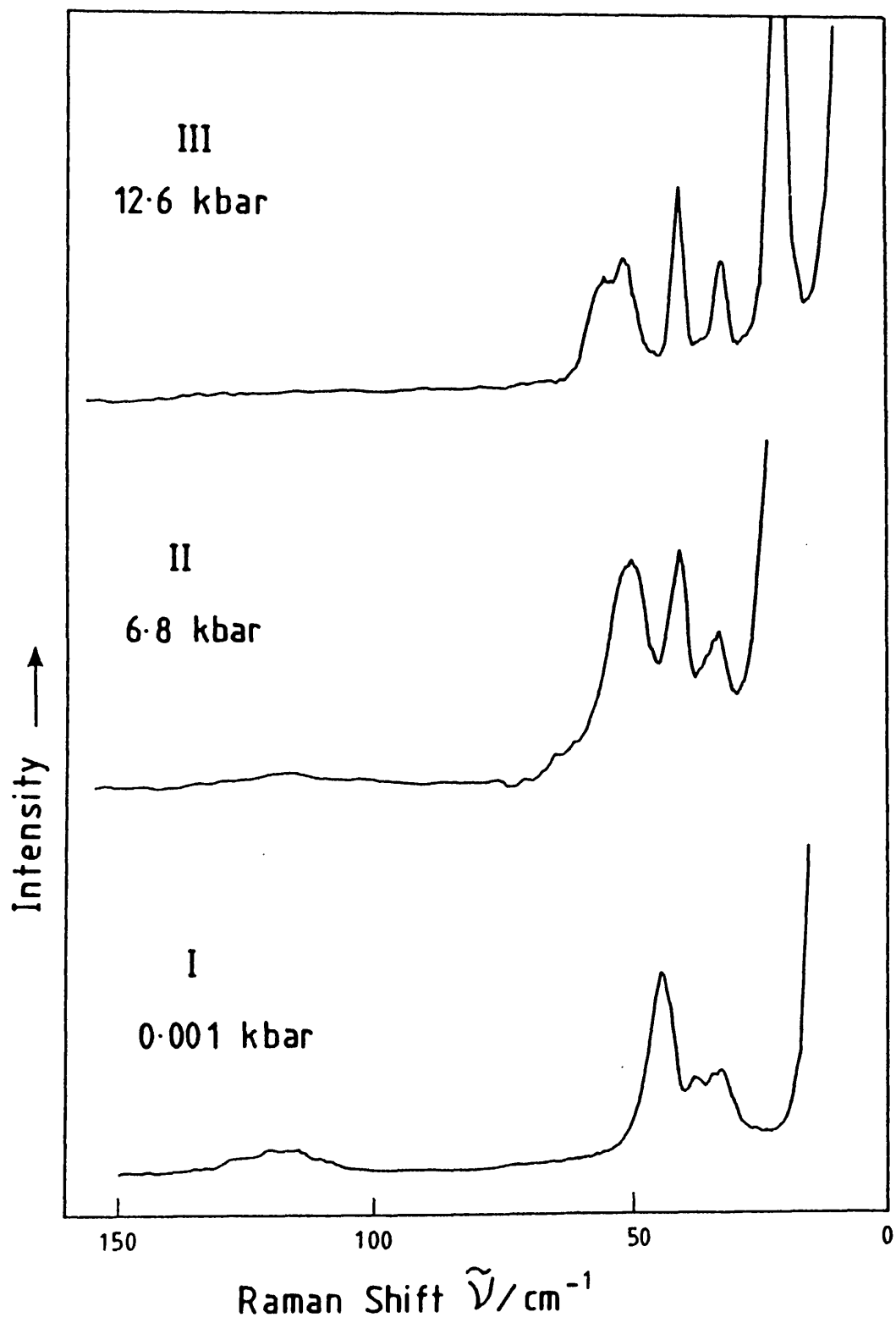
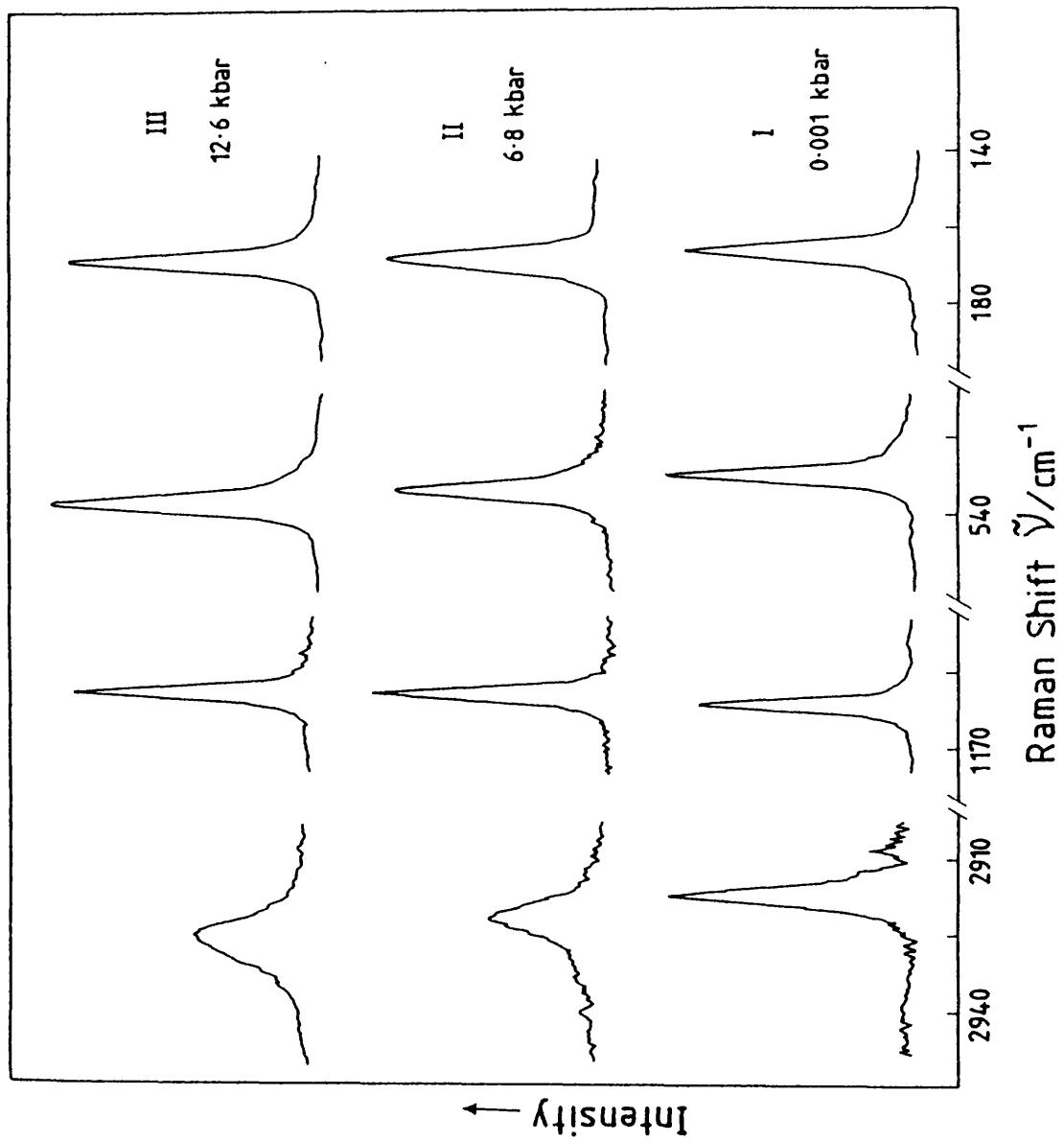




**Figure 5.14**

Raman-active external modes of both ambient and high pressure phases of methyl mercury iodide. Spectral slit width  $1.0\text{ cm}^{-1}$  below  $1000\text{ cm}^{-1}$ , and  $1.5\text{ cm}^{-1}$  above  $1000\text{ cm}^{-1}$ .



## 5.4. Crystallographic data

### 5.4.1. Methyl Mercury Chloride $\text{CH}_3\text{HgCl}$

The structure of methyl mercury chloride was first attempted by Grdenic and Kitiagorodski 1949.<sup>7</sup> It was part of a study on the packing of molecular crystals of the type  $\text{RHgX}$  where in this case  $\text{R} = \text{alkyl}$  and  $\text{X} = \text{Cl}$  and  $\text{Br}$ . Up to the propyl analogue ( $\text{C}_3\text{H}_7$ ) of both the chloride and the bromide a space group of  $\text{D}_{4h}^7$  ( $\text{P4/nmm}$ ) where  $\text{Z} = 2$  was suggested, with lattice parameters varying along the elongated  $c$ -axis as expected. Unfortunately, the only one excluded from this study was  $\text{CH}_3\text{HgBr}$ .

Diagrammatic representation of the  $\text{CH}_3\text{HgCl}$  structure has been given in, Figs. 5.15 & 5.16. Since all atoms are on sites  $2c$  which are of  $\text{C}_{4v}$  symmetry, it is not compatible with a structure exhibiting fixed methyl groups, which would result in  $\text{C}_{3v}$  symmetry. Then in this structure the methyl groups are thought to freely rotate around the  $\text{Hg-C}$  bond. However, it is known that the  $\text{CH}_3\text{---CH}_3$  distances are  $4.22 \text{ \AA}$ , since half of this distance is  $0.1 \text{ \AA}$  less than the value generally taken ( $2.2 \text{ \AA}$ ), for the effective radius of a freely rotating methyl group, the hydrogen atoms of one group must mesh in with those of another, like two gear-wheels.

### 5.4.2. Methyl Mercury Bromide $\text{CH}_3\text{HgBr}$

Since the methyl mercury bromide structure had not been previously deduced, we attempted a determination ourselves.

A tetragonal space group of  $\text{D}_{2d}^3$  ( $\text{P4}_2\text{m}$ ) where  $\text{Z} = 4$ , was revealed. All atoms were determined to be on sites  $4e$ , with unit cell dimensions  $a = b = 6.906 \text{ \AA}$  and  $c = 8.834 \text{ \AA}$ .

Observed interatomic distances:  $\text{C-Hg} = 2.270 \text{ \AA}$

$\text{Hg-X} = 2.490 \text{ \AA}$

and  $\angle \text{C-Hg-X} = 174.7 \pm 1.5^\circ$

A diagrammatic representation of methyl mercury bromides crystal structure has been given in Fig. 5.17. The main difference between the chloride and the bromide structure apart from the enlarged unit cell (ie. now  $\text{Z}=4$ ) is the  $\text{C-Hg-X}$  unit, which is straight in the chloride and bent in the bromide.

**Figure 5.15**

The crystal structure of methyl mercury chloride, showing molecular packing using approximate covalent radii.

Structure of  $\text{CH}_3\text{HgCl}$ ,  $[110]$  Projection

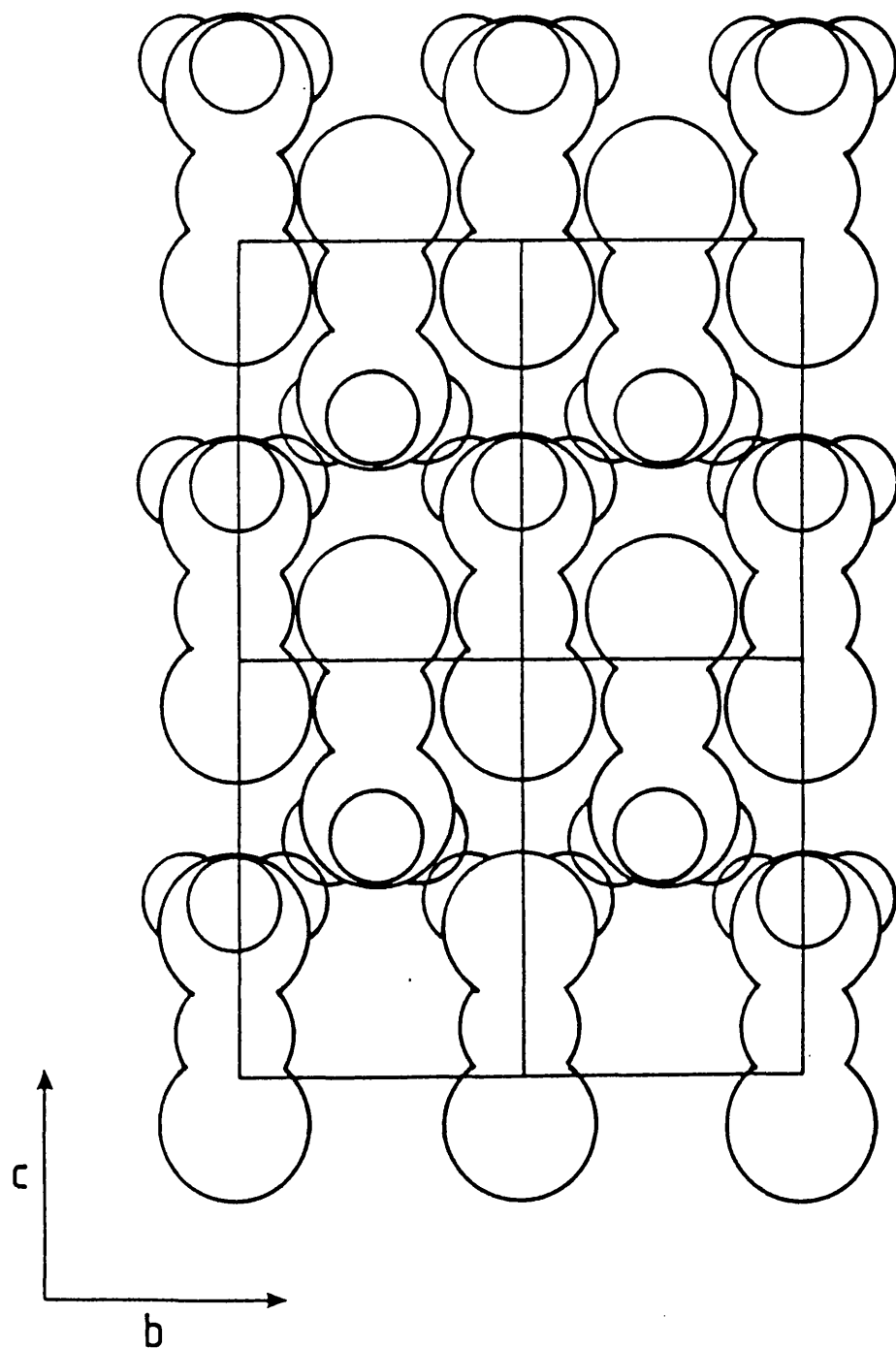


Figure 5.16

Crystal structure of methyl mercury  
chloride.

Tetragonal space group  $D_{4h}^7$  ( $P_4/nmm$ ),

$Z = 2$ .

Lattice parameters:  $a = b = 4.62 \text{ \AA}$

$c = 9.39 \text{ \AA}$

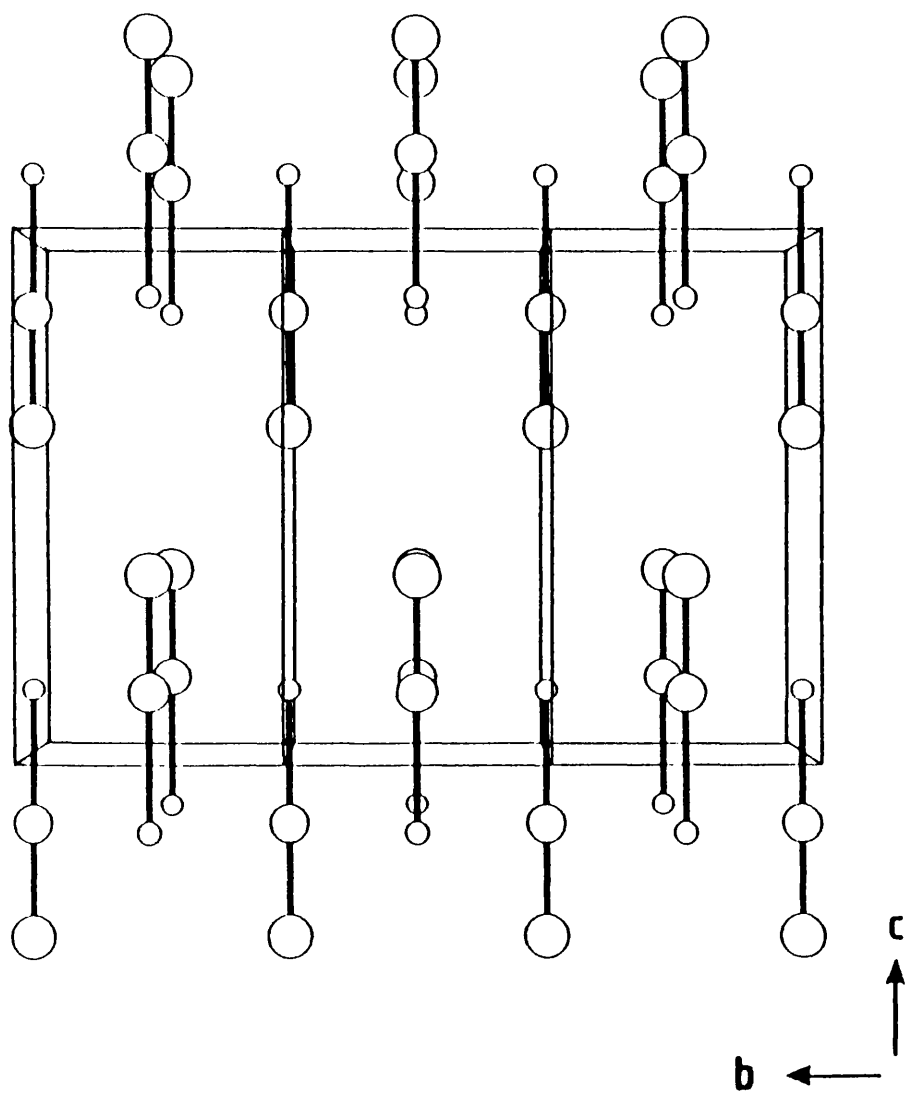


Figure 5.17

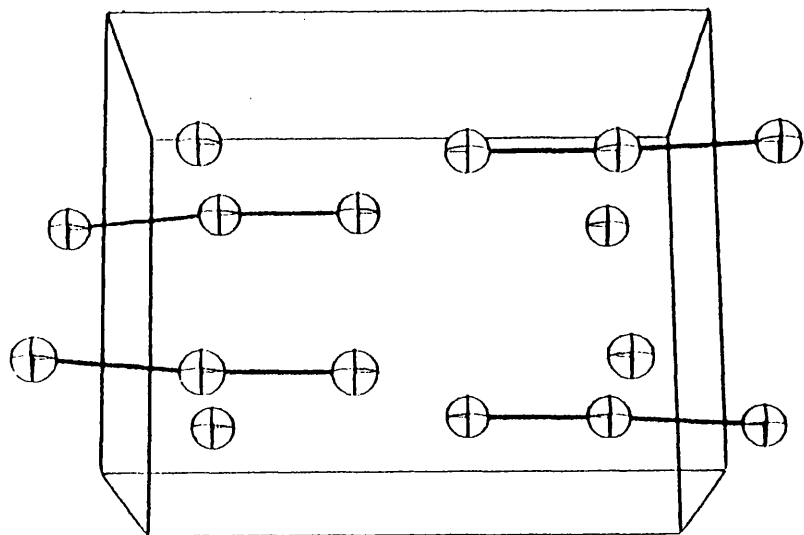
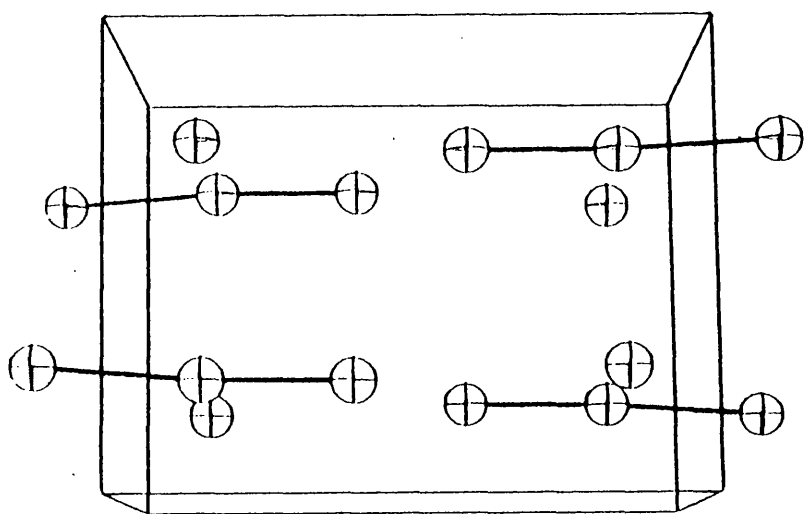
Crystal structure of methyl mercury  
bromide.

Tetragonal space group  $D_{2d}^3$  ( $P\bar{4}2_1m$ ),

$Z = 4$ .

Lattice parameters:  $a = b = 6.906 \text{ \AA}$   
 $c = 8.834 \text{ \AA}$





#### 5.4.3. Methyl Mercury Iodide $\text{CH}_3\text{HgI}$

Attempts were made to deduce the crystal structure of the iodide analogue from single crystal data. Unfortunately, a full set of Weissenberg photographs was not obtained; therefore a full derivation of the space group symmetry was not possible. However, from the limited data available, the structure is considered to be monoclinic. Clearly it is not isostuctural with either the chloride or the bromide in their room temperature phases.

### 5.5. Spectra and Phase Behaviour

#### 5.5.1. Spectra of the Ambient Pressure Phases

From the X-ray results and the proposed phase diagrams we can deduce that the s.t.p. phases of  $\text{CH}_3\text{HgCl}$  and  $\text{CH}_3\text{HgBr}$  are different. On cooling the chloride to below 162.5 K the  $\text{I}(\text{D}_{4h}^7)$  to  $\text{II}(\text{D}_{2d}^3)$  phase transition was induced, whereas the bromide is in phase II at all temperatures from ambient to 80 K. With this understanding, we have reinterpreted the ambient pressure spectra of these two compounds.

Goggin *et al*, satisfactorily assigned the spectra of  $\text{CH}_3\text{HgCl}$  I in both lattice and internal mode regions on the basis of the space group  $\text{D}_{4h}^7$ ,  $Z = 2$ , Table 5.4.<sup>8</sup> The factor group analysis of  $\text{CH}_3\text{HgBr}$  on the basis of  $\text{D}_{4h}^7$  was incorrect, and has now been reinterpreted on the basis of  $\text{D}_{2d}^3$  (below 310 K), Tables 5.5a) & b). The factor group analysis of  $\text{CH}_3\text{HgBr}$  requires eleven Raman-active lattice modes, Table 5.6. However, only seven bands have been observed, but we note that fewer bands than predicted are often observed in  $Z = 4$  cells, due to the potential weakness of the factor group coupling.

In the case of  $\text{CH}_3\text{HgI}$  there are six lattice modes below  $50\text{ cm}^{-1}$ ,<sup>8</sup> one of which is clear only at low temperature. The low-symmetry unit cell proposed by preliminary X-ray work, in principle readily accomodates the observed spectrum, Figs. 5.13 & 5.14.

The internal mode regions (above  $\sim 280\text{ cm}^{-1}$ ) of both the chloride and the bromide can be accounted for on the basis of  $\text{D}_{4h}^7$  selection rules. This again implies that there is little factor group splitting in  $\text{CH}_3\text{HgBr}$  II. However, at low temperature, the  $\nu(\text{Hg-Br})$  region of  $\text{CH}_3\text{HgBr}$  II shows three components as would be expected on the basis of  $\text{D}_{2d}^3$  rules ( $A_1 + B_1 + E$ ). These may be the three factor group components revealed

**Table 5.4** Raman—active external and internal mode frequencies of  $\text{CH}_3\text{HgCl}$  in phase I.

Symmetry Species			frequency ( $\text{cm}^{-1}$ )
$A_{1g}$	$\nu(\text{CH}_3)_s$	$\nu_1$	2923.3wm
$A_{1g}$	$\delta(\text{CH}_3)_{as}$	$\nu_2$	1185.3ms
$A_{1g}$	$\nu(\text{Hg}-\text{C})$	$\nu_3$	554.1vs
$A_{1g}$	$\nu(\text{Hg}-\text{X})$	$\nu_4$	292.7m
			288.4m
$E_g$	$\delta(\text{C}-\text{Hg}-\text{X})$	$\nu_{13}$	142.0vw
$E_g$	$\nu_T$	$\nu_{14}$	67.5vs
$A_{1g}$	$\nu_T$	$\nu_5$	48.8m
$E_g$	$\nu_R$	$\nu_{15}$	37.1ms

(Goggin, Kemeny & Mink 1975)

Table 5.5 Factor group analysis for  $\text{CH}_3\text{HgX}$ .

a)  $D_{4h}^7$

	$A_{1g}$	$E_g$	$A_{2u}$	$E_u$
$N_T$	3	3	3	3
$T_A$			1	1
$T_{OPT}$	1	1		
$R(x,y)$		1		1
$\Gamma_{int.}$	2	1	2	1

Raman

Infrared

b)  $D_{2d}^3$

	$A_1$	$A_2$	$B_1$	$B_2$	$E$
$N_T$	6	3	3	6	9
$T_A$				1	1
$T_{OPT}$	2	1	1	1	2
$R(x,y)$	1	1	1	1	2
$\Gamma_{int.}$	3	1	1	3	4

Ra

-

Ra

Ra & ir

Table 5.6 Correlation scheme for  $\text{CH}_3\text{HgX}$ .

$$\Gamma_{int} = D_{4h}^7 \xleftarrow{\times 2} \text{Site } C_{4v} \xleftarrow{\text{Mol. } C_{\infty v}} \text{Site } C_s(xy) \xrightarrow{\times 4} \Gamma_{int} = D_{2d}^3$$

$A_{1g} + A_{2u}$	$A_1$	$\nu(\text{Hg-C}), A_1$	$A'$	$A_1 + B_2 + E$
$A_{1g} + A_{2u}$	$A_1$	$\nu(\text{Hg-X}), A_1$	$A'$	$A_1 + B_2 + E$
$E_g + E_u$	$E$	def., $E$	$A' + A''$	$A_1 + A_2 + B_1$ $+ B_2 + 2E$

now only after cooling, but this space group also allows lo.-to. splitting in  $B_1$  and E species. In  $CH_3HgI$  both  $\nu(Hg-I)$  and  $\nu(C-H)$  split at low temperature, which is consistent with the purposed low-symmetry environment.

In all three compounds there is an additional feature in their spectra which behaves anomalously, this is the broad bands at  $142(X = Cl)$ ,  $119(X = Br)$  and  $115(X = I)$   $cm^{-1}$  which was attributed by Goggin *et al.* to the  $\delta(C-Hg-X)$  bending mode. In the bromide and the iodide they are dramatically temperature-sensitive rising rapidly in frequency as the temperature is decreased, however, no sharpening occurs. In contrast, the chloride phase II has a singlet initially at  $142\text{ cm}^{-1}$ . In phase I it splits into a doublet which appears consistent with  $D_{2d}^3$  selection rules, but is little affected by temperature. Alternatively, it may be possible to account for the thermal dependence of these modes better by considering them as methyl torsional modes.

#### 5.5.2. Spectra of the high pressure phases

The entry into phase II of  $CH_3HgCl$  at elevated pressures appears to be accompanied by only subtle spectral changes, as the resolution under these conditions is low, not revealing the spectral structure known from low-temperature spectra.

In  $CH_3HgCl$  there is a clear phase change at 5.9 kbar followed by a further transition occurring almost instantaneously, resulting in a significant increase in spectral complexity. A transition displaying similar effects is exhibited by  $CH_3HgBr$  at 12.5 kbar. For the iodide the situation is less clear, there being two phase transitions (5.0 and 11.5 kbar), both displaying only subtle changes in all regions.

However, in all three materials pressure increases cause significant softening of the  $\delta(CH_3)_s$  mode. In the chloride and bromide it becomes relatively insensitive to further pressure increase after the phase transition III/IV. The chloride and bromide  $\delta(CH_3)_s$  now displays two or three components respectively, with splittings of  $7.2(X = Cl)$  and  $18.0(X = Br)$   $cm^{-1}$ .

#### 5.5.3. Phase transition mechanisms

**I/II transition:** This transition in both the chloride and bromide has been designated first order in type since it has a related Becke line under visual examination, and exhibits space groups which are

related by a cell doubling, but not through a supergroup/subgroup correlation and therefore can not be dealt with in the terms of Landau's theory of second order phase transitions.<sup>9,10</sup> The transition probably involves some minor repacking of the C-Hg-X units, resulting in the straightening of these units from an observed angle of  $174.7^\circ$  in phase II to a linear unit in phase I. The resulting increase in packing efficiency may induce the corresponding volume change. The soft mode in phase II when seen well away from the phase boundary, is below  $20\text{ cm}^{-1}$  for both the chloride and the bromide, indicating that it is a lattice mode (further discussion of the soft mode will be made in section 5.6).

II/III and III/IV transitions: These transitions are considered to be first order in type. This is supported by visually observed Becke lines and regions of intergrowth reflecting the sluggish mechanisms often observed in first order systems. The methyl group is implicated in the mechanism of transition II/III since it is preceded by pronounced softening of the  $\delta(\text{CH}_3)_s$  mode within phase II. Removal of the essentially free rotation where the methyl group becomes locked in place at the transition, is suggested for phase III. The increased spectral complexity at this phase transition boundary appears to originate in the breakthrough of i.r.-active modes. In particular the new  $\nu(\text{C-H})$  2926,  $\delta(\text{CH}_3)_s$  1187.5 and  $\nu(\text{Hg-C})$  556.5  $\text{cm}^{-1}$  are all in reasonable positions, when allowing for parallel hardening or softening of the corresponding infrared components from which they originate. In the lattice mode region, the new band at 83  $\text{cm}^{-1}$  may have originated from the 74  $\text{cm}^{-1}$  infrared-mode, also, the new band at 114  $\text{cm}^{-1}$  might have come from  $\nu_{19}$ ,  $E_u$   $\delta(\text{C-Hg-Cl})$  at 107  $\text{cm}^{-1}$  (ambient).

These data suggest loss of the centre of symmetry at the II/III transition. The degeneracy of the  $E_g$  lattice mode is removed, implying the possibility of the  $C_4$ -axis within the cell being removed, further supporting the removal of free rotation in the methyl groups. The above would suggest an orthorhombic space group, with factor group  $D_2$  or  $C_{2v}$ , since this would fit the facts. Of the many possibilities the space group  $D_2^3$  is especially interesting in being thought of as the orthorhombic equivalent of  $D_{2d}^3$  (which is the space group of phase II). The selection rules of  $D_2^3$  require seven Raman-active lattice modes, exactly the number observed in phase III. Further, these bands arise in this model by lifting the degeneracies of the  $E_g$  and  $E_u$  modes accompanied by infrared breakthrough. Alternatively, the transition mechanism may be based upon a cell doubling with a retention of the centre of symmetry.

In the absence of further information on phase IV any discussion on the structure is not worthwhile, neither is it clear whether the equivalence suggested for phases IV in both the chloride and the bromide are true. Much more detailed work is required at variable temperatures along with high pressures to clarify the situation.

When considering  $\text{CH}_3\text{HgI}$  any reasonable transition mechanism must be discussed in the light of conclusive crystallographic data. Also, the mechanisms for the transitions involved in the iodide are evidently different from those in the chloride and bromide.

### 5.6.Soft modes

A concept which makes possible a microscopic understanding of structural phase transitions in solids is that of the soft mode. In simple terms, a soft mode is a vibrational mode, which displays a squared frequency tending to zero linearly as the phase transition temperature or pressure is approached. Structural phase transitions are generally accompanied by atomic or ionic displacements, the mean value of such displacements correspond to an order parameter. Vibrational soft modes are expected to be associated with all such transitions.

If we define a transition as the long-range order of some degree of freedom, such as atomic displacement, rotation or disordering, the order being absent before the transition occurred, then the transition may be described by the order parameter. For this long-range order to exist, the order parameter must be non-zero below the phase transition temperature, and it becomes zero above the transition temperature. In structural phase transitions, an order parameter mirrors the mean magnitude of change in atomic configuration from the parent structure. These atomic displacements generally parallel the variation of a particular normal mode of vibration. This normal mode would then describe the thermal or pressure induced fluctuations in the order parameter. The frequency of this normal mode, in anticipation of the phase transition, decreases. This transition is a result of the eigen vector corresponding to this softening mode being superimposed on the parent structure.

According to Landau's theory of second order phase transitions there is a requirement of the ordering process, which is identified by some ordering parameter, to tend continuously to zero as the transition temperature is approached. Since in structural phase transitions this ordering parameter is mirrored by the corresponding soft mode we may

expect a criterion for second order transitions to be a continuous soft mode reaching zero at  $T_c$ , the transition temperature.

However, in the case of first order transitions, there is an association with latent heat, discontinuous volume changes and large structural changes. Subsequently, the related order parameters associated with first-order transitions are discontinuous. Again, using the link between soft mode and order parameter we may assume that the soft mode will show discontinuous behaviour at the transition.

#### 5.6.2. Evidence for Soft modes in the methyl mercury halides, $\text{CH}_3\text{HgX}$ , where $\text{X}=\text{Cl}, \text{Br} \& \text{I}$

Evidence for the existence of a soft optical phonon in  $\text{CH}_3\text{HgBr}$  was based primarily on the frequency versus pressure plots, Fig. 5.8, where the lowest frequency band ( $7 \text{ cm}^{-1}$  at s.t.p.) was seen to tend towards zero frequency as the transition pressure decreased. Although this soft mode was not seen to decrease to zero energy within the P/T region initially studied. However, on considering our model for the phase diagram of the  $\text{CH}_3\text{HgX}$ 's Fig 5.18, the existence of a high temperature phase transition revealing the behaviour of the soft mode in full at ambient pressure was expected. The appropriate high temperature experiment was carried out, resulting in Fig. 5.19, showing classical behaviour for a softening optically active mode at a first order phase transition. For both temperature and pressure the corresponding frequency squared plots were made, Figs 5.20 & 5.21, these show the expected linear relationship.<sup>11</sup> However, there is some deviation from linearity as the transition is approached, suggesting some damping effects, which are not fully understood in this case, but not totally unexpected.

Further, we looked at  $\text{CH}_3\text{HgCl}$  in the hope of discovering a similar soft mode hence, revealing a transition of similar mechanism to that seen in  $\text{CH}_3\text{HgBr}$ . In the plot of frequency vs. pressure for  $\text{CH}_3\text{HgCl}$ , two points at very low frequency (ca  $17 \text{ cm}^{-1}$  at 5.5 kbar) were detected Fig. 5.2. These were interpreted as the high pressure section of a similar soft mode as that in the bromide. The phase boundary I/II, is considered to be the boundary towards which the soft mode decreases. Hence, a low temperature experiment revealed the transition at ambient pressure giving  $T_c$  as 162.5 K, Fig. 5.22 & 5.23. The plot of frequency squared against temperature for the chloride gives the expected linear



Figure 5.18

Schematic representation of the phase diagram of the methyl mercury halides, showing the known areas of stability, as well as the projected areas of stability suggested by all the data available on these compounds combined.

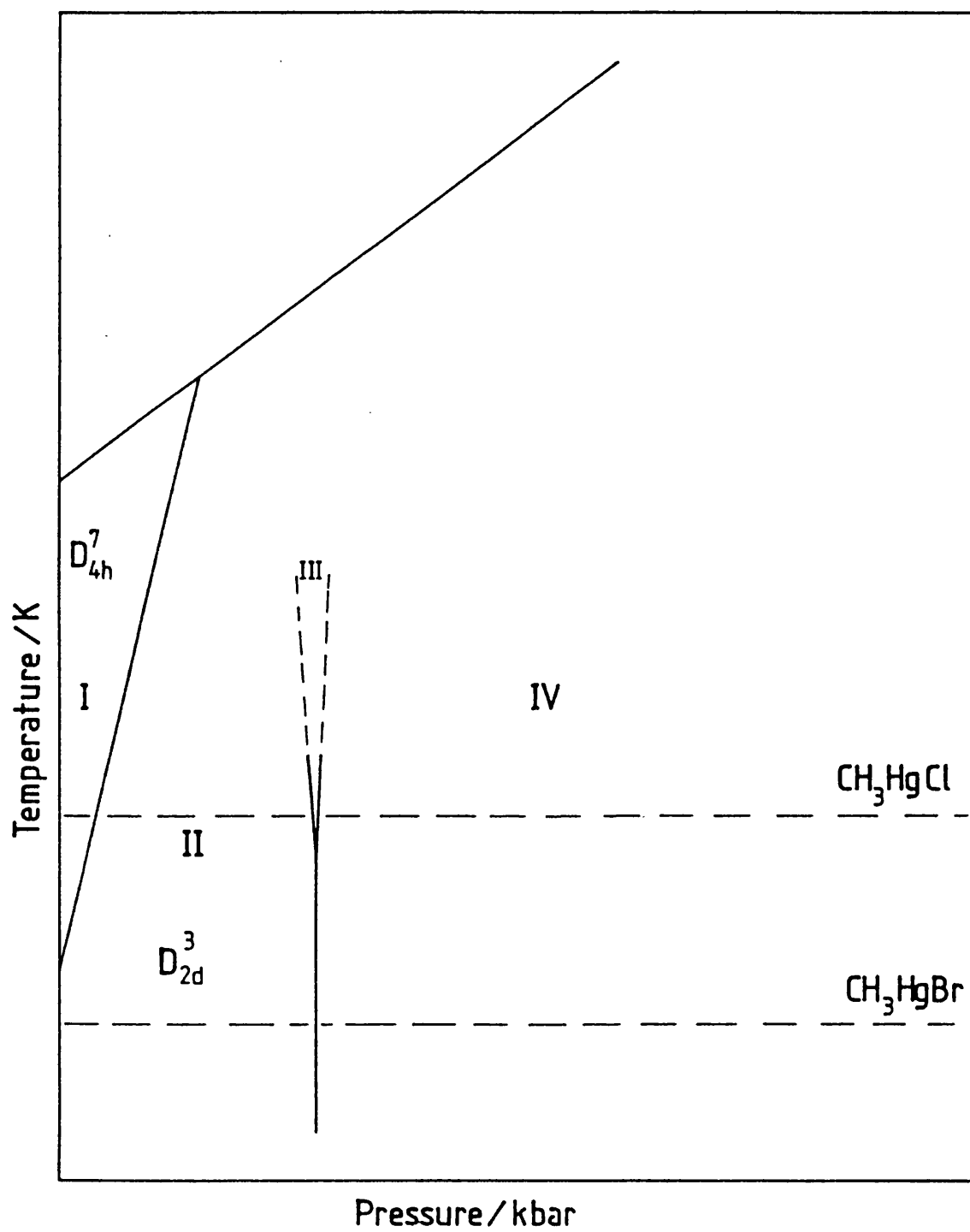


**Figure 5.19**

Plot of frequency versus temperature for the Raman-active soft mode in methyl mercury bromide.

**Figure 5.20**

Plot of frequency squared versus temperature for the Raman-active soft mode in methyl mercury bromide. The plot reveals classical behaviour, modified only near  $T_c$ , by damping effects.

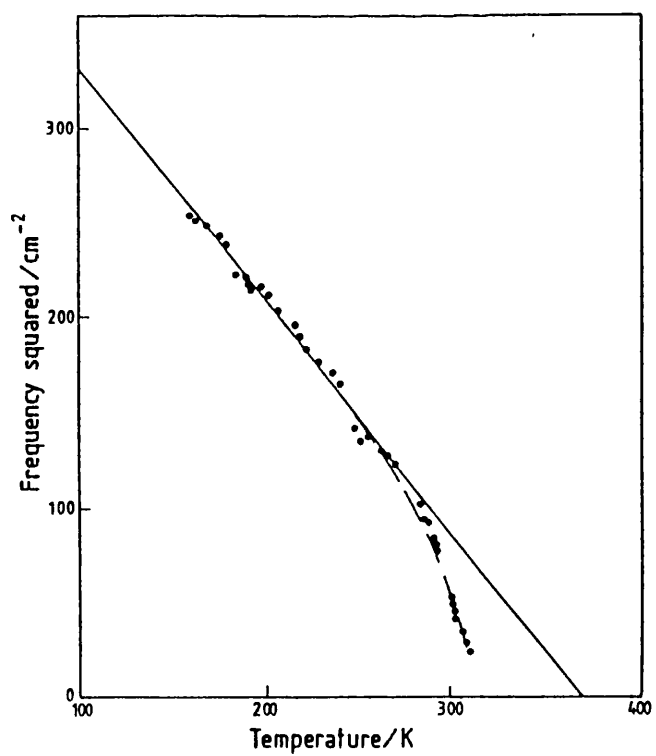
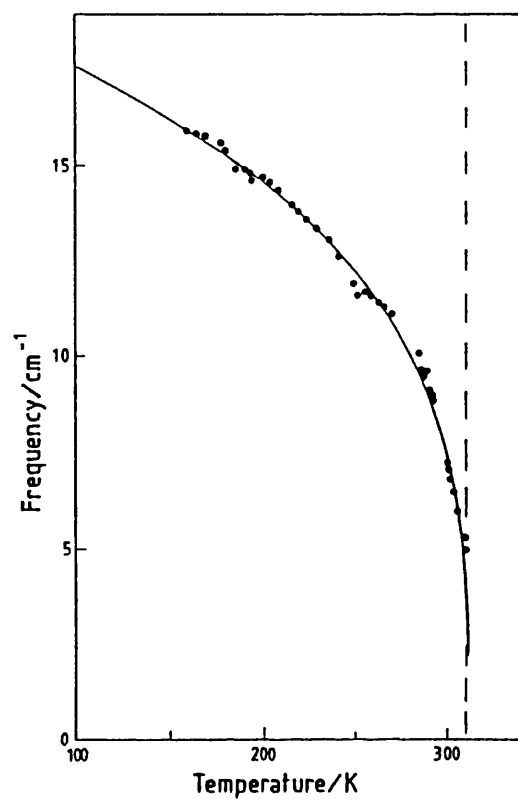


**Figure 5.21**

Plot of frequency squared versus pressure for the Raman-active soft mode in methyl mercury bromide.

**Figure 5.22**

Plot of frequency versus temperature for the Raman-active soft mode in methyl mercury chloride.

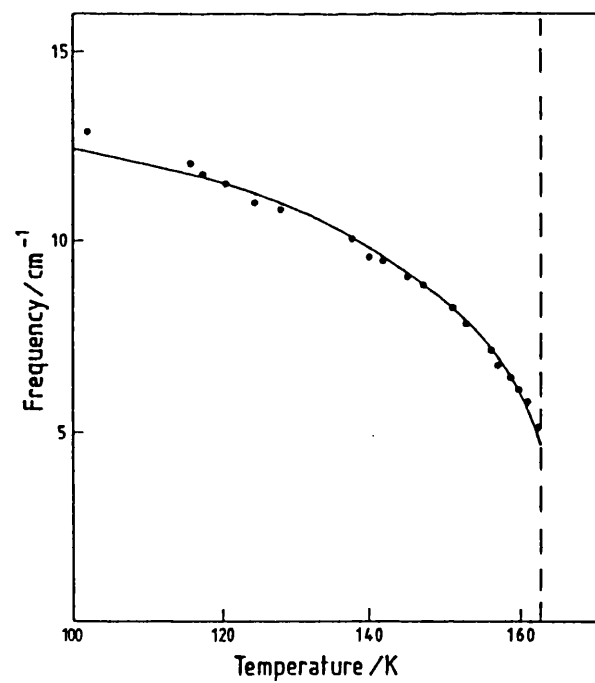
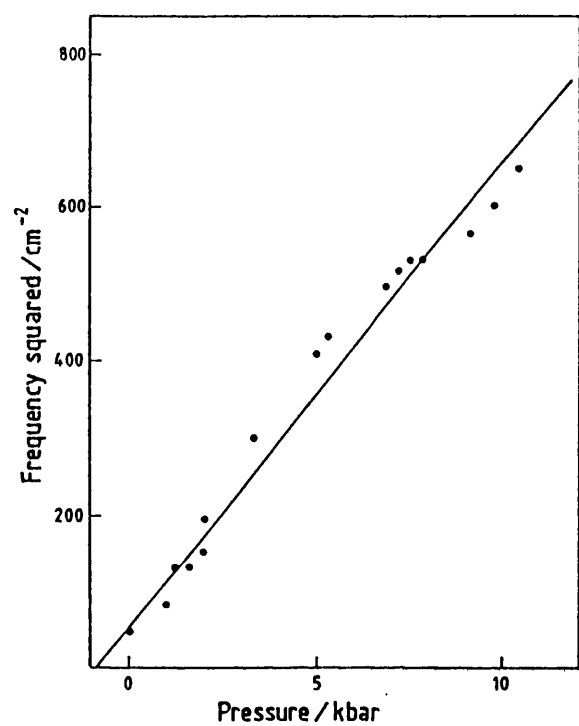


**Figure 5.23**

A 3-D plot showing the evolution of the Raman-active soft mode in methyl mercury chloride giving the relationship of temperature to peak position and peak intensity.

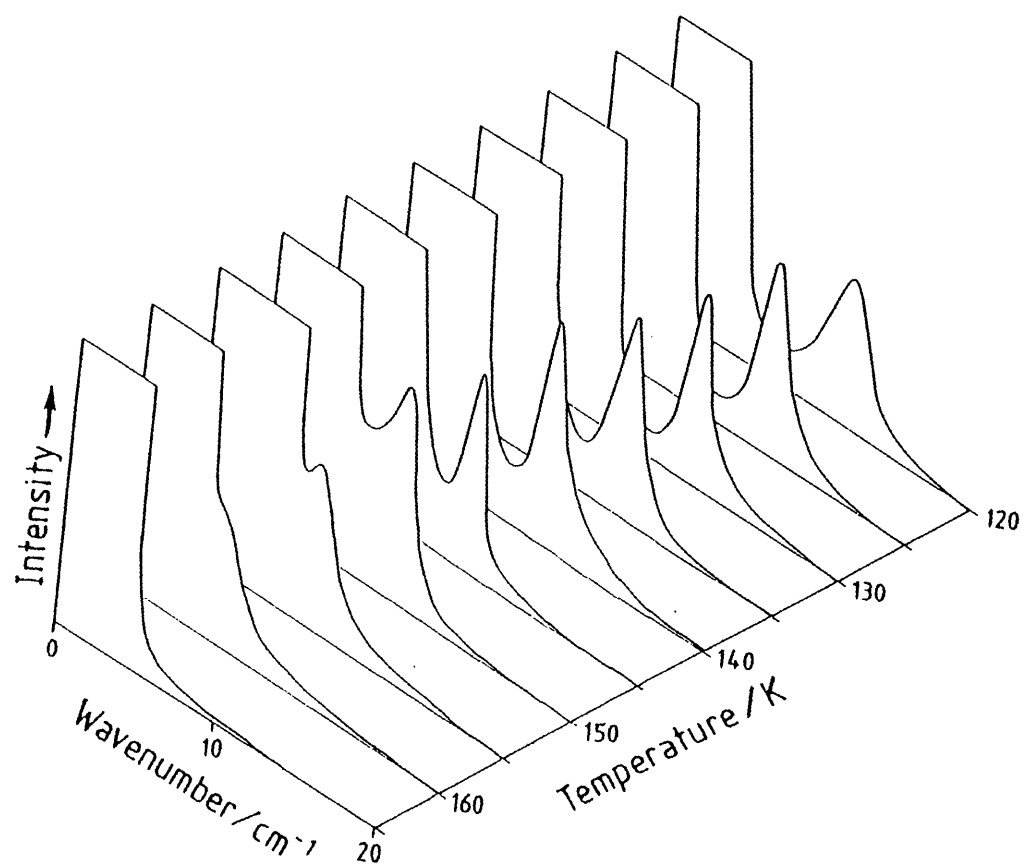




**Figure 5.24**

Plot of frequency squared versus temperature for the Raman-active soft mode in methyl mercury chloride.

**Figure 5.25**

Plot of frequency versus pressure for the Raman-active soft mode in methyl mercury iodide.

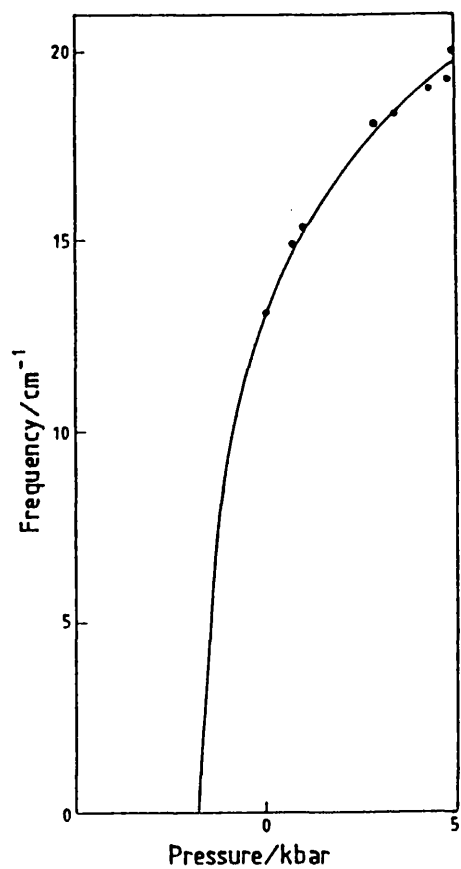
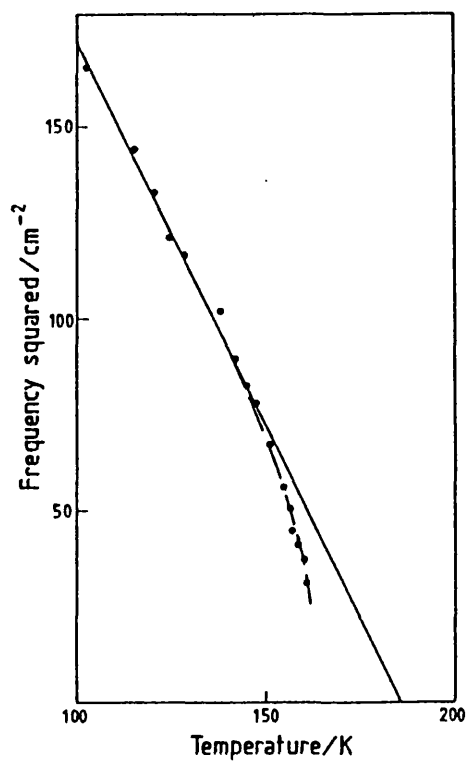
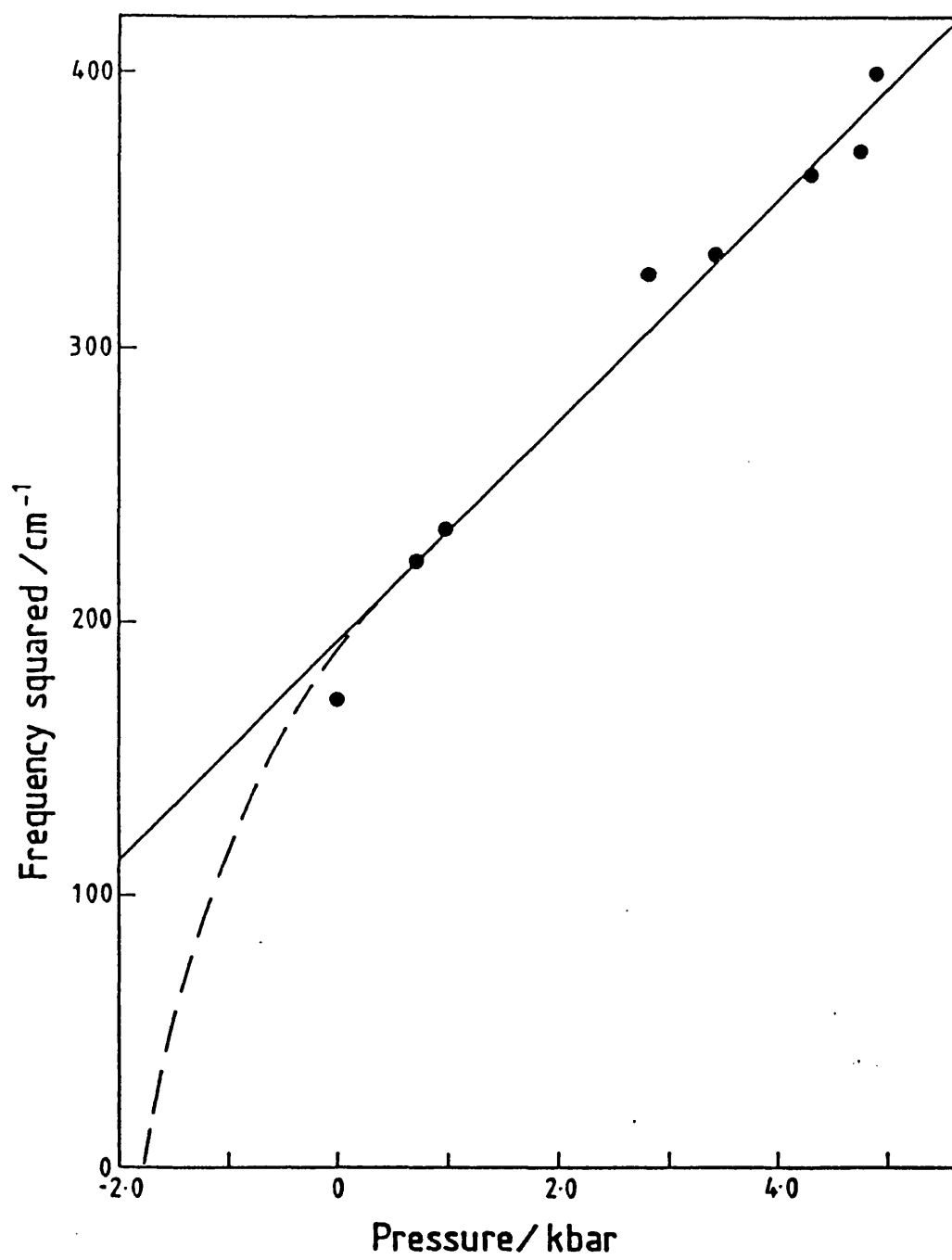


Figure 5.26

Plot of frequency squared versus pressure  
for the Raman-active soft mode in methyl  
mercury iodide.



relationship with the deviation due to damping also in evidence, Fig. 5.24.

When the data on  $\text{CH}_3\text{HgI}$  were considered with respect to soft modes the possibility of one became evident when a frequency verses pressure and a frequency squared verses pressure plot of the lowest frequency band ( $13\text{ cm}^{-1}$  s.t.p.) was made, Figs. 5.25 & 5.26. These plots revealed the expected behaviour, but whether it is analogous to the soft mode observed in the chloride and bromide is unknown.

### 5.6.3. Discussion of soft modes in the methyl mercury halides, X=Cl & Br.

Both analogues of  $\text{CH}_3\text{HgX}$  have a temperature induced phase transition, and in both cases the Raman-active soft mode associated with this transition has been observed. Unfortunately, a full vibrational assignment of the lattice mode region of  $\text{CH}_3\text{HgCl}$  and  $\text{CH}_3\text{HgBr}$  in the ambient pressure phases has not been possible. This has rendered the assignment of a symmetry species to this soft mode virtually impossible. However, we know it must be a lattice mode since it exists in both cases below  $20\text{ cm}^{-1}$ . In the space group  $D_{2d}^3$  translations  $\nu_T$  and librations  $\nu_L$  are allowed to exhibit the same symmetry species, therefore our soft mode may be either a  $\nu_T$ ,  $\nu_L$  or a mixture of both, but it must be non-totally symmetric, since the eigen vector associated with it must have a distorting influence on the lattice. It must also reflect the straightening of the C-Hg-X triatomic unit since this is probably related to the mechanism of the transition.

From the evidence presented, this transition is considered to be first-order. There is no direct route based on a supergroup/subgroup relationship since the transition requires  $D_{2d}^3$  to  $\frac{1}{2} D_{4h}^7$ , also, there is no non-totally symmetric mode in  $D_{2d}$  which has a totally symmetric component in  $D_{4h}$ .

On losing the soft mode near the Rayleigh line, we may assume that the transition has occurred and that the soft mode has been discontinued without ever reaching zero. However, dramatic loss in intensity may be provoked by coupling with other vibrational modes, often acoustic modes at such low frequencies, where an exchange in intensities may be made, this acoustic mode will not be observed by the Raman process.

## References

1. Jenkins, T.E., Ferris, L.T.H. and Bates, A.R. (1977), *J. Phys. Chem.*, **10**, L521.
2. Jenkins, T.E., Ferris, L.T.H., Bates A.R. and Gillard, R.D. (1978), *J. Phys. Chem.*, **11**, L77.
3. Janick, B., Janick, J.M. and Janick, J.A. (1978), *J. Raman Spect.*, **7**, 297.
4. Bates, A.R., Ferris, L.T.H. and Jenkins, T.E. (1979), *J. Phys. Chem.*, **12**, 2945.
5. Adams, D.M. and Payne, S.J. (1976), *Inorg. Chim. Acta.*, **19**, L49-50.
6. Adams, D.M., Hatton, P.D., Shaw, A.C. and Tan, T.K. (1981), *J. Chem. Soc. Chem. Comm.*, 226-227.
7. Grdenic D.R. and Kitaigorodskii, A.I. (1949), *Zhur. Phys. Khim.*, **23**, 1161.
8. Goggin, P.L., Kemeny, G. and Mink, J. (1976), *J. Chem. Soc. Farad. Trans.*, **19**, 1025-1035.
9. Landau, L.D. and Litshitz, E.M. (1959), "Statistical Physics", Pergamon Press, Oxford.
10. Rao, C.N.R. and Rao, K.J. (1968), "Phase Transitions in Solids - An Approach to the Study of the Chemistry and Physics of Solids", McGraw-Hill, New York.
11. Scott, J.F. (1974), *Rev. Mod. Phys.*, **46**, 83.